Copyright is owned by the Author of the thesis. Permission is given for a copy to be downloaded by an individual for the purpose of research and private study only. The thesis may not be reproduced elsewhere without the permission of the Author.

Sensors for Optics-Based Strain, Temperature and Chemical Sensing

A thesis presented in partial fulfilment of the
requirements for the degree of

Doctor of Philosophy
in
Physics

at

at Massey University, Palmerston North,
New Zealand

Adam James Swanson

2015

Abstract

This thesis is a study of optical sensor development with two themes. Firstly, the development of polymer coated glass optical fibre sensors for relative humidity sensing. Secondly, the development and characterisation of novel planar dye-doped polymer waveguide sensors for strain, temperature and chemical sensing. This thesis was motivated by the need to measure strain, temperature and chemicals in harsh conditions with high precision (including compact, high electric field or explosive environments where traditional sensors can not be used). In addition, dye-doped polymer optical chips are being developed for telecommunication applications and their dependence on humidity, temperature and strain will be a key consideration. Sensor applications utilising dye-doping can achieve a greater sensitivity over traditional undoped sensors.

The developed polymer coated glass optical fibre sensors were characterised with humidity calibration experiments. A polyimide based coating was found to have a humidity response of 7.2 pm/%rh corresponding to a coefficient of moisture expansion of 74 ppm/%rh. A series of modified block co-polymer coatings was investigated to identify important chemical structure features. Enhanced performance was achieved by the modification of the chemical structure of an existing commercial polyetherimide. A correlation between coating thickness and optical fibre diameter was observed where the humidity response was enhanced by using thicker coatings or smaller diameter fibres due to a fibre to coating ratio effect. The time response of the sensor's to a humidity step change was measured. To explore the response time dependencies the sensors humidity step change response a novel two-layer model was proposed. A mesh model was also utilised to calculate the diffusion coefficient for each coating. The time response was found to be highly dependent on coating thickness with response time increasing significantly with thickness.

Novel dye-doped polymer sensors were developed by photo-bleaching waveguides containing Bragg gratings, with Bragg reflections observed. The sensor fabrication process was refined by modifying the waveguide dimensions and utilising precise phase mask alignment to obtain a single-mode waveguide with a single Bragg reflection. Methods of coupling the film sensor to a single-mode fibre with a housing unit was explored and a novel method proposed and tested. The film sensors were characterised with strain, temperature and chemical sensing experiments. A strong humidity response in the range of 55 to 65 pm/%rh and the time responses to a humidity step change were measured. Strain responses

in the range of 1.70 to 1.80 pm/$\mu\epsilon$ were observed, exceeding that of comparable silica and PMMA sensors.

Acknowledgements

I would like to express my most heartfelt thanks to my day to day supervisor Sebastiampillai Raymond who was always able to smile and encourage through the difficult times of this thesis and to my university supervisor Mark Waterland whose enthusiasm and guidance has been invaluable.

My sincere thanks to Jeremy Lovell-Smith for his assistance with making humidity measurements, guidance on humidity theory and his extensive proof reading of this thesis and publications. I am deeply indebted to Stefaan Janssens who has offered me invaluable advice, suggestions and ideas throughout my thesis. I would like to express my sincere thanks to the current and former Photonics team members at Callaghan Innovation in particular Robert Breukers, David Clarke, Reece Whitby, Andrew Kay, Gerald Smith, Nicola Winch and Delower Bhuiyan for their chemistry advice and Damian Carder, Dijana Bogunovic, Yasar Kutuvantavida, Ayla Middleton, Victoria Peddie, Andrew Best, Katrina Teu, Ann Manning for their support and especially Julien Hansen and Sebastian Hess for being the best German interns the Photonics team have ever had. I would like to mention a special thanks Philip Zhang for his mathematical help and to Xinjie Song for her invaluable advice and guidance.

I would like to express my sincere thanks to the Callaghan Innovation workshop team who were of great help in the development experimental equipment used in this thesis.

I would especially like to gratefully acknowledge the often overlooked thesis examiners Alan Mickelson, Ian Woodhead and Geoff Jameson who have taken time out of their busy schedules to read through this thesis ensuring its final high quality.

I am deeply grateful for the PhD scholarship from Callaghan Innovation funded by the Ministry of Business, Innovation and Employment New Zealand - for which this thesis would not be possible without.

I am immeasurably grateful to my parents Tony and Pat Swanson and to my sister Vanessa Baunton who have supported and encouraged me throughout this thesis.

Most of all I would like to acknowledge my partner Sophia (Cen Chen) who

was always working with me behind the scenes making sure I had a hot meal at home after a long hard day.

Contents

Abstract i

Acknowledgements iii

1 Introduction 1

2 Basic Concepts 5
2.1 Introduction . . . 5
2.2 Fibre optics . . . 5
2.2.1 Optical fibre . . . 5
2.2.2 Optical modes . . . 5
2.3 Fibre optic sensors . . . 8
2.4 Fibre optic sensors' classification . . . 9
2.4.1 Extrinsic sensors . . . 9
2.4.2 Intrinsic sensors . . . 9
2.5 Fibre Bragg gratings . . . 10
2.5.1 Basic theory . . . 10
2.5.2 Strain and temperature sensing overview . . . 14
2.5.3 Types of fibre Bragg grating sensors . . . 17
2.5.4 Applications . . . 17
2.5.5 Strain tensor measurement . . . 19
2.6 Humidity . . . 19
2.6.1 Humidity sensing applications . . . 20

3 Instruments and Techniques 23
3.1 Introduction . . . 23
3.2 Spin coater . . . 23
3.3 Measurement of pore size . . . 23
3.4 Dip coater . . . 25
3.5 Measurement of thickness and refractive index . . . 25
3.5.1 Metricon 2010 . . . 25
3.5.2 DekTak profilometer . . . 25
3.6 Absorption spectroscopy . . . 26
3.7 Microscope . . . 26
3.8 Interrogator . . . 27
3.9 Optical spectrum analyser . . . 28
3.10 Light sources . . . 28

3.10.1 Broadband light sources . . . 28
3.10.2 Lasers . . . 29
3.10.3 LEDs . . . 30
3.11 Humidity generators . . . 31
3.11.1 Model 2500 Thunder Scientific humidity generator . . . 31
3.11.2 Two-flow humidity generator . . . 31
3.12 Strain measurements . . . 32

4 Humidity response of polymer coated fibre Bragg gratings 33
4.1 Introduction . . . 33
4.2 Basic concepts . . . 34
4.2.1 Bragg gratings as humidity sensors . . . 34
4.2.2 Coefficient of moisture expansion and sensitivity . . . 34
4.2.3 Dip coating theory . . . 38
4.3 Fibre preparation . . . 39
4.3.1 Stripping fibre coatings . . . 40
4.3.2 Surface cleaning . . . 41
4.3.3 Adhesion promoter . . . 41
4.3.4 Dip coating . . . 42
4.3.5 Spray coating . . . 46
4.3.6 Drying . . . 46
4.4 Experimental setup . . . 46
4.4.1 Humidity response setup . . . 47
4.4.2 Temperature response setup . . . 48
4.5 Poly(methyl methacrylate) fibre coatings . . . 49
4.6 Polyetherimide fibre coatings . . . 52
4.6.1 Dip coated polyetherimide coatings . . . 54
4.6.2 Spray coated polyetherimide coatings . . . 54
4.6.3 Modified polyetherimide coatings . . . 56
4.7 Polyimide fibre coatings . . . 58
4.7.1 Avensys polyimide . . . 58
4.7.2 P84 polyimide . . . 60
4.7.3 P84 HT polyimide . . . 62
4.7.4 Adhesion promoter mechanism . . . 64
4.8 Other fibre coatings . . . 65
4.8.1 Ormocer . . . 65
4.8.2 Polyvinyl alcohol-co-ethylene vinyl alcohol . . . 65
4.8.3 Acrylate . . . 67
4.8.4 No coating . . . 67
4.9 Temperature response of coatings . . . 67
4.10 Summary and future work . . . 68

5 Humidity time response of polymer coated fibre Bragg gratings 71
5.1 Introduction . . . 71
5.2 Basic concepts . . . 71
5.2.1 Two-layer model . . . 71
5.2.2 Mesh model . . . 73

5.3 Experimental method 74
5.4 Pore size measurements 75
5.5 Poly(methyl methacrylate) fibre coatings 79
5.6 Polyetherimide fibre coatings 84
5.7 Polyimide fibre coatings 84
5.7.1 Avensys polyimide 85
5.7.2 P84 polyimide 85
5.7.3 P84 HT polyimide 88
5.8 Other fibre coatings 90
5.9 Summary and future work 90

6 Fabrication of planar dye-doped polymer Bragg grating sensor 93
6.1 Introduction 93
6.2 Basic concepts 94
6.2.1 Introduction to dye doping 94
6.2.2 Film sensor design concept 95
6.3 Sensor fabrication 97
6.3.1 Film fabrication 97
6.3.2 Waveguide inscription 99
6.3.3 Bragg grating writing 102
6.3.4 Coupling 108
6.3.5 Bragg reflections 111
6.3.6 Summary and future work 116

7 Planar dye-doped polymer Bragg grating sensor 119
7.1 Introduction 119
7.2 Basic concepts 120
7.2.1 Dye-doped polymer films as humidity and temperature sensors 120
7.2.2 Dye-doped films as chemical sensors 122
7.2.3 Dye-doped polymer films as strain sensors 122
7.3 Humidity and temperature response of doped film sensors 124
7.3.1 Experimental setup 124
7.3.2 Humidity and temperature response 125
7.4 Chemical response of doped polymer film sensor 131
7.4.1 Experimental setup 131
7.4.2 DNT response 133
7.5 Strain response of doped polymer film sensor 137
7.5.1 Experimental setup 137
7.5.2 Strain response 140
7.6 Summary and future work 147

8 Summary 149

Abbreviations

APC	Amorphous polycarbonate
BA	Poly(methyl methacrylate-co-butyl methacrylate)
BAF-1	A photo-switchable chromophore
CME	Coefficient of moisture expansion
DMF	Dimethylformamide
DNT	2,4-dinitrotoluene
EA	Poly(methyl methacrylate-co-ethyl acrylate)
FBG	Fibre Bragg grating
FOS	Fibre optic sensor
FWHM	Full width half maximum
MA	Poly(methyl methacrylate-co-methacrylic acid)
Mod PEI	Modified polyetherimide
NEP	N-ethyl-2-pyrrolidone
OSA	Optical spectrum analyser
PEI	Polyetherimide
PMMA	Poly(methyl methacrylate)
PVOH-ET	Polyvinyl alcohol-co-ethylene vinyl alcohol
PYR-3	A second-order non-linear optical chromophore
TCE	1,1,2-Trichloroethane

Chapter 1

Introduction

Fibre Bragg Gratings (FBGs) are an essential component in the established and emerging fields of optical communications and optical fibre sensing [1]. Traditionally their use as sensors has been focused on strain and temperature sensing where their advantage of high sensitivity, intrinsically safe, non-destructive and remote sensing has allowed them to stand out from other sensors. They are an active area of research and have shown particular promise as niche sensors for use where other sensors cannot be used. Recently polymer coated optical fibre based fibre Bragg gratings have drawn attention as moisture sensors in civil structures, power transformers and fuel cells [2], which subject sensors to compact and harsh conditions. Silica fibre Bragg grating sensors have drawn special attention as a sensor for the particularly harsh environment of a furnace, where temperatures greater than 1,000 °C have been recorded [3]. Initially observed in doped glass fibre, Bragg gratings have now been made in plain polymer, dye-doped fibre and dye-doped films, opening up the possibility of increased sensitivity and new sensing applications. These include smart optical sensing chips that can have multiple Bragg gratings allowing an integrated sensor measuring temperature, strain tensor, humidity, pressure, acceleration and chemicals.

Currently the humidity responses of coated FBGs tends to be small, which means that while cheap to manufacture, costly high-precision interrogator instruments are required for read out - restricting their widespread use. The development of a polymer coating giving a large and fast humidity response would allow the possibility of using a cheaper, lower precision interrogator unit. This complements current research developing lower cost interrogator units. Polymer optical fibres have been shown to give much larger humidity responses than their coated silica fibre counterparts, but often this comes at the cost of an extremely slow temporal response.

Adding a dye can induce a greater refractive index change allowing for smaller Bragg gratings and leading to greater sensitivity than undoped polymer and silica fibre based FBGs. The development of a dye-doped polymer film humidity sensor offers the possibility of a large and fast humidity response using a single-mode waveguide, thereby preserving the Bragg reflection. The use of a dye could

potentially enhance the strain response allowing it to outperform its undoped polymer film analogue - giving an enhanced response to humidity and strain. Using a dye also gives rise to the possibility that the vapour of highly polarised molecules (e.g. explosives) could be detected by the sensor.

Dye-doped polymer planar sensors opens up the possibility of an optical sensing chip. This sensing chip could house a configuration of multiple sensors to measure strain, temperature and chemicals simultaneously. A particular advantage would be obtained if the chip were used as a strain sensor as much smaller rosettes could be written, compared to conventional optical fibre strain rosettes. This sensing chip is made possible by utilising a dye, where the sensing components can be made much smaller in size - reducing the length of Bragg gratings from the current 10 mm to less than 0.5 mm.

This thesis contains two branches of work: the research and development of a humidity sensitive coating on existing glass-based fibre Bragg gratings and the research and development of a novel dye-doped polymer film sensor. The contents of this thesis are arranged as follows:

Chapter 2: This chapter gives a review of fibre optics and the current use of fibre optic sensors. It then focuses on one particular fibre optic sensor, the fibre Bragg grating. Here the basic theoretical background of Bragg gratings and their use as sensors is given with an introduction to concepts of humidity. This chapter is designed to complement the research specific theory at the start of each experimental chapter (chapters 4-7).

Chapter 3: This chapter gives an overview of the instruments and main techniques used in the fabrication and characterisation of the sensors developed in this thesis that have promise as niche sensors for compact and harsh conditions.

Chapter 4: The humidity response of a set of polymer coatings are trialled on existing glass-based fibre Bragg gratings. Here the effects of coating thickness and optical fibre diameter are investigated. A synthesised coating is tested and insights to structural modifications to enhance humidity response are proposed.

Chapter 5: The investigation of the fibres developed in the previous chapter is continued with time response to a humidity step change observed. A two layer model for modelling fibre coating time response is proposed. The absorption and desorption diffusion coefficients for each coating are estimated using a mesh model solving the diffusion equation.

Chapter 6: This chapter details the fabrication of the planar dye-doped polymer film sensors. Combinations of various dyes and polymers are trialled with Bragg reflections observed. The reflection is refined by optimising the cladding and waveguide dimensions with special attention given to the phase mask positioning. The sensor is coupled with a single-mode silica fibre held in place with a

custom built housing unit giving it mobility and allowing integration with existing optical components.

Chapter 7: Here the optical film sensors developed in the previous chapter are tested for their strain, temperature and chemical sensing response. This work is divided into three major sections. The first section investigates the humidity and temperature response using a calibration chamber to cycle relative humidities for a set of temperatures. The effect of multiple cycles at the same temperature is also reported. The second section investigates the sensors response to chemical species where detection of DNT, an analogue of the explosive TNT, is trialled. The final section investigates the strain response by cycling hanging free weights of different masses off the film to calibrate the strain response. The breaking strain of the film is determined by loading the film to failure.

The important findings and future directions of this work are outlined in chapter 8.

Chapter 2

Basic Concepts

2.1 Introduction

This chapter provides a basic introduction to the fundamental theory used in this thesis. It is designed to complement the applied theory given at the start of each of the experimental chapters 4-7. Optical fibre communication systems transmit and receive a large amount of information quickly and accurately, they are an important part of a modern country's infrastructure.

2.2 Fibre optics

2.2.1 Optical fibre

An optical fibre consists of a core, where the guided light propagates, surrounded by a cladding with a coating layer provided for fibre strength (Fig 2.1). For light to be coupled into a fibre, the incident light must fall within the fibre's acceptance cone where it will be totally internally reflected and supported as a light mode. Light outside the cone will not be supported, and is quickly lost by leaking out of the fibre (Fig 2.2). The numerical aperture (NA) is a useful parameter to describe the acceptance cone. For a fibre this is given by equation 2.1, where θ_a and θ_c are the acceptance cone and critical angle respectively and n_{core} and n_{clad} are the refractive index of the core and cladding respectively. Optical fibres have been extended from the original glass fibres to polymer fibres. Although these fibres have a higher attenuation loss they are a cheaper alternative for short distances [1, 4–6].

$$NA = sin\theta_a = \sqrt{n_{core}^2 - n_{clad}^2} \tag{2.1}$$

2.2.2 Optical modes

Light, as an electromagnetic phenomenon, propagates along an optical fibre according to Maxwell's equations. The solutions to the propagation equations give the optical modes of the light wave within the fibre cavity. The number of light

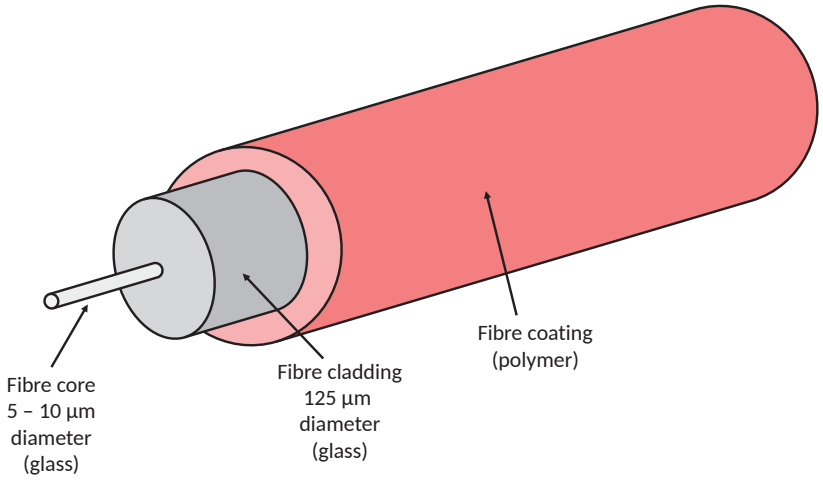


Figure 2.1 – Optical fibres comprise of a core, where the light propagates, bounded by a cladding with a coating applied to allow handling. Single-mode fibres have core diameters typically between 5 - 10 μm, while multi-mode fibres are either 50 or 62.5 μm in diameter. Both are surrounded with the standard 125 μm diameter glass cladding. Today optical fibre is made out of either glass or polymer [4, 6].

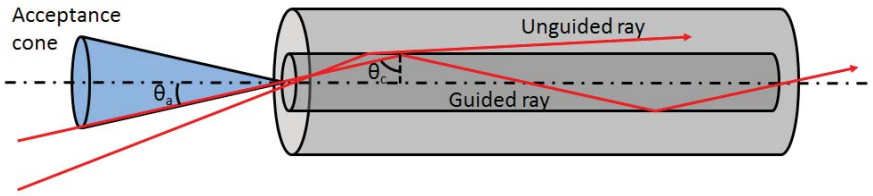


Figure 2.2 – Basic operating principle of an optical fibre. Light entering the fibre within the acceptance cone, exceeds or equals the critical angle required for total internal reflection and is guided within the fibre [5].

modes supported by the fibre depends on the diameter of the core and the refractive index contrast between the core and its cladding. It is single-mode if one mode is supported and multi-mode for more than one mode (Fig 2.3) [5].

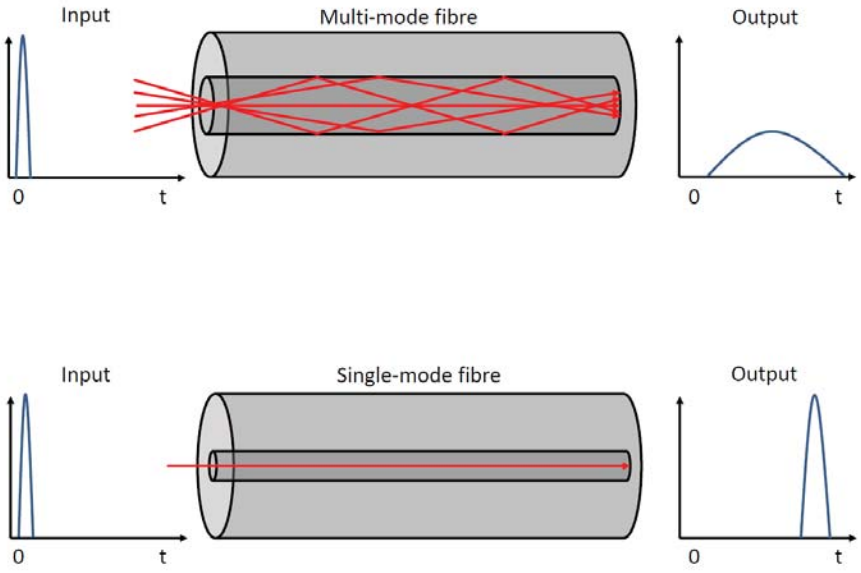


Figure 2.3 – Modes supported in an optical fibre. The input pulse was blurred during multi-mode propagation due to group velocity dispersion, while its pulse shape was retained during single-mode propagation [4, 5].

If the fibre radius or refractive index contrast between the core and cladding is large, then multiple modes can be supported by the fibre. The total number of possible modes, M, in a fibre can be estimated by equation 2.2. The V parameter is given by equation 2.3, where a is the core radius of the fibre and λ_0 is the wavelength of the light being guided [5].

$$M \approx \frac{V^2}{2} \tag{2.2}$$

$$V = 2\pi(\frac{a}{\lambda_0})NA \tag{2.3}$$

In practice the number of modes excited and supported in a fibre depends largely on the angle of the input light. The supported modes travel with different group velocities*, this results in the pulse spreading which linearly increases with length of the fibre. This is a problem for optical communication over a large distance as the information becomes distorted. One method to reduce this dispersion for multi-mode fibres is to use graded index (GRIN) fibres. However, in practice all long distance optical communications are done using single-mode fibres to minimise information loss [5].

All supported modes will experience chromatic dispersion from two effects.

*The group velocity of a wave is the velocity with which the overall shape (modulation or envelope) of the waves' amplitudes propagates through space.

The dominant effect is material dispersion from the dependence of refractive index on wavelength and the minor effect is waveguide dispersion from the dependence of group velocity [5].

When the core radius, a, and numerical aperture, NA, are sufficiently small such that $V < 2.405$, then only a single-mode is supported. There will be a minimum core radius required to support a light mode, and below this no light can be supported by the waveguide. This equation only approximates the single-mode dimensions and other methods should be used for a more accurate estimate [5, 7]. Recent advancements in micro-structured polymer optical fibres have allowed the development of single-mode polymer optical fibres [6].

The concepts for cylindrical optical fibres can be extended to square optical waveguides. The number of modes is given by equation 2.4. The numerical aperture is the same as that of a cylindrical optical fibre, equation 2.1, and d is the width of the waveguide [5].

$$M \approx 2\pi^2 \frac{a^2}{\lambda_0^2} NA^2 \tag{2.4}$$

In this thesis the single-mode dimension range for square optical waveguides were determined numerically using the method in reference [7].

2.3 Fibre optic sensors

Fibre Optic Sensors (FOSs) owe their existence to the development of the laser and low-loss optical fibre in the 1960s. Both were built on the decades earlier predecessors of the microwave laser (maser) and short length low transparency fibres [8]. Although ubiquitous with telecommunications today, the first applications of optical fibre were as sensors and by the early 1970s experiments developing the first FOSs were well under way [8, 9]. Presently they remain a topic of intensive research, with progress leading to commercial products sold for niche applications [10]. This market is valued at around US$600 million/annum in 2000, with leading user industries including military, aerospace, power generation, petrochemical, process, civil structures, environment and healthcare [8]. For these industries the FOSs are used to measure temperature, strain, pressure, vibration, current and voltage [10]. Temperature sensing has been the most successful application, where they are used as either point, distributed or quasi-distributed sensing systems (Fig 2.4) with fibre lengths extending to tens or hundreds of kilometers [8].

Niche applications have been extended to the nuclear industry, where the sensors have been shown to be immune to high radiation doses [8, 11]. Current research is focused on gas and chemical sensing where the sensors have had the

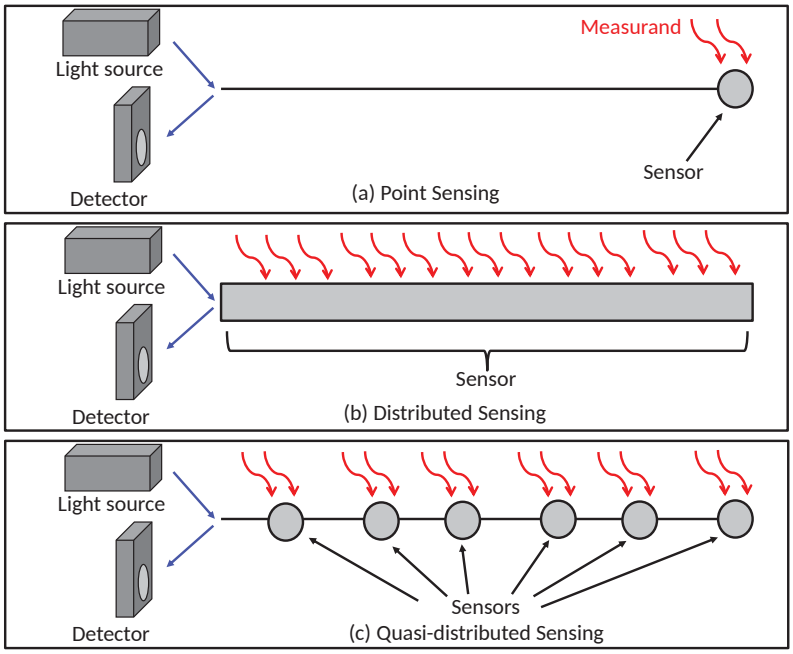


Figure 2.4 – Fibre optic sensors arranged in (a) point, (b) distributed and quasi-distributed sensing configurations [8].

least success [10]. Today the design of fibre optic sensors is so varied that the only thing they have in common with each other is the optical fibre [8, 12–14].

2.4 Fibre optic sensors' classification

As fibre optic sensors are so numerous and varied they are divided into classes of extrinsic or intrinsic sensors, depending on the position of the transducer. The transducer is the sensing part of the fibre optic sensor. It is the location where the system has been designed in order to allow an external physical phenomenon to interact with the light propagating in the fibre [15]. The sensors can be subsequently sub-grouped based on their mode of operation.

2.4.1 Extrinsic sensors

An extrinsic fibre optic sensor is one in which the light is removed from the optical fibre, acted upon by the transducer, and then coupled back into the same fibre or a separate fibre (Fig 2.5) [16]. Examples of this type of sensor are given in Fig 2.6a.

2.4.2 Intrinsic sensors

An intrinsic fibre optic sensor is one in which the light in the fibre is acted upon by the transducer without leaving the fibre (Fig 2.5) [13, 16]. Examples of this type of sensor include Fig 2.6b. One of the most successful intrinsic sensors is the fibre Bragg grating.

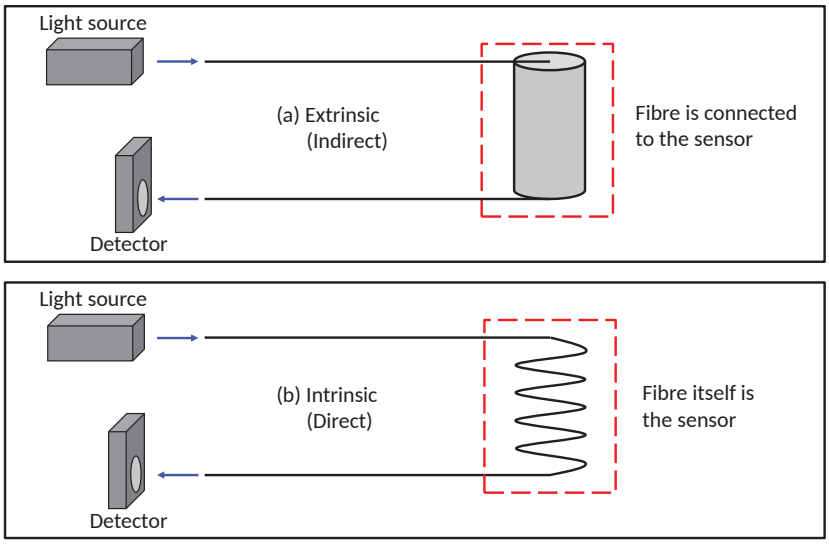


Figure 2.5 – For an (a) extrinsic sensor the optical fibre is not the sensor - it just transports light to and from the sensor, while an (b) intrinsic sensor the optical fibre is the sensor.

2.5 Fibre Bragg gratings

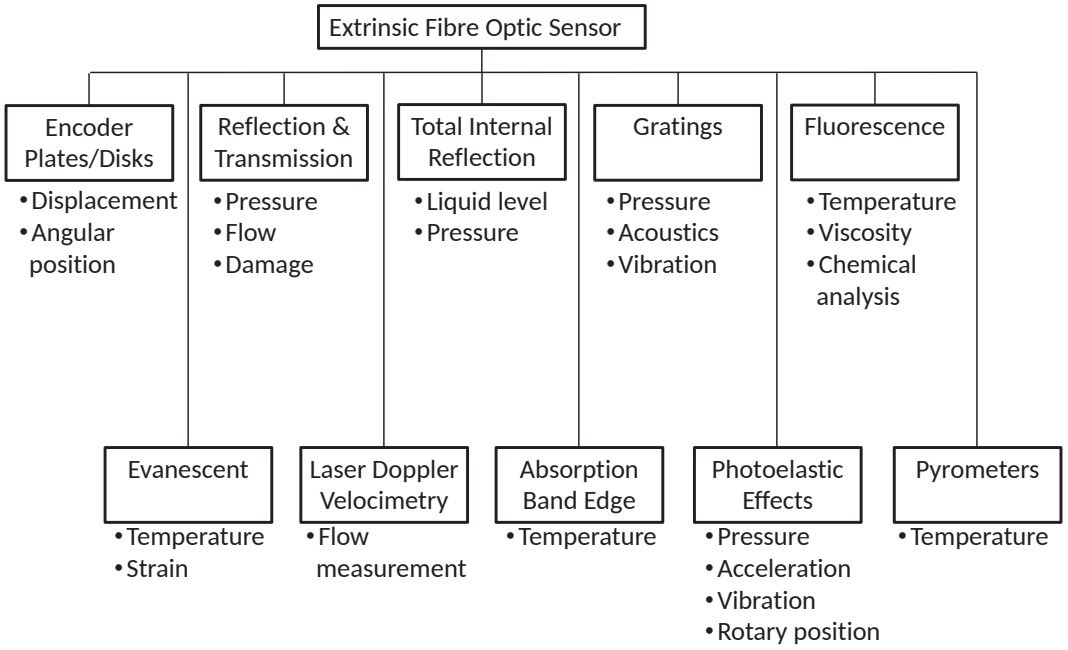
2.5.1 Basic theory

Fibre Bragg Gratings (FBGs) were discovered by Ken Hill in 1978 when a UV laser was propagated in a photosensitive fibre, where it formed an interference pattern that lead to a permanent refractive index modulation in the fibre core. This was due to the UV light altering the structure of the glass, permanently increasing the refractive index by the amount Δn. When a broadband pulse is propagated down the fibre a narrow wavelength band of the pulse is reflected back, while the rest is transmitted (Figs 2.7 & 2.8). The wavelength of the light reflected is called the Bragg wavelength, λ_B, and depends on the spacing, Λ_B, and effective refractive index, n_e, of the modulations, as shown by equations 2.5 & 2.6 [1, 18].

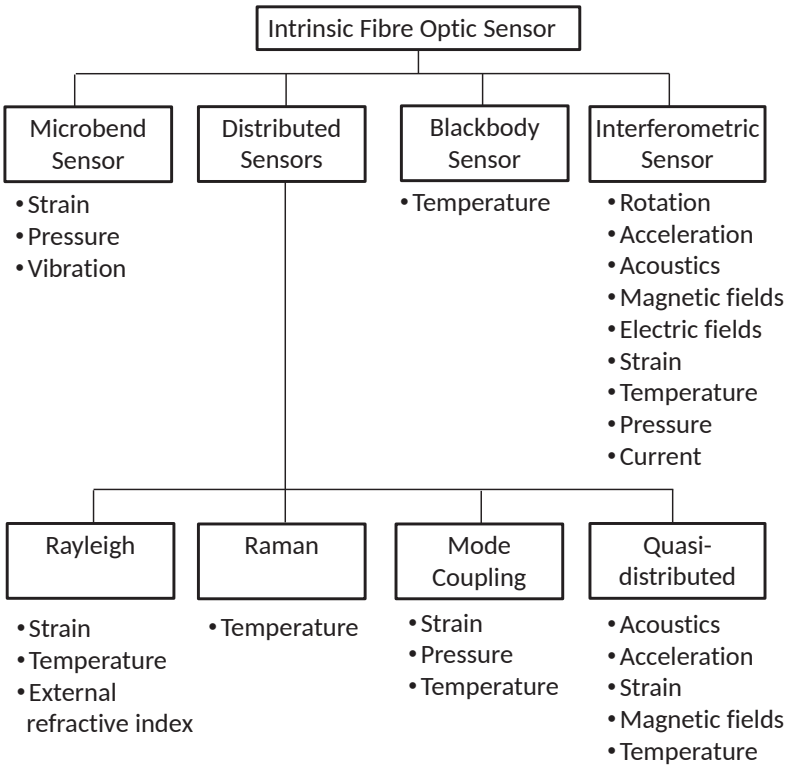
$$\lambda_B = 2n_e\Lambda_B \tag{2.5}$$

$$n_e = \frac{n_{max} - n_{min}}{2} \tag{2.6}$$

Since the initial Bragg grating written with UV light propagating down the fibre, side-on methods have been developed. Current methods of writing Bragg gratings are based on illuminating the fibre side-on with two-beam interference patterns. Phase masks are a popular method to generate a repeatable and pre-



(a) Extrinsic sensor classes.



(b) Intrinsic sensor classes.

Figure 2.6 – Classification of fibre optic sensors [17].

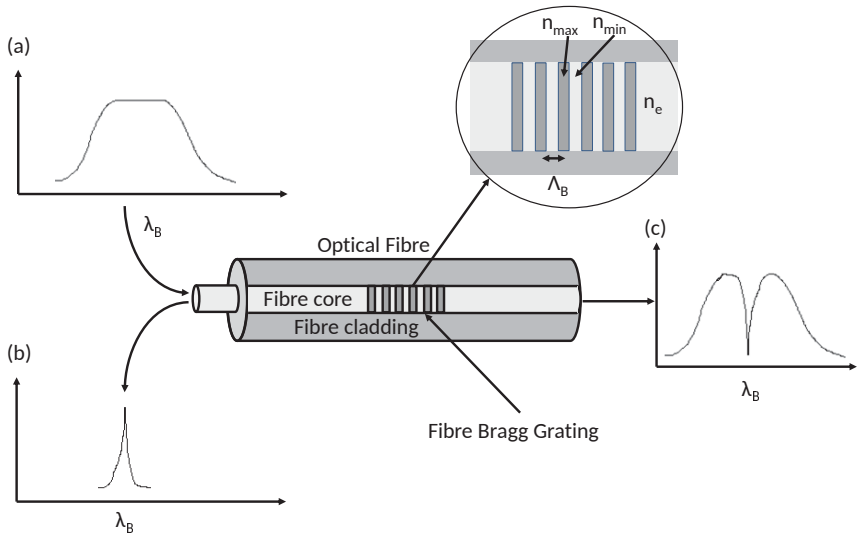


Figure 2.7 – A (a) broadband pulse propagates in a fibre core with (b) a narrow wavelength range reflected while the rest is (c) transmitted.

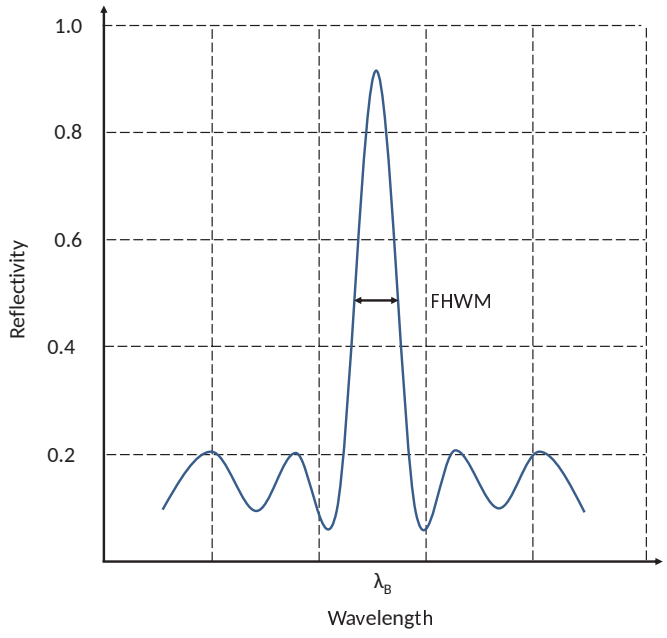


Figure 2.8 – The Bragg reflection is a narrow band of wavelengths that are reflected by a refractive index modulation. The FWHM and reflectivity are useful characteristics of a Bragg reflection. More expensive fibre Bragg gratings have higher reflectivity values. Side lobes accompany Bragg reflections due to an interference effect and can be minimised by apodization.

cise two-beam interference pattern (Fig. 2.9). This creates a uniform sinusoidal modulation in refractive index during writing [19].

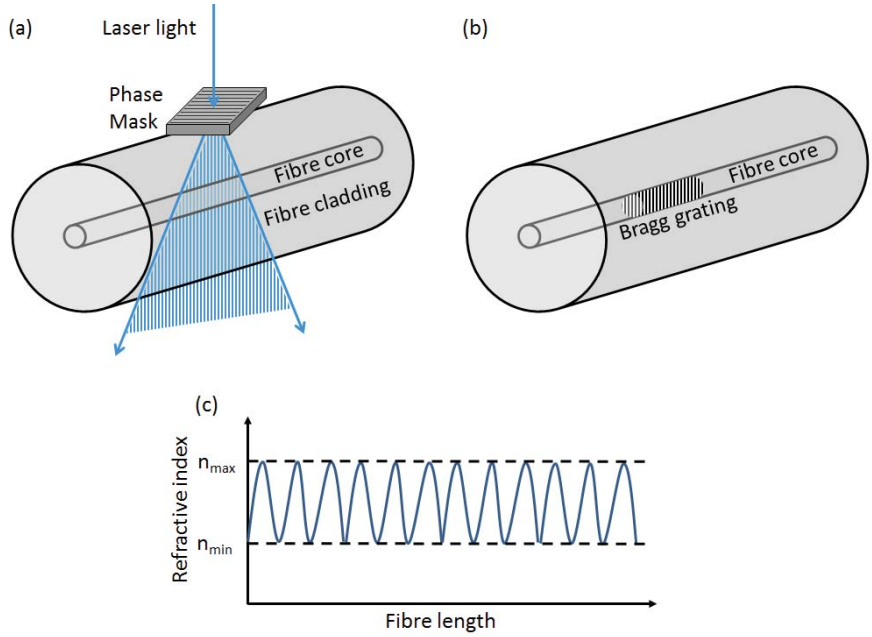


Figure 2.9 – The two beam interference pattern generated by a (a) phase mask inscribes a (b) Bragg grating by inducing a permanent (c) refractive index modulation.

For this type of index modulation the peak reflectivity, $R(l, \lambda)$, is a function of both the grating length, l, and wavelength, λ [20]:

$$R(l, \lambda) = \frac{\kappa^2 sinh^2(\gamma l)}{\Delta\beta^2 sinh^2(\gamma l) + \kappa^2 cosh^2(\gamma l)} \tag{2.7}$$

where κ is the coupling coefficient (equation 2.8), $\Delta\beta$ is the wave vector detuning (equation 2.9), β is given by equation 2.10 and γ is given by equation 2.11. Here n_0 is the average refractive index of the core and its modulations ($n_0 = n_e$).

$$\kappa = \frac{\pi \Delta n}{\lambda} \tag{2.8}$$

$$\Delta\beta = \beta - \frac{\pi}{\Lambda_B} \tag{2.9}$$

$$\beta = \frac{2\pi n_0}{\lambda} \tag{2.10}$$

$$\gamma = \sqrt{\kappa^2 - \Delta\beta^2} \tag{2.11}$$

For light at the Bragg reflection peak there is no wave vector detuning ($\Delta\beta = 0$) and this formula can be simplified to equation 2.12 [20].

$$R(l,\lambda) = tanh^2(\gamma l) \tag{2.12}$$

The Full Width Half Maximum (FWHM) of a Bragg reflection can be calculated by equation 2.13.

$$FWHM = \lambda_B S \sqrt{\left(\frac{\Delta n}{2n_0}\right)^2 + \left(\frac{1}{N}\right)^2} \tag{2.13}$$

where S is a factor which is 1 for strong gratings (near 100% reflection) or 0.5 for weak gratings, n_0 is the average refractive index ($n_0 = n_e$) and N is the number of grating planes ($N = \frac{l}{\Lambda_B}$) and l is the grating length [1]. An interesting feature is that as the induced refractive index change Δn increases, so does the FWHM. This leads to a trade off between increasing the refractive index change Δn to obtain a large reflectivity $R(l,\lambda)$ with small grating length l, while ensuring the Bragg reflection does not become unrecognisably broad.

2.5.2 Strain and temperature sensing overview

Fibre Bragg gratings are ideally suited for very accurate strain and temperature measurements, where the Bragg reflected wavelength changes from its original wavelength to a shifted wavelength. This shift in wavelength with strain or temperature changes is caused by two effects:

- The spacing between refractive index modulations change - expanding as they are strained or heated and contracting as they are compressed or cooled [1].
- The refractive index changes - increasing with strain and temperature[†].

For applied strain the modulation spacing change is the dominant effect and for temperature changes the refractive index change is the dominant effect[1, 6].

Strain sensing

By applying a stress on a material it is stretched from its original length, l_0, to an extended length, l_e. The ratio of the two lengths is the stretch ratio of the material extension, ε, given by equation 2.14.

$$\varepsilon = \frac{l_\varepsilon}{l_0} \tag{2.14}$$

If strain is applied along a fibre Bragg grating, a change in the Bragg reflected wavelength, $\Delta\lambda_B$ occurs as given by equation 2.15.

[†]For silica fibre refractive index increases with temperature while for polymer fibre the opposite is observed [6].

$$\Delta\lambda_B = \lambda_B(1 - p_e)\varepsilon \tag{2.15}$$

where the effective strain-optic coefficient, p_e, depends on the material the Bragg grating is inscribed into, with its full form given by equation 2.16.

$$p_e = \frac{n_e^2}{2}(p_{12} - \nu(p_{11} + p_{12})) \tag{2.16}$$

where p_{11} and p_{12} are the Pockels coefficients, which are components of the strain optic tensor and ν is the Poisson ratio (equation 2.17) with $d\epsilon_z$ and $d\epsilon_x$ being the change in transverse and axial strain respectively [1, 21, 22].

$$\nu = -\frac{d\epsilon_z}{d\epsilon_x} \tag{2.17}$$

Temperature sensing

Just as strain causes a change in the Bragg reflected wavelength, a temperature change,ΔT, will also shift the Bragg wavelength, with the amount of this change given by equation 2.18.

$$\Delta\lambda_B = \lambda_B(\alpha_\Lambda + \alpha_n)\Delta T \tag{2.18}$$

where α_Λ is the thermal expansion coefficient given by equation 2.19 and α_n the thermo-optic coefficient[‡] given by equation 2.20 [1, 21, 22].

$$\alpha_\Lambda = \frac{1}{\Lambda}\frac{\partial\lambda}{\partial T} \tag{2.19}$$

$$\alpha_n = \frac{1}{n_e}\frac{\partial n_e}{\partial T} \tag{2.20}$$

Some typical coefficient values for silica and polymer fibre Bragg gratings are given in Table 2.1. A much larger response to temperature than strain is observed, making it a key consideration when performing strain measurements.

Combined sensing

Because both temperature and strain can change the Bragg reflected wavelength it becomes necessary to distinguish between the two effects if they are to be accurately measured. There are multiple methods to achieve this, such as using two Bragg gratings:

- of the same material and similar wavelength - two silica FBGs ($\lambda_B = 1540$ and 1550 nm) where one grating is fixed to the object measuring strain and the other unfixed and unstrained measuring only temperature [1, 21, 25].

[‡]Polymers have a negative thermo-optic coefficient due to the predominate effect of density change with temperature, with maximum operating temperatures typically around 80 - 120°C [23].

Table 2.1 – Table of coefficients and temperature and strain sensitivity at 1550 nm.

Parameter	Si-Ge fibre [1]	PMMA [23, 24]
n_{eff}	1.5200	1.4800
Δn	1.0×10^{-4}	1.0×10^{-2}
p_e	0.2126	0.1035
p_{11}	0.1130	0.3
p_{12}	0.2520	0.297
ν	0.1600	0.34
$\alpha_\Lambda(\mathrm{K}^{-1})$	5.5×10^{-7}	7.0×10^{-5}
$\alpha_n(\mathrm{K}^{-1})$	8.6×10^{-6}	-1.2×10^{-4}
E (GPa)	73.0	3.3
Temp Sens (pm/°C)	14.2	-77.5
Strain Sens (μm/ε)	1.2	1.4

- of the same material and different wavelength - two silica FBGs ($\lambda_B = 800$ and 1550 nm) that are both fixed to the object, where a sufficiently different refractive index change in response to temperature and strain response allows the two effects to be resolved.

- of different materials and similar wavelength - one silica and one polymer FBG (λ_B = 1540 and 1550 nm) that are both fixed to the object, where a sufficiently different refractive index change in response to temperature and strain response allows the two effects to be resolved [22].

The total change in Bragg reflected wavelength is given by equation 2.21, which is the sum of both the strain contribution and temperature contribution.

$$\Delta\lambda_B = \lambda_B(1 - p_e)\varepsilon + \lambda_B(\alpha_\Lambda + \alpha_n)\Delta T \tag{2.21}$$

Both effects cause a linear response that can be exploited to distinguish between strain and temperature effects by using two fibre Bragg gratings of either a sufficiently different wavelength or material. Here different temperature (K_{1T} and K_{2T}) and strain ($K_{1\varepsilon}$ and $K_{2\varepsilon}$) responses of the fibres allow a set of simultaneous equations to be formed in a matrix (equation 2.22). The change in temperature and strain of the sensor pair in terms of the change in reflectance wavelength can be determined by inverting the matrix (equation 2.23) [1, 6, 21, 26].

$$\begin{pmatrix} \Delta\lambda_{B1} \\ \Delta\lambda_{B2} \end{pmatrix} = \begin{pmatrix} K_{1T} & K_{1\varepsilon} \\ K_{2T} & K_{2\varepsilon} \end{pmatrix} \begin{pmatrix} \Delta T \\ \Delta\varepsilon \end{pmatrix} \tag{2.22}$$

$$\begin{pmatrix} \Delta T \\ \Delta\varepsilon \end{pmatrix} = \frac{1}{K_{1T}K_{2\varepsilon} - K_{2T}K_{1\varepsilon}} \begin{pmatrix} K_{2\varepsilon} & -K_{1\varepsilon} \\ -K_{2T} & K_{1T} \end{pmatrix} \begin{pmatrix} \Delta\lambda_1 \\ \Delta\lambda_2 \end{pmatrix} \tag{2.23}$$

Although combined sensing is not studied in this thesis, this is the foundation theory for the future work incorporating combined sensing.

2.5.3 Types of fibre Bragg grating sensors

By changing the UV light interference pattern illuminating the photosensitive core of a fibre during writing, different types of fibre Bragg gratings can be created (Fig 2.10). Although the fundamental Bragg grating theory is based around uniform Bragg gratings other profiles can be used to impart unique properties to the gratings [4]. Some typical grating profiles include:

- Uniform - Both the changes in refractive index and period are uniform. This grating is formed when a uniform intensity beam is used during writing and is the most basic of the gratings and suffers from excessive side lobes to its main peak [1].

- Apodized - While the period of the grating is uniform the changes in refractive index experience a maximum in the center of the grating. This grating is formed using a raised cosine or Gaussian beam. The non-uniform changes in refractive index greatly reduce the side lobes of a Bragg reflection (Fig 2.11) [4, 27, 28]. The Bragg gratings used for the work described here are uniform apodized Bragg gratings written with a Gaussian beam.

- Chirped - The period of the grating is non-uniform. A common chirped grating has a shorter period at the start of the grating that gradually increases. This is useful for compensating for chromatic dispersion, where the longer wavelengths travel faster than shorter wavelengths in the optical fibre. They can then be recombined to preserve the pulse shape [29].

- Tilted or blazed - The grating is tilted at an angle which has the effect of generating cladding and ghost modes in addition to the main Bragg peak. The cladding modes can be used as a sensor, where refractometer and concentration sensors have been demonstrated [30, 31].

- Superstructure or sampled - This structure is formed by multiple Bragg gratings separated by un-modulated (blank) fibre, and a Fabry-Perot cavity effect occurs between the gratings. This type of grating can be used as comb filters for signal processing or for increasing the tunablity of fibre laser grating reflectors [32–34].

2.5.4 Applications

Since their inception fibre Bragg gratings have found a range of niche applications including:

- Communications - where they are used as notch filters, add-drop multiplexers and chromatic dispersion compensators [1].

- Sensors - where they have excelled in harsh and compact conditions, such as radiation immune sensors in the nuclear industry, electric field immune sensors in the electricity industry, safe sensors in explosive environments

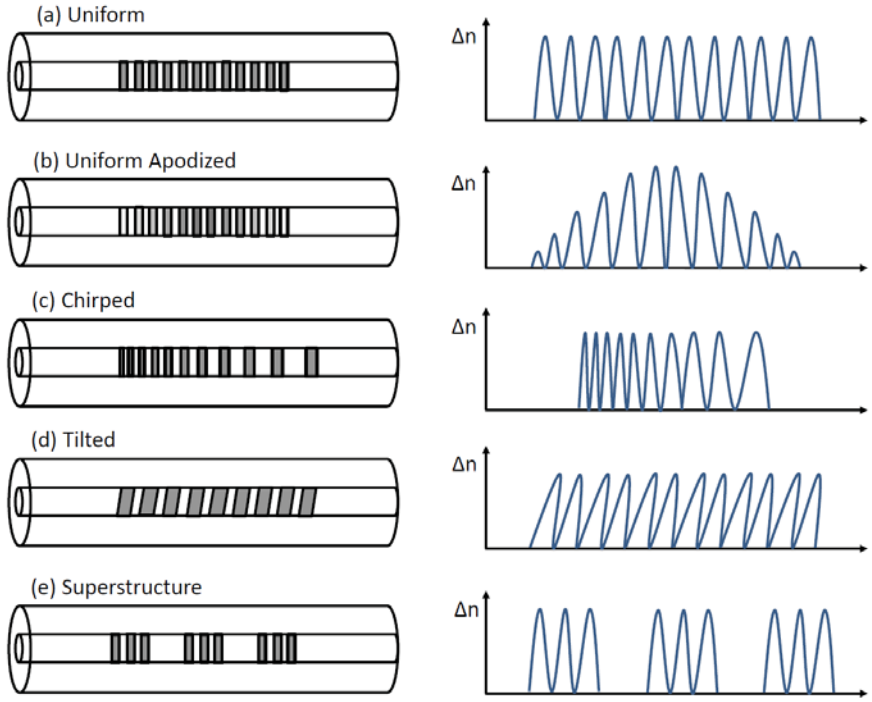


Figure 2.10 – Typical fibre Bragg grating profiles.

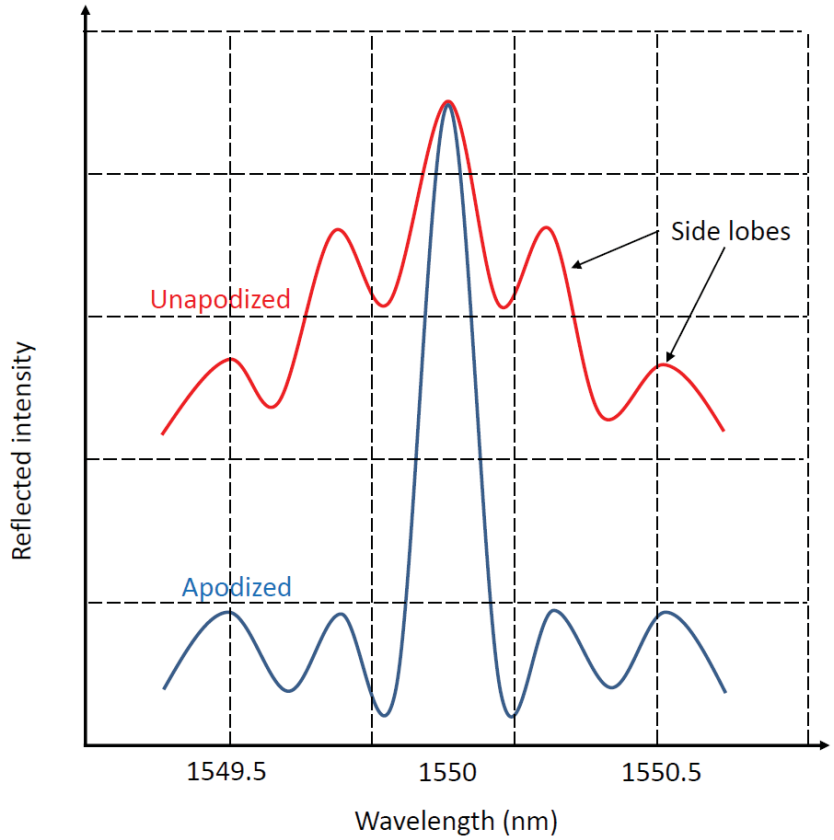


Figure 2.11 – By apodization the side lobes of a Bragg reflection can be greatly reduced.

or compact sensors in enclosed environments. Their large capacity for multiplexing and ability for remote sensing has allowed them to be excellent quasi-distributed sensors monitoring large civil structures like buildings and bridges [1, 4, 14]

• Fibre lasers - Bragg gratings can be used as the high reflector and output coupler to form the laser cavity for fibre lasers [35–37].

• Matching active and passive fibers - Bragg gratings can be used to match double-clad fibres, like a Yb-doped core signal waveguide and its inner pump light cladding waveguide [38, 39].

2.5.5 Strain tensor measurement

Although fibre Bragg gratings are ideally suited for single strain magnitude measurements, there are applications where it is necessary to determine the strain tensor. It is possible to determine this for a surface by using multiple FBGs arranged in a rosette. Typically two FBGs arranged at 45° or three FBGs at 120° with respect to one another to form rectangular or delta rosettes respectively, as shown in Fig 2.12. The rosette, together with an additional Bragg grating to correct for the temperature contribution, can be used to determine the strain tensor for a surface [40, 41]. This is also foundation theory for future work from this thesis.

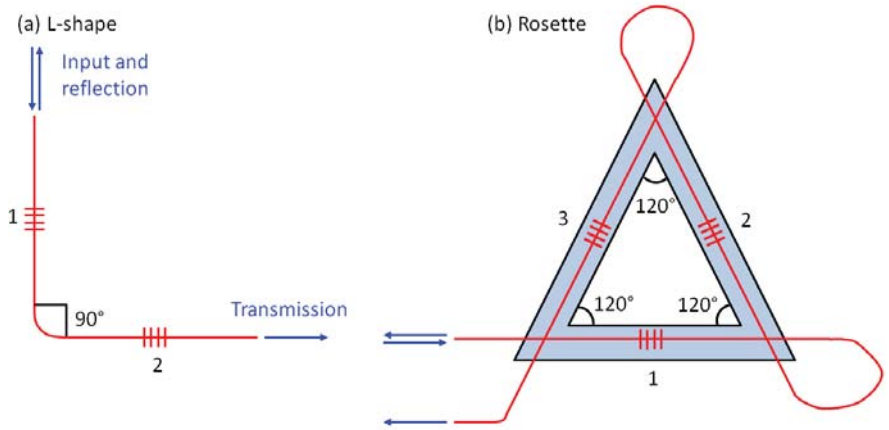


Figure 2.12 – Fibre Bragg gratings arranged in a rosette configuration for strain tensor determination.

2.6 Humidity

Humidity is defined as the water vapour content in a gas [42]. The usual measure of humidity is relative humidity which is defined as the ratio of the actual vapour pressure of air at a particular temperature, to the saturation vapour pressure at the same temperature, shown by equation 2.24 [42, 43].

$$\%rh = \frac{p_w}{p_{ws}} \tag{2.24}$$

where p_w and p_{ws} are the partial pressure of water vapour and saturated water vapour pressure respectively.

This measure expresses the water vapour content as a percentage of that required to saturate the air and form water droplets or dew. The amount of water vapour able to be held in a given volume of air is highly dependent on temperature, as the water vapour content increases significantly at higher temperatures. This makes temperature a key consideration when making humidity measurements.

2.6.1 Humidity sensing applications

The development of fibre optic humidity sensors are a strong theme in this thesis. These sensors have potential applications for measuring humidity where the conditions are unsuitable for traditional humidity sensors. These applications include:

• Structural health monitoring - this is one of the main applications of fibre optic humidity sensors. Here the sensor is presented with the harsh and compact conditions of highly alkaline concrete. Water generation is a by-product of concrete degradation; the recording of humidity in structures allows the degradation process to be tracked [44].

• Food processing and storage - the shelf life of fruit and vegetables can be maximised by storing them at an optimal humidity. This optimum humidity will be particular to each fruit and vegetable. Here a quasi-distributed fibre optic sensor would be ideally suited to simultaneously record humidity and temperature for multiple storage areas, allowing for climatic control [42].

• Medical applications - the monitoring of breathing is important during certain imaging and anaesthetic procedures. Tracking the humidity in breath can detect certain respiratory disorders like hypopnoea and apnoea. FOSs offer the potential of an accurate and compact humidity sensor [42].

• Soil humidity monitoring - the monitoring of moisture content of soil is important for horticulture to ensure optimum crop growing humidity and for mineral processing to monitor the water content in mined minerals. Here the distributed, remote, compact and accuracy features of a fibre optic sensor make it an attractive solution [42].

• Fuel water content - The variation of moisture content in fuel results in an energy uncertainty when fuel is delivered to a plant or machinery.

A fibre optic sensor could provide a non-destructive and safe method for determining the moisture content in potentially explosive conditions [42].

• Aerospace - An exciting application could be the in-situ measurements of humidity in space, such as the near surface atmospheric water content on Mars. Here the sensor would need to withstand the harsh conditions of space [42].

• Human comfort - An entire office building could have its temperature and humidity regulated using a distributed fibre optic sensing system. Humidity levels below 35 %rh cause dry eyes, throat and skin; together with high or low temperatures this makes for an uncomfortable working condition, potentially lowering productivity [42].

Chapter 3

Instruments and Techniques

3.1 Introduction

This chapter gives an overview of the instruments and techniques used in this thesis and is designed to complement the material in the experimental method sections in chapters 4-7. This overview will give a brief introduction to the important components of the instrument or technique with references where more detail can be found.

3.2 Spin coater

The preparation of thin (about 10 μm) polymer films used in chapters 6 and 7 was done by spin coating, with a detailed procedure given in chapter 6. The spin coater* shown in Fig 3.1 allowed the repeatable fabrication of high quality thin films of custom thickness between 1 and 14 μm. The film thickness was controlled by varying combinations of spin speed and solution viscosity. The glass substrates were held on the rotary stage using an external vacuum and the spin speed, acceleration and duration of spinning was controlled by the spin coater control unit [45, 46]. An additional solvent extraction unit was installed to prevent a build up of solvent fumes during coating.

3.3 Measurement of pore size

The surface area, total pore volume and average pore size of the polymer fibre coatings tabulated in chapter 5 (Table 5.1) were determined using a gas adsorption† method utilised by a Micromeritics ASAP 2010 Accelerated Surface Area and Porosimetry analyser (Fig 3.2). This unit had two preparation ports for heating samples under vacuum to remove water or remaining solvent before measurements. During a measurement the sample was under vacuum and immersed in liquid nitrogen (-195 °C), to keep a constant temperature, then a small amount

*WS-400E-6NPP-LITE from Laurell technologies corporation

†*Adsorption* is the gas molecule sticking to the surface of the polymer coating and is not to be confused with *absorption* where the gas molecule enters the polymer.

of the adsorptive gas, nitrogen, was released into the sample tube and the pressure was allowed to equilibrate, allowing the quantity adsorbed to be calculated.

A series of adsorptive amounts were dosed and then removed by vacuum enabling the quantity adsorbed at each pressure to be determined and the adsorption and desorption isotherms defined. The isotherms show the quantity of gas required to form a monolayer over the external surface of the sample, and by knowing the area covered by each adsorbed gas molecule the surface area can be calculated.

The same process was used to get information about the pore volume and size. Here the pressure was increased allowing the gas to condense in the pores where the smallest pores fill first then the bigger pores, giving a map of the pore size distribution from which the average pore size was determined. The adsorptive gas pressure was then reduced incrementally evaporating the condensed gas from the sample. By analysing the adsorption and desorption branches of the isotherms, and the hysteresis between them, information about the pore size, pore volume and surface area of the sample was revealed.

Experimentally this process was largely automated. The ASAP 2010 was computer controlled and by entering the carefully weighed dried sample amount (after rigorous heated drying under vacuum), topping up the liquid nitrogen reservoir and pressing the start button, the unit would automatically complete the above process and fit the acquired isotherm data with the appropriate model (Langmuir, BET, BJH and others) [47].



Figure 3.1 – The spin coater used to spin coat thin polymer films of custom thickness onto glass substrates.



Figure 3.2 – ASAP 2010 Accelerated Surface Area and Porosimetry analyser.

3.4 Dip coater

A custom dip coating setup was made to apply polymer coatings on the optical fibres used in chapters 4 and 5. This setup provided coatings that were uniform, repeatable and of custom thickness by controlling the solution viscosity and withdrawal speed. The immersion and withdrawal speed of a fibre into solution was controlled by a 50 mm motorised translation stage (MTS50/M-Z8) secured vertically to the bench with a bracket (MTS50-28). The motorised stage was linked to a computer via an APT-DC servo controller (TDC001), allowing the stage to be controlled with an APT user application. The components and software were sourced from Thorlabs. An in-depth theory of dip coating and details on how it was done in practice are given in the basic concepts and experimental section of chapter 4.

3.5 Measurement of thickness and refractive index

The measurement of the thickness and refractive index of the thin polymer films used in chapters 6 and 7 was performed using a Metricon 2010. For very thin ($\leq$ 2 μm) films or films that could not achieve good coupling with the Metricon 2010 prism a DekTak profilometer was used instead.

3.5.1 Metricon 2010

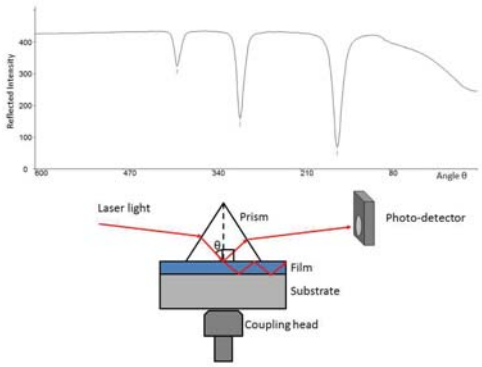
The Metricon 2010 relies on a prism coupling technique to determine the thickness and refractive index of a film. The film (while still adhered to a glass substrate) is held against a prism by a piston on a rotation stage while a laser illuminates the prism. The laser sources of 633, 1300 and 1550 nm were available for illumination to determine the thickness and refractive index. The prism coupler works by directing a laser onto one side of the prism which is then normally reflected back out the opposite side of the prism onto a photo detector. While rotating the prism on the rotation stage for certain incidence angles, called mode angles, the laser is not transmitted to the photo detector but rather couples into the polymer film (Fig 3.3). The position of the first mode determines the refractive index and the spacing to the next mode the film thickness. The Metricon 2010 was computer controlled and the rotation, detection of modes and calculation of refractive index and thickness was done automatically [45, 48]. Practically, care had to be taken not to use a laser source that would be absorbed by the film.

3.5.2 DekTak profilometer

The DekTak profilometer used for measuring the film thickness was a DekTak I manufactured by Veeco/Sloan. It has a stylus profiler that drags across the surface of the film giving a high resolution map of the surface capable of measuring film thicknesses in the range of 100 nm to 100 μm. As the stylus moves up and down



(a) The outer enclosure of the Metricon 2010 prism coupler unit that had three laser sources.



(b) A film held against the prism (below) with light coupling into the film at particular angles (above).

Figure 3.3 – The Metricon 2010 prism coupler used to measure film thickness and refractive index.

with the surface it generates a small voltage difference which formed the basis of its operation. By using a razor to neatly remove a portion of the film from the glass substrate the stylus was made to drag across the film and drop to the glass substrate where the film was cut away, giving the height of the drop and hence the film thickness. The voltage difference was converted into a thickness measurement using custom software developed in Matlab. This is a destructive method for measuring the film thickness that does not give the refractive index and was more time consuming than the Metricon 2010 prism coupler. As such it was only used as a back up method when the prism coupler was unable to make the required measurements [45].

3.6 Absorption spectroscopy

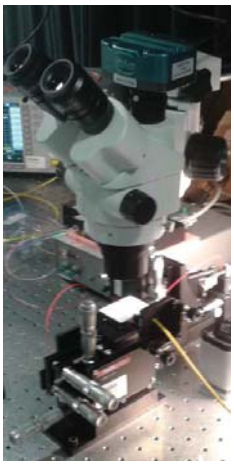
Absorption spectroscopy of the films was performed with a Lambda 1050 WB UV/Vis/NIR spectrophotometer (Fig 3.4), which allowed absorption measurements in the 175 - 3300 nm wavelength range. The light sources were a pre-aligned tungsten-halogen (Vis/NIR) and deuterium source (UV). The detectors were a grid-less photomultiplier tube (175 - 800 nm), Peltier cooled InGaAs detector (800 - 1800 nm) and Peltier cooled PbS detector (500 - 3300 nm) [45, 49]. These offered a good combination of scanning speed and wavelength range. The scanning speed was about 5 minutes per sample for a 320 - 1700 nm scan with 2 nm resolution.

3.7 Microscope

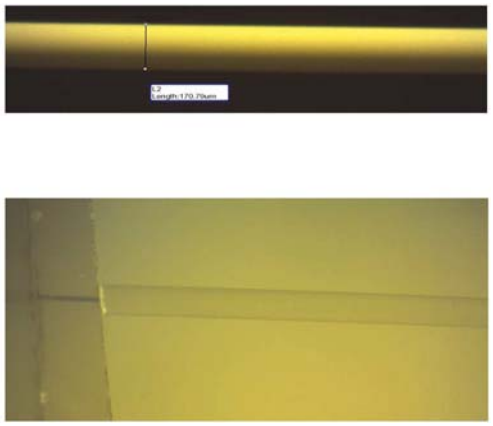
A microscope was vital for the fabrication of the polymer coated optical fibre sensors developed in chapter 4, where it was used to measure the thickness of the coatings. It was also necessary for the film sensors developed in chapter 6,



Figure 3.4 – The Lambda 1050 WB UV/Vis/NIR spectrophotometer.



(a) The microscope used with the micro-positioning stage.



(b) Pictures taken with the microscope camera.

Figure 3.5 – The Omano 2300ST microscope used for measuring fibre coating thickness and assisting with coupling alignment.

where it was used to assist with the precise alignment of the single-mode fibre for coupling (Fig 3.5). The microscope used was an Omano 2300ST GX4 zoom trinocular stereo boom microscope with a 1.5X Barlow lens and a digital microscope camera with a 0.3X C-mount adapter that was computer linked with photo and distance measuring software. The light was provided by an external lamp with an energy efficient low heat producing bulb, as temperature changes would cause an alignment shift when coupling the single-mode fibre to the polymer film.

3.8 Interrogator

An interrogator was used as the broadband light source and detector for the coated fibre humidity sensor work in chapters 4 and 5. The interrogator used was a prototype OSA 150i from Southern Photonics, which has a 1550 nm broadband light source and a Fabry-Pérot etalon based spectrometer detector (Fig 3.6). This gave it a 1500 - 1580 nm detection range and a -40 dBm minimum light reception

sensitivity [50]. It had a drift of about 100 pm that occurred as it heated up from room temperature after it was first turned on. This drift can be seen with a fibre with no coating (to remove any humidity effects) in Fig 3.8a. To account for this the unit was always left on for at least an hour before any measurements. Once fully warmed up, 100 sample points of the Bragg reflection peak were recorded to give the distribution of the readings (Fig 3.8b). More than 90% of points were covered by a 10 pm band, this was used as the error bar range in the graphs.



Figure 3.6 – The interrogator used as the broadband light source and detector for the coated fibres.

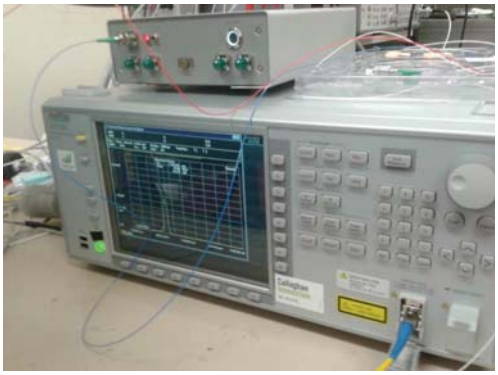


Figure 3.7 – The OSA used as the high performance detector for the film sensors and the Southern Photonics broadband light source sitting on top.

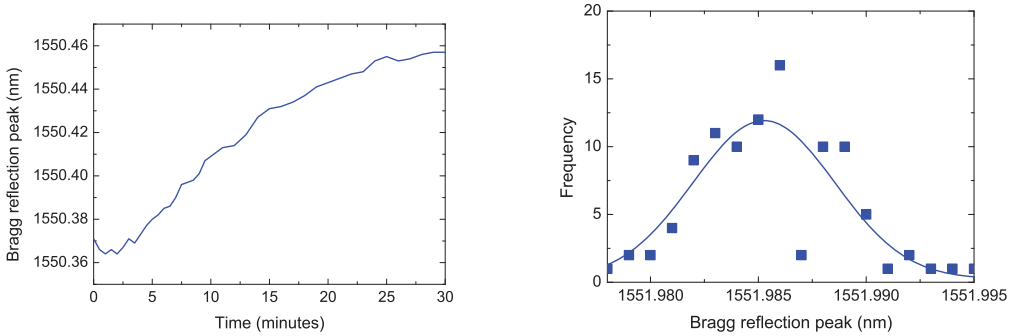
3.9 Optical spectrum analyser

An optical spectrum analyser (OSA) was used as the detector for the film sensor work in chapters 6 and 7. The OSA used was a MS9740A from Anritsu corporation and had a 600 - 1750 nm detection range, fast wavelength sweeping time (<0.2 s/5 nm), 30 pm minimum resolution and a -90 dBm minimum light reception sensitivity (Fig 3.7) [51]. This detector was preferred to the interrogator for the film sensor development in chapters 6 and 7, due to its speed and sensitivity to low powers over a large wavelength range. The OSA was computer linked with a Labview program developed to record the Bragg peak, peak width and power of multiple peaks.

3.10 Light sources

3.10.1 Broadband light sources

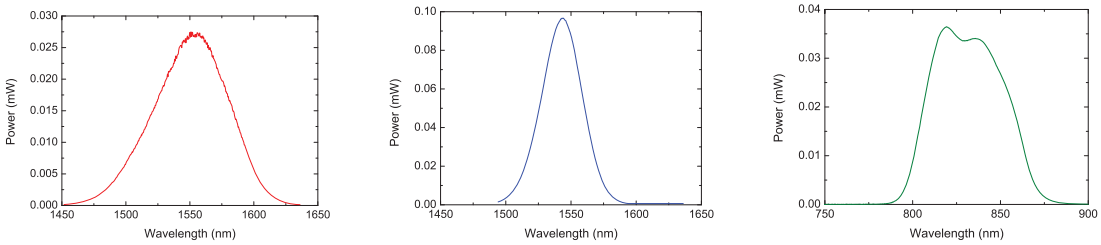
The broadband light sources used were superluminescent diodes (SLEDs). The SLEDs used in the research described here were the in-built source of the interrogator, a 1550 nm source from Southern Photonics (SP) and a 820 nm source from InPhenix. The spectra of the sources are shown in Fig 3.9 with the characteristics given in Table 3.1. A small amount of spectral ripple can be seen



(a) The wavelength drift during the start up of the interrogator, a shift of 100 pm can be seen.

(b) The frequency distribution of 100 Bragg reflection peak measurements with a Gaussian fit.

Figure 3.8 – The wavelength drift and distribution from the interrogator for a bare fibre.



(a) Interrogator source.

(b) SP broadband source.

(c) 820 nm SLED source.

Figure 3.9 – Spectra of broadband light sources.

with the interrogator spectrum when viewed with the high resolution OSA[‡]. The ripples have no detrimental effect as the interrogator was used exclusively for the coated fibre work with commercial fibre Bragg gratings that have high reflectivity. The Southern Photonics 1550 nm source had much more power over a narrower wavelength range than the interrogator source. Its peak was closer to the Bragg reflection peak of the film sensors so was the preferred source. The InPhenix 820 nm source was used for assisting fibre coupling with the films. This wavelength was chosen as it was not absorbed by the dye and, although invisible, it could be seen with the microscope camera. This greatly assisted alignment of the fibre before using the invisible 1550 nm light. SLED light can be partially or fully polarised when it is generated. However, single-mode fibres do not maintain polarisation and any polarisation is lost by the time the light reaches the sensor [52].

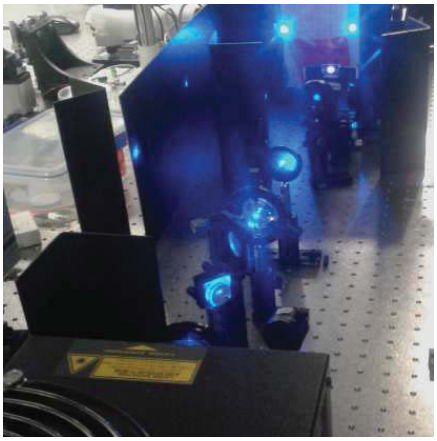
3.10.2 Lasers

The lasers used for writing Bragg gratings in dye doped films were an argon ion laser and 445 nm diode laser. A 780 nm diode laser was used to probe the efficiency of the gratings. The argon ion laser was a Melles Griot (35-LAP-431-230)

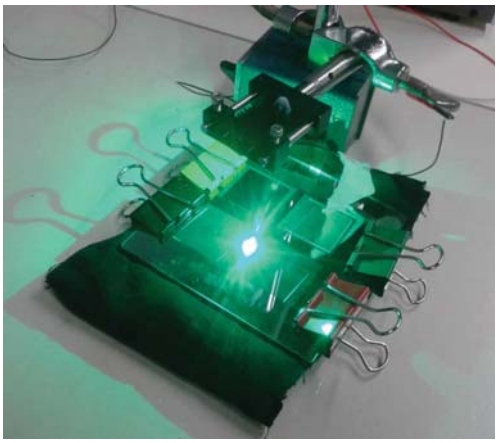
[‡]The interrogator detector did not have the resolution to detect the ripples.

Table 3.1 – Broadband light sources characteristics.

Light source	Peak (nm)	Span (nm)	Power (mW)
Interrogator source	1550	120	2.0
SP Broadband source	1545	80	4.0
InPhenix 820 nm SLED	1545	70	1.6



(a) 488 nm light from the argon ion laser writing a Bragg grating into a PYR-3 doped film.



(b) The 525 nm LED bleaching a waveguide into a PYR-3 doped film with a lithographic mask on top.

Figure 3.10 – Light sources.

43 series argon ion laser (Fig 3.10a) and the diode lasers were a 600 mW 445 nm diode laser (DHOM-M-445-600mW) and a Roithner laser technik 15 mW 780 nm diode laser (RLT7810G). The 488 nm wavelength was the preferred wavelength from the argon ion for bleaching the PYR-3 dye and 514 nm for the BAF-1 dye, as they both had a good penetration depth and absorption with each dye [45].

3.10.3 LEDs

Two LEDs were used for photo-bleaching waveguides into PYR-3 doped films, a green 525 nm and red 625 nm LED (Fig 3.10b). They were powered with a Topward electric instruments co. ltd. DC power supply (TPS-2000) with an Electus distribution 12 - 30 VDC input LED Driver (AA-0596) attachment. The LEDs were mounted 50 mm away from the film and the DC power supply set at 0.7 Amps. Both LEDs were used for photo-bleaching and both produced good quality waveguides, but red was preferred as it was faster at bleaching.

3.11 Humidity generators

3.11.1 Model 2500 Thunder Scientific humidity generator

This humidity generator was a self contained system capable of producing humidities in the range of 12 and 95 %rh at atmospheric pressure for temperatures between 0 and 70 °C [53]. The generator works by generating saturated pressurised air, which is then released through an expansion valve to atmospheric pressure in the measurement chamber where it becomes a lower relative humidity (Fig 3.11a).

This can be explained mathematically with the dew point given by equation 3.1, where $e(t_d)$ is the dew point, $e(t_s)$ is the saturated dew point, t_d and t_o are the temperatures of the dew point and current temperature of the air in the chamber and t_s is the saturated air temperature and p_o and p_s are the chamber and saturated air pressure respectively. This leads to the relative humidity (%rh) expression of equation 3.2[§]. The saturated air was passed multiple times around the temperature controlled sample chamber to ensure the saturated air was the same temperature as the chamber ($t_o = t_s$). This humidity generator had exceptional temperature stability and accuracy when producing relative humidities, which made it ideal for the humidity calibration measurements of the sensors developed in chapter 4 and 7. This humidity generator had an auto profile program that could set humidity steps to run automatically [43].

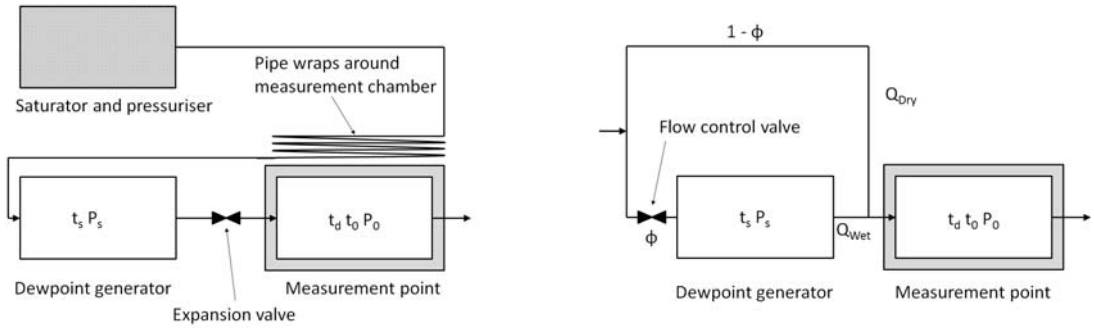
$$e(t_d) \cong \frac{p_o}{p_s} \cdot e(t_s) \tag{3.1}$$

$$\%rh \cong \frac{p_o}{p_s} \cdot 100\% \tag{3.2}$$

3.11.2 Two-flow humidity generator

This humidity generator was capable of producing humidities in the range of 5 and 95 %rh at atmospheric pressure for ambient temperature. The generator works by combining two air flows, a dry air flow generated by air passed through a column containing dry silica beads and a saturated air flow generated by water evaporation when the air was passed over a saturated material (Fig 3.11b). A small amount of evaporative cooling can occur during the generation of the saturated air, so the unit has a built in heater to compensate for this. A flow valve was used to combine the two flows to give the desired humidity with the portion of the flow expressed mathematically as equation 3.3. The relative humidity generated can be calculated by equation 3.4, where ϕ is the portion of the flow (1 for all wet flow and 0 for all dry flow) and Q_{wet} and Q_{dry} are the flow rate of the wet and dry air respectively. The flow valve allows it to be quickly switched between dry and wet air to simulate a humidity step change. This was

[§]Examples are saturated air pressurised at 5 bar being released to the chamber (1 bar) to give a relative humidity of $\frac{1bar}{5bar} = 20$ %rh. Alternatively if the air was saturated but not pressurised then the air in the chamber was saturated.



(a) Model 2500 Thunder Scientific. **(b)** Two-flow humidity generator.

Figure 3.11 – Humidity generators used for the calibration and humidity step change response.

the preferred generator for the investigating the time response of the sensors in chapters 5 and 7.

$$\phi = \frac{Q_{wet}}{Q_{wet} + Q_{dry}} \tag{3.3}$$

$$\%rh \cong \phi \cdot 100\% \tag{3.4}$$

3.12 Strain measurements

The strain measurements on the films in chapter 7 were performed by a simple method of hanging weights attached to the base of the film [54]. The weights were a set of 1, 2, 5, 10, 20, 50, 100 and 200 g slotted weights that were hung off a clip attached to the base of the film. A centre 313 humidity and temperature probe was required to account for any changes due to humidity or temperature. Up to 600 g could be loaded onto the film before the film would either break, have the glue fail or the hanger slip off the film.

Chapter 4

Humidity response of polymer coated fibre Bragg gratings

4.1 Introduction

The use of fibre Bragg gratings as humidity sensors is an emerging field. In many situations there is a need to accurately monitor humidity, often during compact and harsh conditions where traditional sensors cannot be used. Fibre Bragg gratings offer an attractive solution due to their compact size, insensitivity to high electric fields, resistance to harsh conditions and relatively low cost.

Some possible applications include structural health monitoring - where the sensor would be embedded in to concrete where it is exposed to highly alkaline and compact conditions, measuring the moisture content and temperature in power transformers - where the sensor would be exposed to a large electric fields or for domestic purposes, such as in dehumidifiers or in clothes dryers.

Unfortunately, the widespread use of fibre Bragg gratings as humidity sensors is currently limited by the highly expensive high performance interrogation units that are needed to measure the small wavelength changes of a fibre Bragg grating humidity sensor. If a highly-humidity responsive coating could be developed, without compromising selectivity, then a low cost interrogation unit could be used. Many research teams in the world are currently working on providing low cost interrogation units. In addition, using a highly-humidity responsive coating with a high cost interrogation unit would enable highly precise humidity measurements to be made. Therefore, there is a need to study and understand in depth the humidity response of coatings on fibre Bragg gratings and the different parameters affecting their humidity response.

In this chapter a range of polyetherimide (PEI), poly(methyl methacrylate) (PMMA), polyimide (PI) and default factory coatings on fibre Bragg gratings were investigated and compared to an existing dielectric commercial humidity sensor, with humidity response as a function of change in Bragg wavelength reported. The results guide the development of novel polymer coatings suited for humidity

sensing.

4.2 Basic concepts

This section will outline some of the important concepts of this chapter, building on concepts already covered in chapter 2. How fibre Bragg gratings are used as humidity sensors and some important parameters when using them will be covered. An introduction to dip coating is provided giving an insight in to the requirements needed to get a good quality fibre coating.

4.2.1 Bragg gratings as humidity sensors

Fibre Bragg gratings can be used to sense changes in humidity by coating the optical fibre with a humidity sensitive polymer. As the relative humidity ψ^* of the surrounding air increases, the polymer swells as it absorbs water. This strains the underlying optical fibre housing the Bragg grating shifting the dry Bragg reflection, λ_B, by amount $\Delta\lambda_B$ (Fig 4.1) [55].

Ideally this coating would apply a large strain on the underlying fibre, respond linearly, be reversible without hysteresis, low cost and not degrade with water. Although the requirement for reversibility may not be strictly necessary. For certain one time use applications, such as monitoring transformer oil quality where the monotonically increasing water content in the oil indicates when the transformer is nearing the end of its useful life.

4.2.2 Coefficient of moisture expansion and sensitivity

The coefficient of moisture expansion (CME) is defined as the fractional increase in strain per unit mass variation due to the moisture desorption or absorption. The CME is determined by measuring the moisture content change and the strain change between two moisture equilibrium states. This is an important parameter for a coating based fibre Bragg grating humidity sensor as it is the strain transfer from the swelling due to humidity that determines the sensors sensitivity.

Only the strain transfer along the axis of the fibre is measurable, the polymer will also swell perpendicularly to the fibre which will not cause any measurable strain on the fibre (equation 2.15). The general equation for the coefficient of moisture expansion in a single direction is given by equation 4.1 [56].

$$CME = \frac{\left(\frac{\Delta l}{l_{ref}}\right)}{\left(\frac{\Delta m[\%]}{m_{ref}[\%]}\right)} \tag{4.1}$$

*Where the units %rh refer to the relative humidity expressed as a percentage

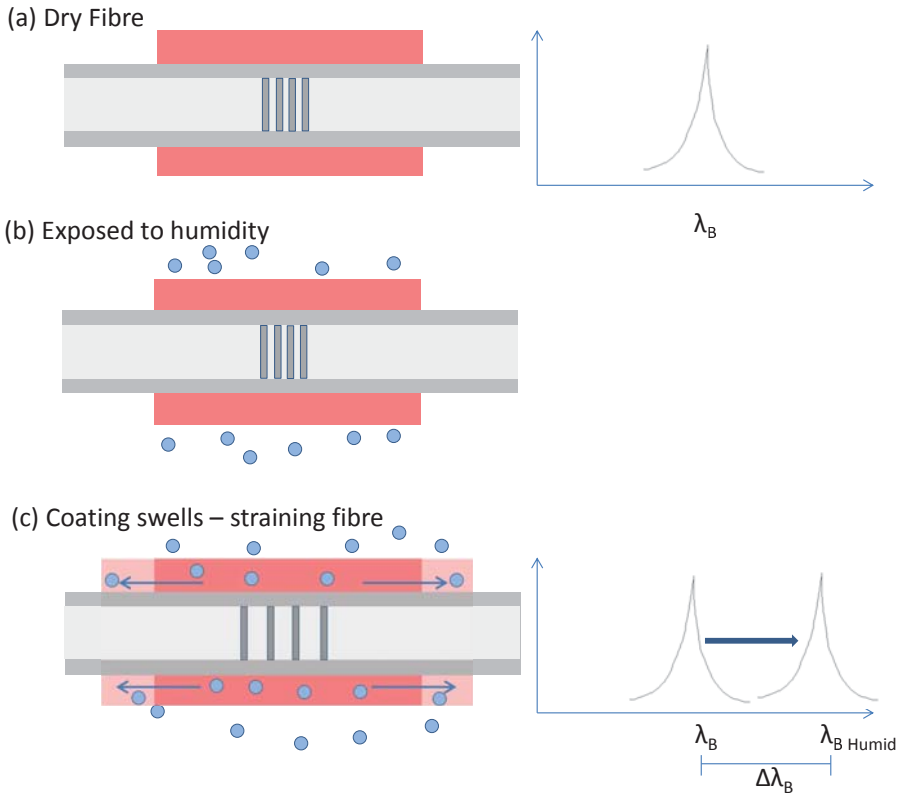


Figure 4.1 – A coated fibre Bragg grating senses humidity (blue circles) by the coating (red) expanding (light red) and straining the underlying cladding (dark grey) and core (light grey) containing the Bragg grating (dark grey rectangles). This process is shown by (a) fibre Bragg grating in dry conditions with a dry Bragg reflection wavelength of λ_B, (b) the fibre being exposed to moisture and (c) the moisture is absorbed by the fibre coating straining the underlying fibre shifting the Bragg reflection wavelength to $\lambda_{B\ Humid}$. The fibre core is expanded for clarity and is not to scale.

where l_{ref} is the original length of the polymer coating, Δl is the change in length of the polymer coating, $m_{ref}[\%]$ is the percentage moisture in the original state and $\Delta m[\%]$ is the percentage moisture in the final state.

The coefficient of moisture expansion of a polymer coating on a fibre Bragg grating can be determined by measuring the swelling response to changes in humidity.

For fibre Bragg gratings acting as humidity sensors, the standard relationship (equation 4.2) can be modified (equation 4.3) if the only strain on the fibre is due to the polymer coating swelling or contracting with humidity changes [55].

$$\frac{\Delta\lambda_B}{\lambda_B} = (1 - P_e)\varepsilon_z + [(1 - P_e)\alpha_\Lambda + \alpha_n]\Delta T \tag{4.2}$$

here λ_B is the original Bragg reflection peak, $\Delta\lambda_B$ is its shift with relative humidity $\Delta\psi$ and temperature ΔT changes, P_e is the effective strain optic coefficient, α_Λ is the thermal expansion coefficient of the fibre and α_n is the thermo optic coefficient of the fibre [1, 55]. Only strain along the fibre axis is measured.

$$\frac{\Delta\lambda_B}{\lambda_B} = (1 - P_e)\varepsilon_{rh} + [(1 - P_e)\varepsilon_T + \alpha_n]\Delta T \tag{4.3}$$

where ε_{rh} and ε_T account for the polymer coating induced strain on the fibre due to relative humidity and temperature changes respectively. In terms of these changes, ε_{rh} and ε_T can be expressed as equation 4.4 and equation 4.5.

$$\varepsilon_{rh} = [\frac{A_p E_p}{A_p E_p + A_f E_f}][CME_p(\psi) - CME_f(\psi)]\Delta\psi \tag{4.4}$$

$$\varepsilon_T = [\frac{A_p E_p}{A_p E_p + A_f E_f}][CTE_p(T) - CTE_f(T)]\Delta T \tag{4.5}$$

Here A_p and A_f are the cross sectional area of the polymer and fibre respectively, E_p and E_f are the Young's modulus of the polymer and fibre respectively as illustrated in Fig 4.2, $CME_p(\psi)$ and $CME_f(\psi)$ are the coefficient of moisture expansion (CME) of the polymer and fibre respectively and $CTE_p(T)$ and $CTE_f(T)$ are the coefficient of thermal expansion (CTE) of the polymer and fibre respectively.

As the glass optical fibre does not absorb water, $CME_f(\psi)$ is assumed to be zero [55]. For constant temperature, equation 4.3 can be rewritten as equation 4.6 which is then substituted in equation 4.4 to give the expression of equation 4.7.

$$\frac{\Delta\lambda_B}{\lambda_B} = (1 - P_e)\varepsilon_{rh} \tag{4.6}$$

$$\Delta\lambda_B = \lambda_B(1 - P_e)[\frac{A_p E_p}{A_p E_p + A_f E_f}]CME_p(\psi)\Delta\psi \tag{4.7}$$

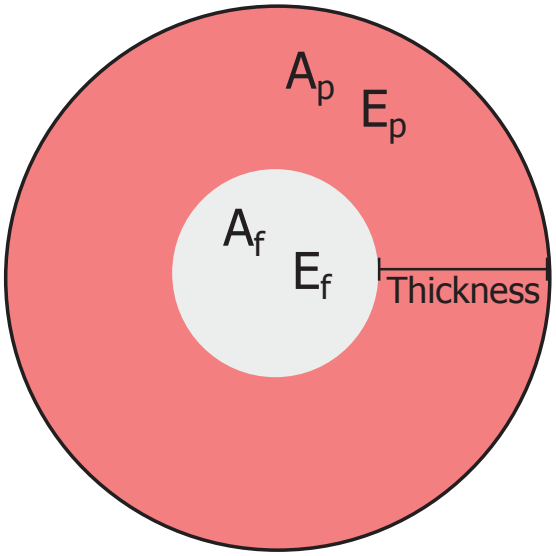


Figure 4.2 – Cross section of a coated optical fibre with the red area representing the polymer coating and light grey area representing the optical fibre. A_p and A_f are the cross sectional area of the polymer and fibre respectively and E_p and E_f are the Young's modulus of the polymer and fibre respectively. The thickness of a coating is defined as the distance between the edge of the optical fibre and edge of the polymer coating.

By making a linear plot of $\Delta\lambda_B$ versus $\Delta\psi$, the slope can be used to experimentally determine the coefficient of moisture expansion.

This model assumes that there is perfect adhesion between the coating and the glass optical fibre allowing for prefect strain transfer; in practice this is not the case.

An important parameter when using fibre Bragg gratings as humidity sensors is the sensitivity. The coefficient of moisture expansion is an intrinsic property of a coating - it should have the same value regardless of the coating thickness or diameter of the optical fibre it is adhered to. The same can not be said about sensitivity - it is an intrinsic property of the sensor and is highly dependent on the coating thickness and diameter of the optical fibre.

The sensitivity of a fibre Bragg grating can be given as a sum of relative humidity sensitivity, S_{rh}, and temperature sensitivity, S_T (equation 4.8). By substituting this into equation 4.3 the sensitivity coefficients can be determined (equation 4.9 and equation 4.10) [57, 58].

$$\frac{\Delta\lambda_B}{\lambda_B} = S_{rh}\Delta\psi + S_T\Delta T \tag{4.8}$$

$$S_{rh} = (1 - P_e)[\frac{A_pE_p}{A_pE_p + A_fE_f}]CME_p(\psi) \tag{4.9}$$

$$S_T = (1 - P_e)\left[CTE_f(T) + \frac{A_pE_p}{A_pE_p + A_fE_f}\right](CTE_p(T) - CTE_f(T)) + \alpha_n \tag{4.10}$$

4.2.3 Dip coating theory

Dip coating is a simple process for depositing a thin film of solution onto cylinder, for example a glass optical fibre, or any other shaped object. As the geometry of the coated object can vary so widely, this is a distinguishing feature of dip coating. The process of dip coating can be separated into five sequential stages [59]:

- Initial immersion - the substrate is dipped in to a reservoir of solution in a controlled way with constant speed.
- Settling and surface wetting - the substrate is allowed time to settle and the surface left to fully wet.
- Solution deposition - the substrate is withdrawn from the solution in a controlled way with constant speed and a thin layer of solution is deposited on the surface of the substrate. This is illustrated by Fig 4.3.
- Excess solvent drainage - the excess liquid drains from the surface due to gravity.
- Solvent evaporation - the remaining solution after drainage has the solvent evaporate leaving a uniform dry coating.

There are several forces involved in the film deposition - viscous drag, gravitational force, capillary force (the resultant force of surface tension) and inertia force. The viscous drag force is the force that moves the solution up with the substrate when it is withdrawn, it is proportional to the solution viscosity and withdrawal speed. The gravitational force drives the solution downwards and is responsible for draining excessive liquid from the substrate. The surface curvature at the base is caused by surface tension, this effect lowers the pressure in the liquid beneath the curved meniscus near the the solution reservoir and produces a downward capillary force in the same direction as gravity. The inertia force is the force the solution has to resist a change in motion.

These forces were modelled by Landau and Levich using the hydrodynamics of a Newtonian fluid flow, ignoring solvent evaporation, resulting in equation 4.11 [59, 60].

$$h_0 = 0.944 \frac{(\eta u_0)^{\frac{2}{3}}}{\sigma^{\frac{1}{6}}(\rho g)^{\frac{1}{2}}} = 0.944(Ca)^{\frac{1}{6}} \left(\frac{\eta u_0}{\rho g}\right)^{\frac{1}{2}} \tag{4.11}$$

Where h_0 is the limiting coating thickness, u_0 is the withdrawal speed, η is the solution viscosity, ρ is the solution density, σ is the solution surface tension and Ca ($= \frac{\eta u_0}{\sigma}$) is the capillary number. The most important parameters influencing the coating thickness are the solution viscosity and the withdrawal speed. Limitations to this model occur when the solvent drainage and evaporation stages overlap, incorporating the effect of solvent evaporation is mathematically demanding. Adaptations to this model can be made by applying a multiplication factor, depending on the solvent used and its evaporation rate.

By using hot air drying while dip coating it was possible to minimise the overlap between the solvent draining and coating drying stages, which can cause an uneven coating. A thinner coating was also achieved when a solvent saturated atmosphere was used and any unevenness on the surface of the substrate itself will result in significant thickening of the coating [59, 61].

Although equation 4.11 is not directly used in this research, it gives an insight in to important considerations to be aware of while using dip coating. The withdrawal speed, solution viscosity, covering of the solution reservoir and the use of hot air drying all play an important role in achieving uniform and repeatable coatings. In practice, trial and error was used to obtain the desired coating.

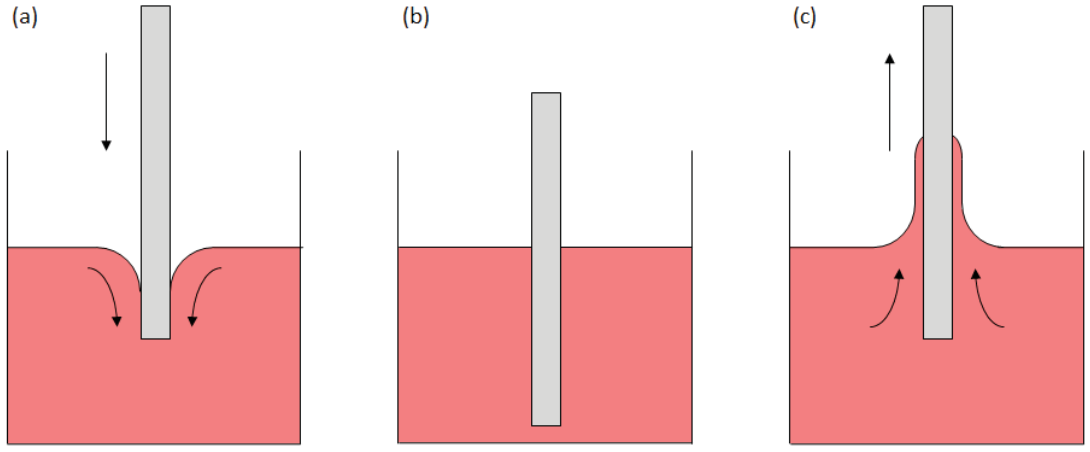


Figure 4.3 – Schematic of dip coating process (a) initial immersion, (b) settling and surface wetting and (c) solution deposition.

4.3 Fibre preparation

The fibre Bragg gratings used in this work had Bragg gratings in the range of 1540 and 1550 nm with acrylate (FOSSCXC4712) or polyimide (FOSS3DXC7324)

coatings purchased from Avensys and acrylate and ormocer (DTG-LBL-1550) coatings from Draw Tower Gratings. Before coating the fibres the original factory coating was stripped off and the surface cleaned with an adhesion promoter applied. The polymer was then dip or spray coated onto the fibre and oven dried before humidity experiments conducted.

4.3.1 Stripping fibre coatings

A typical optical fibre comprises of a core, where the guided light propagates, surrounded by a lower refractive index cladding to contain the light in the core. Both the core and cladding are glass, where the core is doped glass[†] to give it a higher refractive index. The cladding diameter is usually only 125 μm, so a coating layer is needed to give it strength. Common coatings include acrylate, ormocer (organically modified ceramic) and polyimide coatings. Some manufacturers also include a jacket layer to give the fibre extra resistance to its environment.

There are two general methods to strip a fibre - mechanical stripping and chemical stripping. Depending on what the factory coating was, one method may be preferable over the other. Mechanical stripping was done using a Miller dual hole optical fiber stripper (FO 103-D-250). Only a single strip can be made with the optical fiber stripper, as double stripping often resulted in the fibre breaking. Chemical stripping was done by either soaking the fibre in dichloromethane (DCM) at room temperature or soaking the fibre in concentrated sulfuric acid heated to 130 °C[‡]. After stripping a Kimwipe with a few drops of isopropyl alcohol was used to wipe the stripped fibre removing any remaining coating.

Some coatings are easier to strip than others. The easiest coating to strip was an acrylate coating, that was easily stripped by chemical stripping with DCM or mechanical stripping. Although it was possible to strip ormocer coatings chemically with DCM it was far easier to use mechanical stripping. The hardest coatings to strip were polyimide coatings. These have a tendency to form knots while mechanically stripping, causing the underlying glass fibre to break. It also had excellent chemical resistivity to solvents. The best way to strip polyimide coated fibres was chemical stripping with hot concentrated sulfuric acid.

The original factory coating puts the optical fibre under strain when it is coated onto the fibre - this strain is released when stripping the coating, typically shifting the Bragg reflection 250 pm to longer wavelength.

[†]Photosensitivity was originally observed in Germanium doped glass. Although now a range of other dopants have been shown to exhibit it also [1].

[‡]When soaking the fibre in hot concentrated sulfuric acid the stir bar in the acid must be turned off, as the fluid motion caused by the stir bar causes a drag on the stripped optical fibre that can cause it to break.

4.3.2 Surface cleaning

To prepare the fibre for the application of an adhesion promoter the surface of the cladding must be rigorously cleaned. Cleaning was done by soaking the fibre in piranha solution (7 parts concentrated sulfuric acid and 3 parts 30% hydrogen peroxide solution) for 30 minutes, then dipping the fibre into distilled water before a final wipe with a Kimwipe soaked with a few drops of isopropyl alcohol. Extreme care must be taken when using piranha solution, only a small scale amount of 10 mL in a test tube was used with the hydrogen peroxide being added drop-wise to the acid in a fumehood, allowing the heat and vapours generated to dissipate safely.

To dispose of the used piranha solution it was first left overnight to deactivate, then the solution was poured into a large beaker of water to dilute it. The diluted piranha solution could be either poured down the sink with a copious amount of water or stored in a plastic container without a lid for hazardous waste collection. It is extremely important not to use a lid if storing in a plastic container as the solution can produce gas which will put a closed container under pressure that could possibly cause an explosion [62].

4.3.3 Adhesion promoter

An adhesion promoter can be used to promote the adhesion of polymer coatings to the glass optical fibre. The adhesion promoter forms a mono layer on the glass by reacting with the glass surface forming a covalent bond. It subsequently reacts with the polymer coating forming a covalent bond with the polymer, in effect tethering the polymer to the glass cladding with covalent bonds [63]. The tethered polymer chains are entangled with untethered polymer chains (Fig 4.4). This has the potential to increase the humidity response of the coating by allowing better strain transfer of the polymer coating to the underlying glass optical fibre. It also promotes repeatability as polymer slippage on the fibre is minimised.

The adhesion promoter (3-Aminopropyl)triethoxysilane (3-APTS) (CAS: 919-30-2) was sourced from Sigma Aldrich. It must be diluted to effectively react with the optical fibre. A 0.2% by volume solution of 3-APTS in milli-Q water was freshly prepared in a non-reactive high density polyethylene (HDPE) plastic container and shaken well. This was to prevent the 3-APTS reacting with its container rather than the optical fibre. The fibre was immersed in the solution for 2 minutes, then dried in a 120 °C oven for 15 minutes to remove excess water.

The adhesion promoter solution was prepared freshly for each application as 3-APTS will spoil after 24 hours. The stock solution from Sigma Aldrich must be tightly sealed and stored in dry conditions as water will cause the active organosilane to slowly polymerise. The fibres primed with adhesion promoter can be stored up to 24 hours before coating with a polymer solution [64].

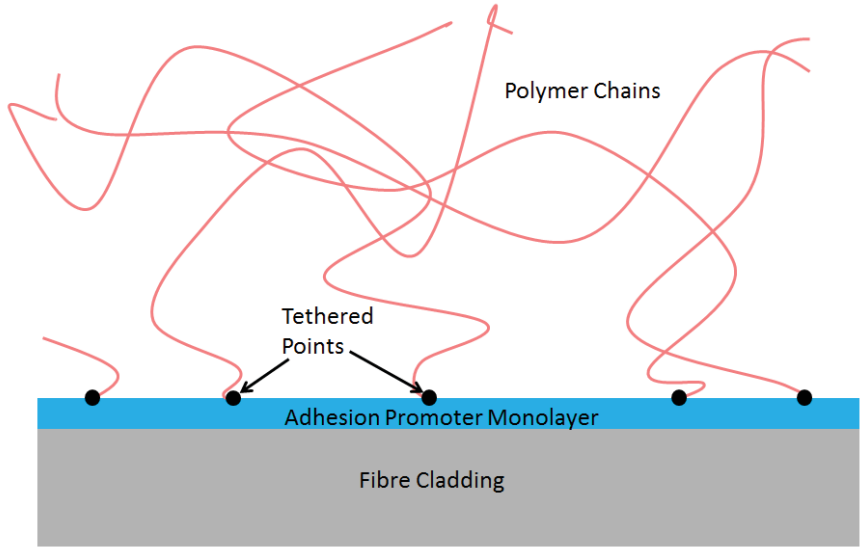


Figure 4.4 – The mono layer of adhesion promoter forms a covalent bond bridge from the glass optical fibre surface to the polymer chain - tethering the polymer coating to the fibre.

4.3.4 Dip coating

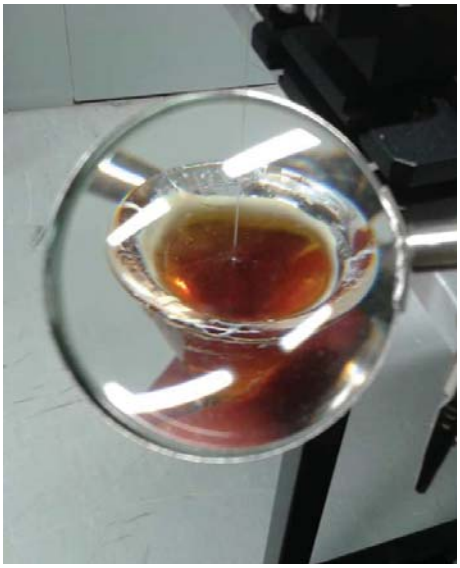
A dip coating set up was developed to allow the precise control of the fibre while it was being coated (Fig 4.5). The fibre was aligned vertically and secured to the stage with the solution bath raised so that the tip of the fibre was just submerged. The top of the solution bath funnels out to give a pool for the fibre to be dipped into. This was to prevent the fibre from sticking of the edges of the solution bath, resulting in an uneven coating.

The setup allowed up to 50 mm of the fibre to be coated, this is the maximum travel of the stage. The length of a commercial Bragg grating was 10 mm long and was arranged to be in the middle travel range to maximise coating evenness. The fibre was lowered into the solution at a speed of 1 mm/s and left for 30 seconds to settle, allowing for surface wetting, before being withdrawn at the desired speed. If the fibre was to be dipped multiple times a 5 minute drying time between dips was observed. All the speeds used an acceleration of 1.5 mm/s^2. The thicknesses of the coatings were measured using a computer linked microscope with distance measuring software.

Before a Bragg grating could be coated, an investigation of the solution viscosity and withdrawal speed was conducted on plain stripped optical fibre. As a general rule, higher solution viscosity and faster withdrawal speed lead to thicker coatings. These are the most important parameters for achieving uniform repeatable coatings. By increasing the weight percent (wt%) of the polymer in solution the viscosity increases. For many coatings the target thickness was 50 μm. The coating thickness does not effect the CME, allowing the comparison of coatings.



(a) Controlled motorised stage used for dip coating fibres.



(b) An action shot of the fibre coating and withdrawal from the solution bath.

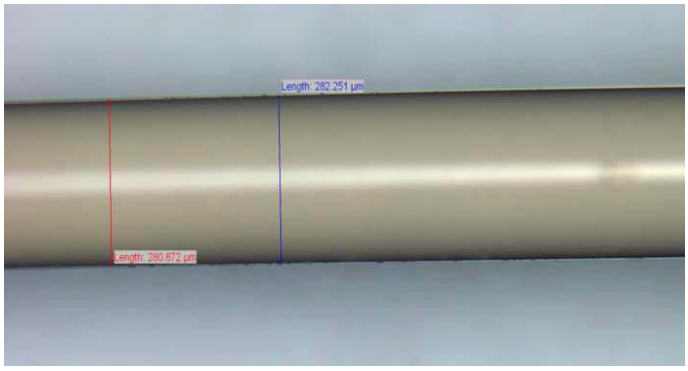
Figure 4.5 – Dip coating setup used to coat fibre Bragg gratings.

However, it does increase the size of the humidity response, thereby increasing the signal to noise ratio of the response being recorded. This target thickness should be small enough for a linear humidity response, without excessive coating unevenness, which will split the Bragg reflection peak.

The solutions were prepared freshly for each set of dip coating trials. The solvent will evaporate over time increasing the viscosity and forming a skin, requiring the top of the solution bath to be scooped and discarded between each fibre coating. For solutions with excessive skin formation it was beneficial to cover the bath with tinfoil, with a small hole for the fibre to go through. This left a solvent saturated atmosphere at the surface of the solution and greatly slowed the formation of a skin. Slightly thinner coatings were obtained when doing this.

If the withdrawal speed or solution viscosity was too high the coating would form beads rather than a smooth uniform coating (Fig 4.6). The onset of beading could be delayed by using hot air drying. This dried the coating before it could bead, allowing for thicker uniform coatings to be achieved. A heat gun with a laminar flow head set to 50 °C held 300 mm from the fibre was used for hot air drying. Although not used in this study, the addition of a surfactant to the solution lowers the surface tension and also delays the onset of beading.

In some cases it was not possible to get a uniform coating of desired thickness in a single dip, in these cases multiple dipping was used. On the second and subsequent dips when the coated fibre was immersed in the solution bath a small layer of the coating was dissolved. This should allow the second coating to have polymer entanglement with the previous, leading to a homogenous coating. Sub-



(a) A uniform coating.



(b) A beaded coating.

Figure 4.6 – Dip coated fibres.

sequent dipping also lead to much larger thicknesses being added for the same dipping conditions as the first coating. In practice a large amount of trial and error was used with the fibre dip coating conditions for the polymers investigated given in Table 4.1.

Table 4.1 – Dip coating conditions for the polymer coatings investigated.

Polymer[a]	Cladding Diameter (μm)	Solvent	wt%	Withdrawal Speed (mm/s)	Thickness (μm)
PMMA	125	1,1,2-TCE	17	2.4 & 1.5	50
MAA	125	1,1,2-TCE	32	2.4	51
EA	125	1,1,2-TCE	27	1 & 1.5	48
BA	125	1,1,2-TCE	30	2.4 & 2.4 & 1	65
PEI	125	1,1,2-TCE	25	0.2	48
PEI	125	1,1,2-TCE	22	0.3	141
Modified PEI	125	1,1,2-TCE	24	1 & 1	60
P84	125	NEP	25	0.3	23
P84	125	NEP	25	0.3 & 0.3	62
P84	125	NEP	25	0.7	79
P84	80	NEP	25	0.3 & 0.3	21
P84	54	NEP	25	0.5	19
P84 HT	125	DMF	30	1.6	53
PVOH-Et	125	1:1 water/propan-1-ol	20	1 & 0.5	110

[a]A list of acronyms can be found at the back of the thesis.

Achieving uniform coatings was vital, as even small unevenness can lead to substantial errors in the calculated CME. This and not breaking the fibre during stripping were the major challenges of this work.

Although not investigated in this thesis, the adhesion of a coating to the fibre can be enhanced by roughing the optical fibre [61]. This can be done be rolling the fibre in lapping fibre[§]. Enhanced adhesion allows for better transfer strain between the coating and optical fibre, improving response.

4.3.5 Spray coating

Spray coating was investigated as an alternative method to dip coating, and was done using an air brush (AMZ Hobby Air Brush AB101) linked with a compressed air line. This particular air brush was chosen as it had a small spray tip for precision coating and a glass canister below the air gun, avoiding problems with the solvent being in contact with plastic components. The fibre was held vertically and carefully rotated by hand to coat around the fibre, with the coating thickness controlled by the duration of spray coating. A solution of 11wt% PEI in 1,1,2-TCE was spray coated onto fibres achieving thicknesses of 44, 73 and 320 μm.

There was great difficulty in achieving uniform coatings while rotating by hand. An additional difficulty was the solution drying as it left the spray gun before hitting the fibre. This reduced the surface wetting of the solution to the fibre, and its subsequent adhesion.

4.3.6 Drying

After coating the fibre was left to dry in ambient conditions for one day before vacuum oven drying. The vacuum oven used was a Lab-line programmable temperature vacuum oven (Model 3618PDM) with a vacuum of 110 Torr slowly applied. The heating ramp consisted of 1 °C per minute ramp to 50 °C, held for 8 hours, then a ramp of 0.5 °C per minute to 80 °C, held for 8 hours. After this the oven was slowly cooled back to room temperature. The application of such slow vacuum and temperature changes was to avoid the effects of coating bubbling and cracking which occur from rapid pressure and temperature changes.

4.4 Experimental setup

This section comprises of two parts, where the first outlines the equipment and methodology used to measure the humidity response of the fibres for a constant temperature. The second outlines the equipment and methodology used to measure the temperature response of the fibres for a constant humidity. As both

[§]Good roughening of a fibre was achieved by rolling 20 times in 6 μm lapping paper.

strain and temperature have an effect on fibre Bragg grating sensors, any experiment must be designed with each effect in consideration. The fibres were housed in a strain free state, so that the only strain felt by the fibre was due to humidity changes.

4.4.1 Humidity response setup

The humidity response was measured using an insulated climatic chamber where temperature and humidity could be controlled. The position of the Bragg reflection peak of the fibre was recorded by an optical interrogator (OSA 150D), which is both a 1550 nm broadband light source and a detector[¶]. The interrogator was computer linked with a custom labview program that allowed the real time recording of the Bragg reflection peak.

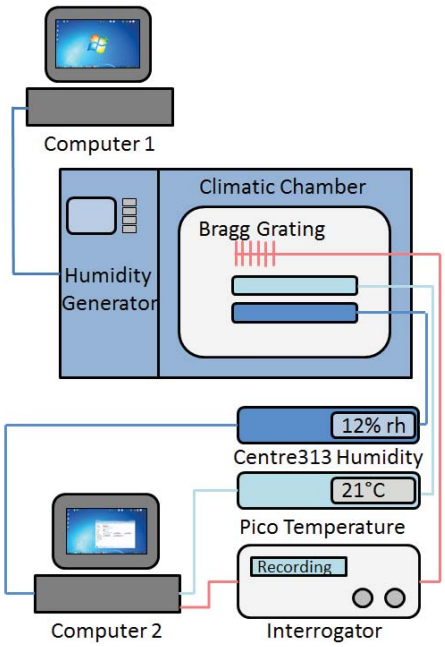
Humidity and temperature in the chamber was monitored with a Centre 313 humidity and temperature probe and Pico Technology PT-104 data logger temperature probe. Both probes were computer linked for data recording. The PT-104 temperature probe possessed a higher resolution than the temperature recorded by the Centre 313 probe, so was the preferred temperature probe.

The humidity and temperature of the chamber was controlled with a 2500 Thunder Scientific humidity generator. This generator was computer linked with programmable auto-profile software that allowed humidity and temperature step profiles to be automated. The generator itself had a set of relative humidity and temperature sensors inside the chamber, allowing another means of recording of humidity and temperature in the chamber (Fig 4.7).

The chamber was held at a constant temperature of 21 °C while performing an auto-profile cycle. This consisted of dry to humid steps of 12, 20, 30, 40, 50, 60, 70, 80, 90 and 95 %rh and the reverse humid to dry steps to return to the dry 12 %rh start. For the initial step from ambient conditions to the first dry step the chamber was left to equilibrate for two hours. Every other step change had a one hour holding period. If multiple cycles were investigated the second and subsequent cycles would commence immediately after the completion of the previous cycle.

When the 2500 Thunder Scientific humidity generator was unavailable a two-flow generator was used in its place. The 2500 Thunder Scientific humidity generator was the preferred choice as it had extremely stable temperature control and had auto-profile functionality. In some cases when using the two-flow humidity generator a small temperature drift would occur, requiring the data to be corrected for this drift using the temperature response of the fibre.

[¶]A detailed description of the OSA 150D was given in chapter 3.



(a) Schematic of humidity response setup.



(b) The actual setup during a humidity cycle.

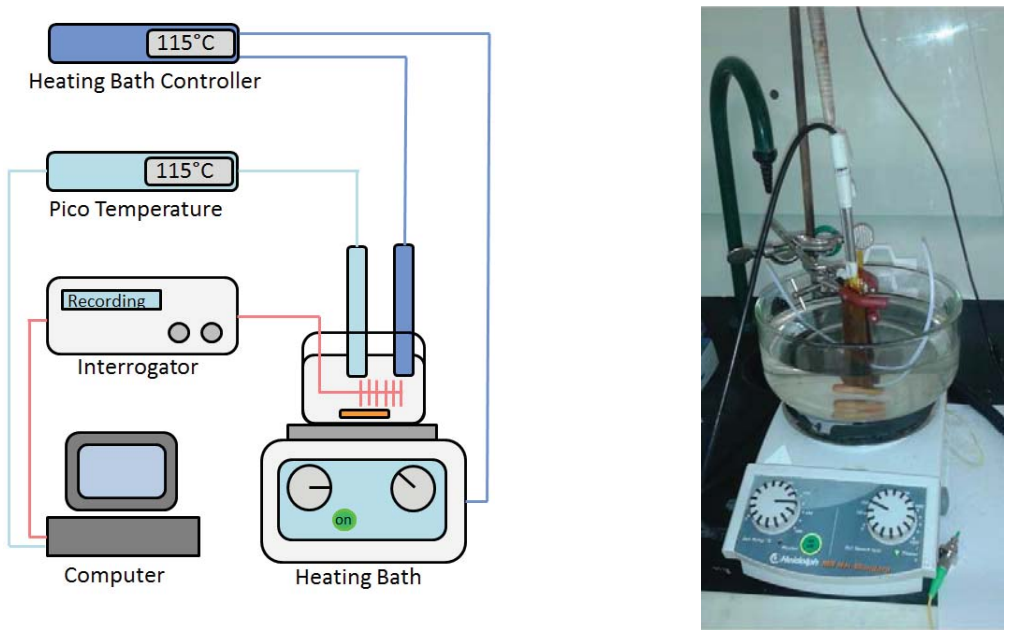
Figure 4.7 – Humidity calibration response setup.

4.4.2 Temperature response setup

The temperature response of the coated fibres was measured using a heated oil bath. Silicone oil (CAS: 63148-62-9) was the preferred oil as it had a high flash point of 300 °C and a sufficiently long molecular chain that water would not be held in it. The oil bath was heated using a Heidolph MR Hei Standard magnetic stirrer, with the temperature of the bath regulated by a probe in the oil connected to the heating control unit. The temperature in the bath was recorded using a pico technology PT-104 data logger temperature. The coated fibre was secured in bath** with the temperature probes adjacent to the Bragg grating section (Fig 4.8). A stir bar rotating slowly at 100 rpm was used to circulate the oil for even heating of the bath.

The oil bath was heated to 115 °C and held for 15 minutes while monitoring the Bragg reflection peak. The peak would slowly decrease, as moisture was expelled from the fibre, before reaching a stable dry humidity free value. The heating was then simply switched off, while leaving the stir bar on, allowing the bath to slowly cool back to room temperature over a matter of hours. This enabled a temperature calibration plot to be obtained.

**An optional thin plastic sleeve could be used to house any particularly delicate fibres.



(a) Schematic of temperature response setup.

(b) The actual setup during a temperature measurement.

Figure 4.8 – Temperature calibration response setup.

4.5 Poly(methyl methacrylate) fibre coatings

A series of four polymer coatings based on poly(methyl methacrylate) and modified block co-polymers were investigated. This was to obtain an insight into what structural modifications might improve the humidity response performance of a polymer coating. The polymers were sourced from Sigma Aldrich and used as provided, with the chemical structures of the polymers provided in Fig 4.9.

Extensive studies on the water uptake in PMMA have been done in the literature, they show that the mass fraction of water with relative humidity begins to deviate from linearity, by increasing more rapidly, after 75 %rh. This deviation from linearity is attributed to the formation of larger water clusters. Below 75 %rh water molecules only associate with the polymer functional groups as dimers. Recent studies have shown that water monomers do not form, even at low humidity, with the formation of water dimers being preferential. However, at higher humidity they associate and form higher sized water clusters as trimers or hexamers [65].

In Fig 4.10 the four PMMA based coated fibres were exposed to step wise increasing, ▲, then decreasing, ▼, humidity changes. Hysteresis was observed for all of the PMMA based polymers, where the decreasing humidity changes result in a larger Bragg wavelength shift than the corresponding increasing step for the same relative humidity. This is the result of the formation of water clusters inside

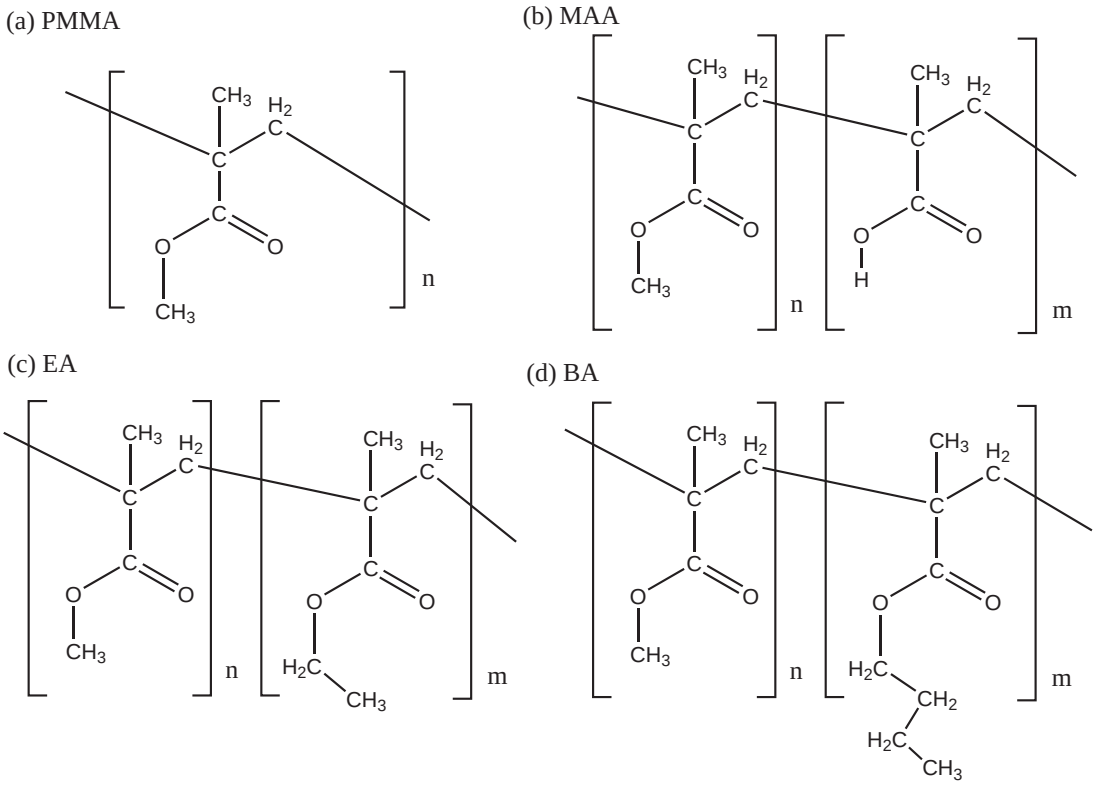


Figure 4.9 – Chemical structures of (a) poly(methyl methacrylate) (PMMA) MW 350k CAS: 9011-14-7, (b) poly(methyl methacrylate-co-methacrylic acid) (MAA) MW 34k CAS: 25086-15-1, (c) poly(methyl methacrylate-co-ethyl acrylate) (EA) MW 101k CAS: 901-88-2 and (d) poly(methyl methacrylate-co-butyl methacrylate) (BA) MW 75k CAS: 25608-33-7.

the polymer matrix. The formation of these clusters is an indication that the hygroscopy, its ability to attract and hold water molecules from its environment, of the polymer is high and relatively large voids exist in the polymer [66]. The effects of this type of hysteresis increases with the amount of water absorbed [67].

Hysteresis was only observed in the short term, after a sufficiently long time the polymer will return to the same state as increasing humidity state, ▲. The humidity response results for PMMA and its co-polymers also show a deviation from linearity at relative humidity above 75 %rh, this was due to the non-linear increase of mass fraction of water by the formation of higher sized water clusters.

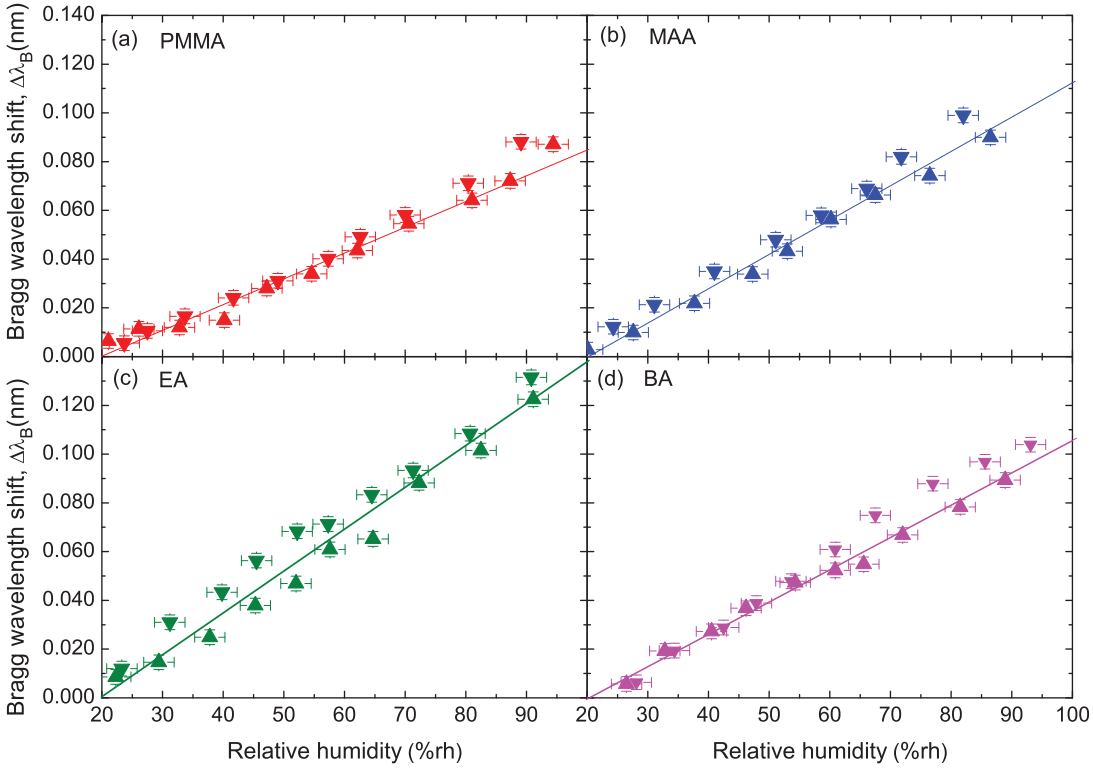


Figure 4.10 – Plots of Bragg wavelength shift for dry to humid, ▲, and humid to dry, ▼, humidity step changes for coatings of (a) poly(methyl methacrylate) (PMMA) of 50 μm thickness, (b) poly(methyl methacrylate-co-methacrylic acid) (MAA) of 51 μm thickness, (c) poly(methyl methacrylate-co-ethyl acrylate) (EA) of 48 μm thickness and (d) poly(methyl methacrylate-co-butyl methacrylate) (BA) of 65 μm thickness. The lines are just for guides.

The slopes of the humidity responses[††] can be used to calculate the coefficient of moisture expansion[‡‡] for each coating by using equation 4.7. The results of this calculation are provided in Table 4.2. The coefficient of moisture expansion

[††]Only the slope of the linear portion of the dry to humid, ▲, data was considered to remove any effects from hysteresis due to water cluster formation.

[‡‡]The CME is given in ppm which is short for parts per million ($1x10^{-6}$) and is not to be confused with pm which is short for picometre.

removes the dependence on thickness and allows a much better comparison of the performance of the coatings. The coefficient of moisture expansion varies significantly between PMMA and its co-polymers.

The CME increases significantly from basic PMMA to the MAA co-polymer, and was explained by the water dimers getting better access and association to the MAA carboxylic acid group. The EA co-polymer yielded the best result with a CME of 19.1 ppm/%rh. While dip coating it was noticed that EA co-polymer had an extremely good adhesion to glass. This increase in CME could be attributed to the better adhesion and consequent better strain transfer between the polymer and glass fibre. Later extension of the carbon chain with the BA co-polymer, led to a significant decrease in the CME. This decrease was attributed to the extended carbon chain either whipping around displacing the associated water dimer or forming a non-polar shield preventing the water dimer from associating (Fig 4.11).

Table 4.2 – Thickness, humidity response, coefficient of moisture expansion and sensitivity for PMMA and the PMMA co-polymers investigated.

Polymer	Thickness (μm)	Slope (pm/%rh)	CME (ppm/%rh)	S_{rh} (ppm/%rh)
PMMA	50	0.97	11.7	0.6
MAA	51	1.36	16.1	0.9
EA	48	1.51	19.1	1.0
BA	65	1.29	11.4	0.8

These results highlight important chemical structural features that influence a polymers' humidity response. By limiting chain lengths to reduce chain whipping or shielding and adding additional oxygen atoms to act as water associating sites, the humidity response could be enhanced.

4.6 Polyetherimide fibre coatings

The underlying chemical structure of polyetherimide (PEI) was selected for modification to improve its humidity response. It was selected because it had a poor humidity absorption, allowing for improvements, and most importantly was soluble in many solvents. This made it easier to coat onto fibres, avoiding the major solubility difficulties when using polyimides. First unmodified polyetherimide (Fig 4.12) had its humidity response investigated, then structural modifications were made and the response re-investigated.

The humidity response of polyetherimide depends on water dimers forming hydrogen bonds with the oxygen atoms in its polymer backbone, causing the polymer to swell. The effect of spray and dip coating were also investigated to determine their effect on the coatings humidity sensing performance.

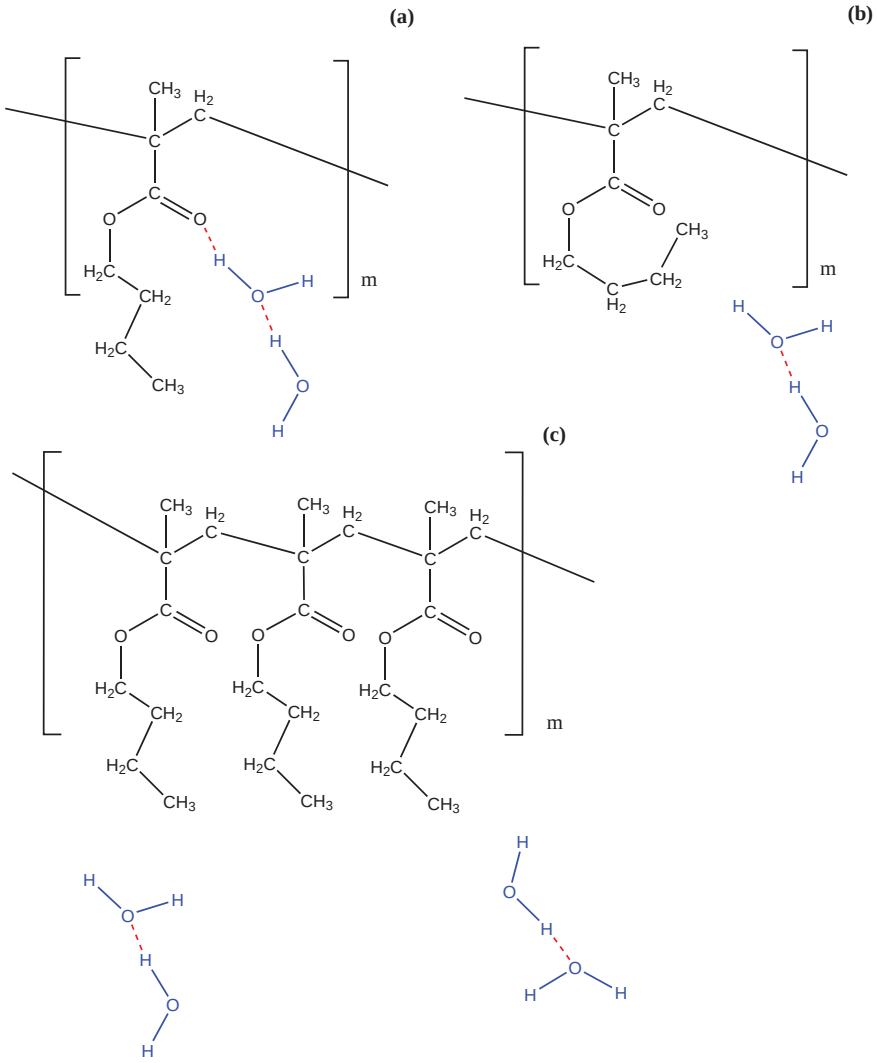


Figure 4.11 – Chemical structure of poly(methyl methacrylate-co-butyl methacrylate) (BA) in the configuration of (a) associating with a water dimer, (b) displacing a bonded water dimer by chain whipping and (c) preventing water dimers from associating by the formation of a chain shield.

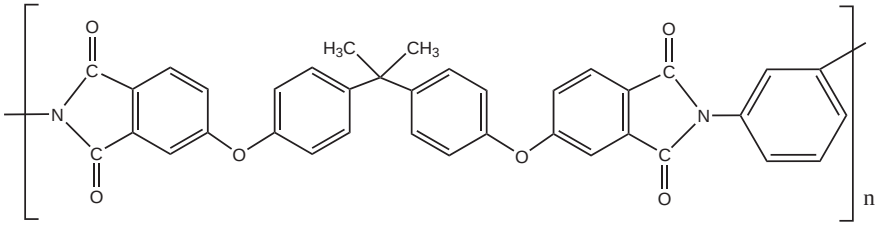


Figure 4.12 – Chemical structure of polyetherimide (CAS: 61128-46-9) sourced from Sigma Aldrich and used as provided.

4.6.1 Dip coated polyetherimide coatings

A 48 μm thick coating of polyetherimide was dip coated onto a fibre and exposed to step wise increasing, ▲, then decreasing, ▼, humidity changes (Fig 4.13a). The slope of the response was used to calculate the CME (Table 4.3) resulting in a CME of 5.6 ppm/%rh, which was half that of plain PMMA.

The response of PEI was enhanced by its higher Young's modulus (3.579 GPa) relative to PMMA (2.25 GPa), where a stiffer polymer transfers strain more effectively to the fibre [68].

However, this enhancement was more than offset by the great reduction in the number of oxygen atoms in polyetherimides' backbone relative to PMMA. Oxygen atoms allow more locations for water dimers to associate with, increasing the uptake of water and polymer swelling.

It was difficult to determine if hysteresis was present due to the very small humidity response of the coating, which resulted in error bars overlapping for the increasing and decreasing parts of the humidity cycle.

Table 4.3 – Thickness, humidity response, coefficient of moisture expansion and sensitivity for PEI and the modified PEI investigated.

Polymer	Coating method	Thickness (μm)	Slope (pm/%rh)	CME (ppm/%rh)	S_{rh} (ppm/%rh)
PEI	Dip	48	0.67	5.6	0.4
PEI	Spray	44	0.27	2.5	0.2
PEI	Spray	73	0.26	1.3	0.2
PEI	Spray	320	1.58	2.0	1.0
Mod PEI	Dip	60	1.45	9.2	0.9

4.6.2 Spray coated polyetherimide coatings

Spray coating was investigated as an alternative method to dip coating, to determine if the method of coating the fibre could influence the humidity performance. When using spray coating it was difficult to control coating thickness and uniformity, as illustrated in Fig 4.14. Coatings of 44, 73 and 320 μm thickness were spray coated and exposed step wise increasing and decreasing humidity (Fig 4.13b).

The slope of the coatings humidity response the CME were determined and given in Table 4.3. A comparison of spray and dip coating for coatings of similar thickness was given in Fig 4.13c.

The response of the spray coated fibre was half that of the dip coated. This was reflected in the CME, where the spray coated fibres were approximately

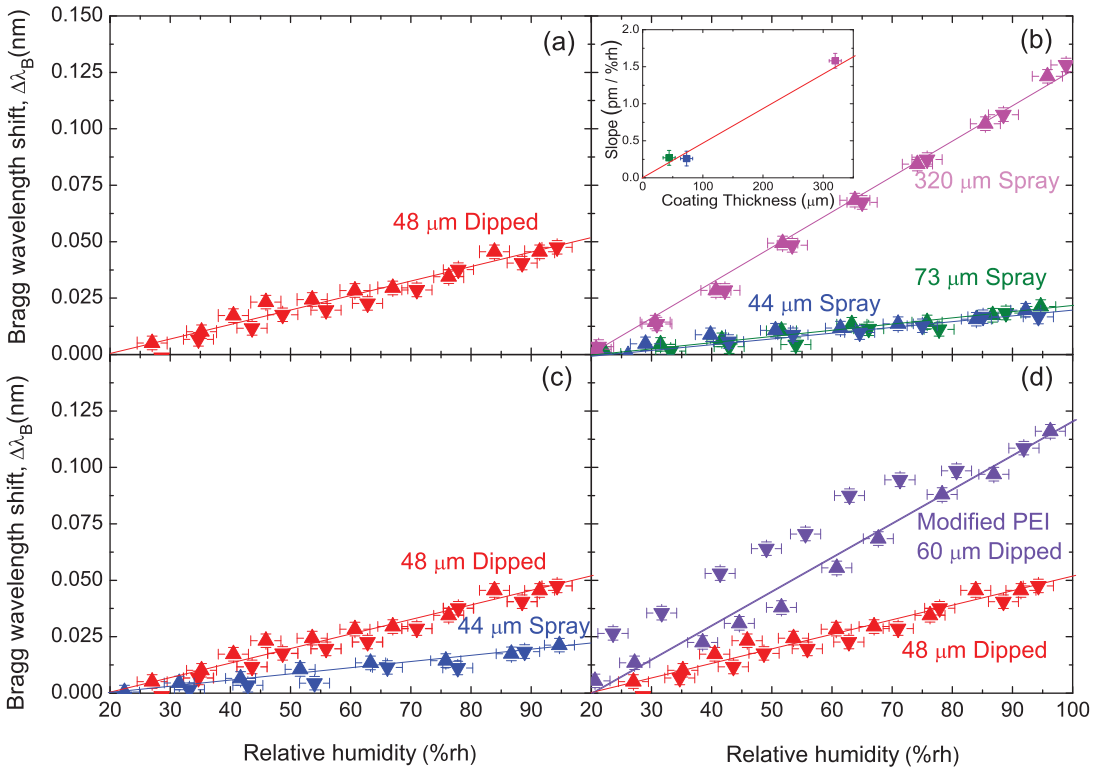


Figure 4.13 – Plots of Bragg wavelength shift for dry to humid, ▲, and humid to dry, ▼, humidity step changes for polyetherimide coatings that are (a) dip coated with 48 μm thickness, (b) spray coated with 44, 73 and 320 μm thickness - the inset is a plot of the humidity response slope against spray coated thickness, (c) dip coated with 48 μm thickness and spray coated 44 μm thickness and (d) dip coated with 48 μm thickness and a modified polyetherimide coating that is dip coated with 60 μm thickness. The lines are just for guides.

2.0 ppm/%rh and the dip coated fibre was 5.6 ppm/%rh. The coating was the same material and should have the same CME. The significant decrease in CME was attributed to the solvent drying during spray coating, greatly reducing the surface wetting and adhesion of the coating to the fibre.

The humidity response with spray coated thickness was illustrated in the inset of Fig 4.13b. Here the humidity response increases linearly with coating thickness. However, more than three data points are required for more certainty of the linearity.

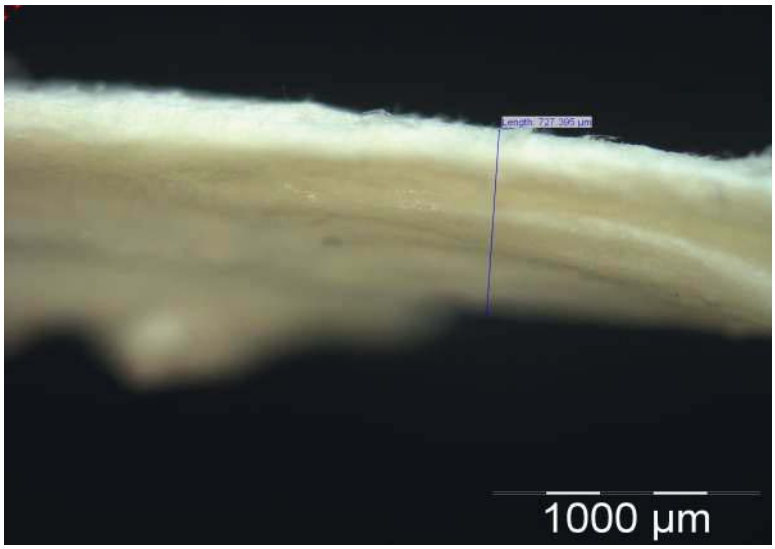


Figure 4.14 – Polyetherimide spray coated on to a fibre Bragg grating. Thickness and uniformity of the coating is difficult to control using spray coating.

4.6.3 Modified polyetherimide coatings

Polyetherimide was modified (Mod PEI) to enhance humidity response performance (Fig 4.15). This was synthesised with a co-polymer block alongside the usual polyetherimide homo-polymer block. The modifications include:

- A carboxylic acid (COOH) group being added - this was another site for water dimers to associate with unhindered access around the group.

- A hydrophobic part of PEI was replaced - the hydrocarbon ether linkers in unmodified PEI are hydrophobic (no place for water to associate), this was altered to have a hydrophilic (a place for water to associate) group attached to this portion.

- The COOH group was linked by only 2 carbons - this prevented chain whipping from occurring.

- The modified section had less aromatic groups - benzene rings can undergo tight pi-stacking (Fig 4.16), reducing the voids in the polymer for water to

fill. By reducing the aromatic groups and introducing more flexibility more voids were created.

• The COOH group was located on a side chain protruding away from the polymer back bone, with reduced aromatic groups in its neighbourhood - this positions the COOH group near a void, allowing good access to water held in the polymer.

A 60 μm coating was dip coated, as it had better surface wetting and coating control than spray coating. The humidity response of the modified coating was investigated (Fig 4.13) with the CME reported in Table 4.3. A increase in CME from 5.6 ppm/%rh for the unmodified PEI to 9.2 ppm/%rh for the modified PEI was observed. The larger response allowed hysteresis to be observed. Here the humid to dry, ▼, step changes resulted in a larger shift than the same relative humidity for the initial increasing humidity steps, ▲. This was attributed to the water held in the voids not being released easily.

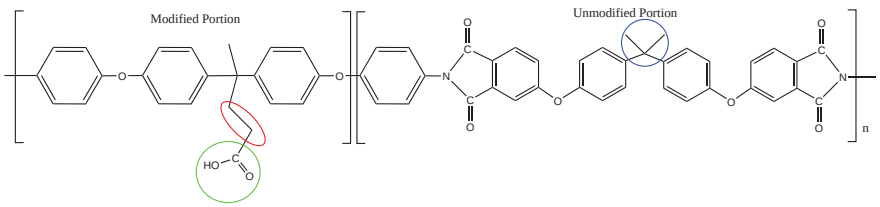


Figure 4.15 – Chemical structure of the modified polyetherimide synthesised, an additional carboxylic acid group linked by only two carbons replaces the hydrophobic part of unmodified PEI.

This shows that structural modifications have the potential to enhance the humidity response of a polymer coating. The next step is to investigate polyimide coatings, which perform extremely well as humidity responsive coatings [11, 55, 57, 58, 69–71] and consider the modifications to improve their response further.

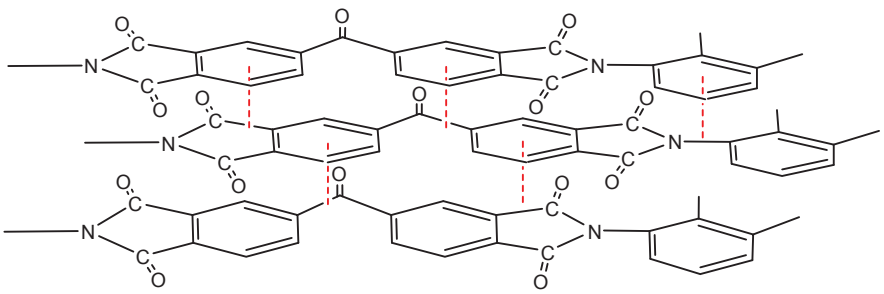


Figure 4.16 – The polyimide P84 undergoing tight sandwich pi-stacking. Any polymer with distributed aromatic rings has the potential to undergo pi-stacking.

4.7 Polyimide fibre coatings

With many types of polyimide available it is important to trial a series of polyimides to determine the best polyimide to modify. Coatings of P84 a best selling polyimide, P84 HT a particularly water absorbing polyimide (Fig 4.17) and default pre-coated polyimide FBG coating from Avensys, were chosen as starting polymers to investigate. A study of the effect of coating thickness and fibre cladding diameter was performed. A mechanism for the attachment of the adhesion promoter (3-APTS) to the polyimide coatings was also proposed.

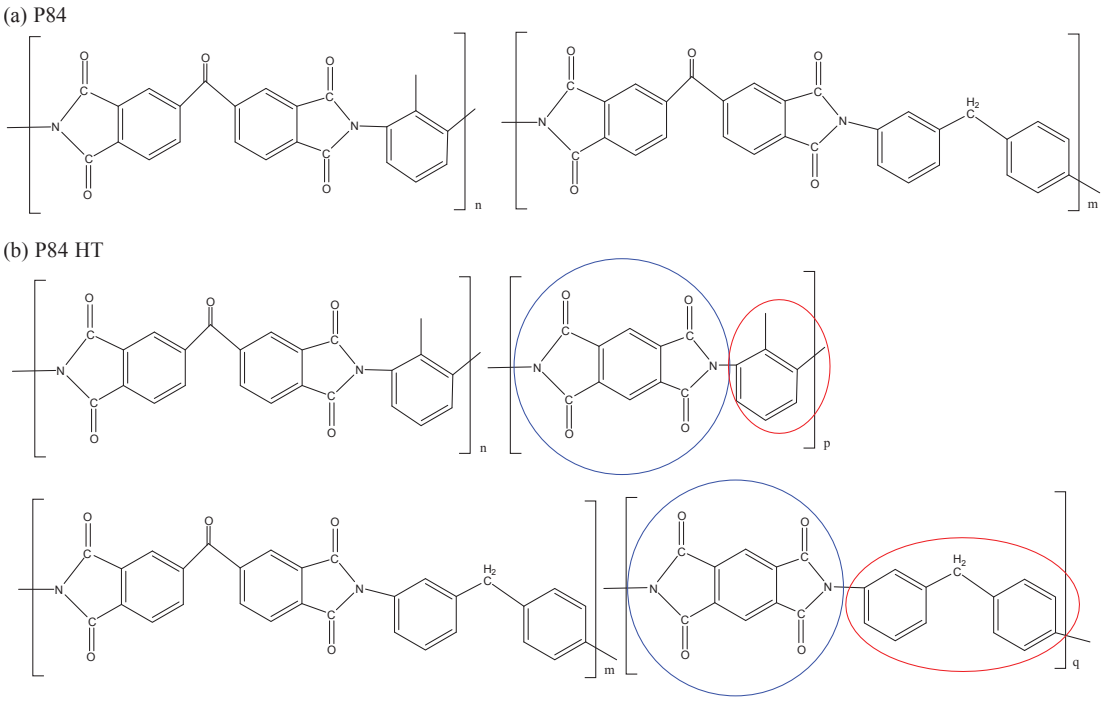


Figure 4.17 – Chemical structure of (a) P84 and (b) P84 HT. The P84 HT structure has additional blocks added to the base P84 structure (the p and q repeating blocks) which have a hydrophilic part and a solubility part. The ratios of the blocks in the polymer are not known.

4.7.1 Avensys polyimide

The default polyimide coating on a fibre Bragg grating from Avensys was investigated for its humidity response. The supplier was unable to provide a chemical structure of the polyimide (the colour of the coating suggests it is not P84 or P84 HT), but could confirm that an adhesion promoter was not used when coating the fibre. The humidity response and CME of the fibre was presented in Fig 4.18 and Table 4.4, where the CME of 54.3 ppm/%rh was a significant improvement over PMMA and PEI based coatings.

Table 4.4 – Thickness, humidity response, coefficient of moisture expansion and sensitivity for the polyimide coatings investigated.

Polymer	Cladding Diameter (μm)	Thickness (μm)	Slope (pm/%rh)	CME (ppm/%rh)	S_{rh} (ppm/%rh)
Avensys PI	125	18	1.50	54.3	0.97
P84	125	79	7.35	47.5	4.76
P84	125	62	5.29	45.9	3.44
P84	125	23	1.82	50.0	1.18
P84	80	20	2.23	43.1	1.44
P84	54	19	3.17	41.2	2.05
P84 HT	125	53	7.20	73.8	4.57

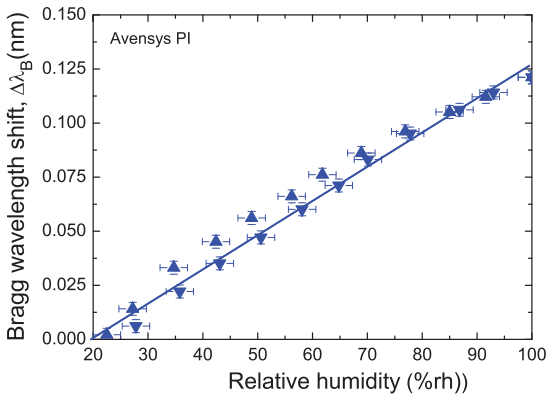


Figure 4.18 – Plot of Bragg wavelength shift for dry to humid, ▲, and humid to dry, ▼, humidity step changes for an Avensys FBGs default polyimide coating of 18 μm thickness.

4.7.2 P84 polyimide

P84 was selected for an investigation into the effect of coating thickness and fibre cladding diameter. It was selected because it was provided as a solution from the supplier, and yielded extremely uniform and repeatable coatings during dip coating. This minimised errors stemming from coating unevenness and allowed the effects to be more accurately compared.

The CME of P84 was determined to be 45 ± 5 ppm/%rh (Table 4.4). This was a slightly lower result than observed for Avensys PI, but it was still a significant improvement over PMMA and PEI based polymers.

Effect of coating thickness

The effect of coating thickness was investigated by coating a series of different thickness coatings onto fibres of the same cladding diameter. A set of 125 μm diameter glass fibres had coatings of 23, 62 and 79 μm applied and were exposed to stepwise humidity changes (Fig 4.19).

All of the coatings had a linear humidity response, with the slope of the response observed to increase with coating thickness. This observation was consistent with other polyimide coatings studied in the literature [55, 65, 69]. This lead to a linear sensitivity (S_{rh}) with coating thickness, similar to the results of spray coated PEI thickness study (Fig 4.13).

The CME of the P84 coatings were similar (Table 4.4). This was expected as the CME is specific to P84 and should be the same for each coating. However, in reality, differences due to adhesion, coating unevenness and errors when measuring coating thickness will lead to different CME values.

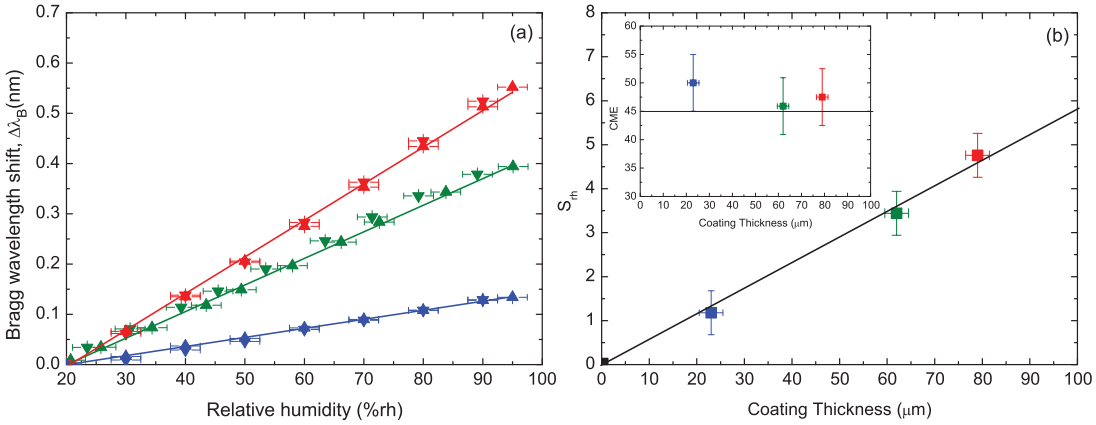


Figure 4.19 – Plots of Bragg wavelength shift for dry to humid, ▲, and humid to dry, ▼, humidity step changes for (a) P84 polyimide coatings of 23, 62 and 79 μm thickness and (b) the sensitivity and CME (inset) of the sensors with coating thickness. The lines are just for guides.

Effect of cladding thickness

The effect of cladding thickness was investigated by coating the same thickness coatings onto fibres with different cladding diameters. Stripped 125 μm diameter glass fibres were etched to 54 and 80 μm. Etching was performed with a solution of boiling (140 °C) 35wt% potassium hydroxide (KOH) in deionised water, with an etch rate of about 0.1 μm/hour.

A set of 54, 80 and 125 μm diameter glass fibres had coatings of 19, 20 and 18 μm applied respectively and were exposed to stepwise humidity changes (Fig 4.20).

All the fibres humidity exhibited a linear humidity response, where response was increased with smaller cladding diameter. This observation was consistent with other studies of polyimide coatings on etched fibres performed in the literature [57]. The increase in sensitivity was attributed to the increased ratio of coating to fibre cross sectional area, when using a smaller fibre cladding (equation 4.9).

The sensitivity of the sensor increases markedly with cladding at small cladding thickness. It is possible to etch a fibre so close to its core that the light propagated in the core can be influenced by its surroundings (evanescent wave sensing) [5]. However, with a 54 μm cladding and 9 μm core diameter the sensor was still well above the threshold thickness required for this effect to occur. There is a trade off between etching to increase response and retaining cladding thickness to prevent fibre fragility[§§].

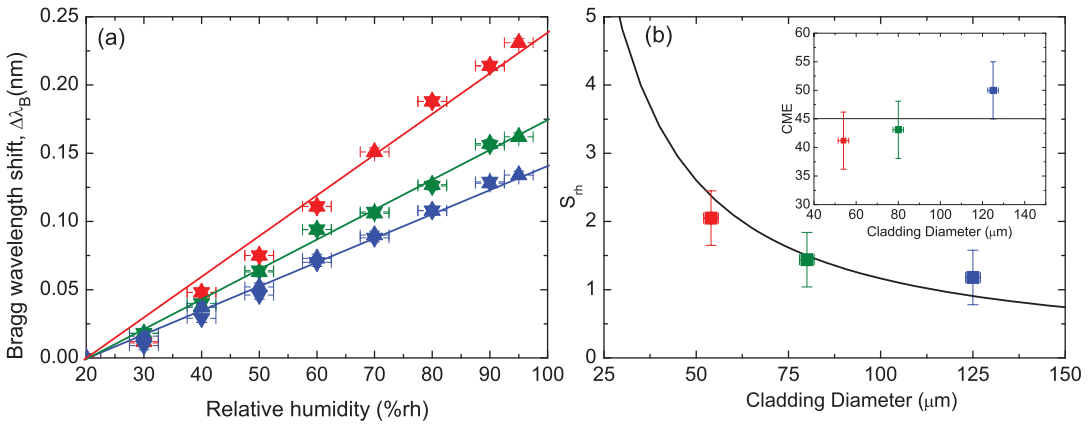


Figure 4.20 – Plots of (a) Bragg wavelength shift with humidity for fibres with cladding diameters of 54, 80 and 125 μm with the same thickness P84 polyimide coatings and (b) the sensitivity and CME (inset) of the sensors with cladding diameter. The line shows the calculated sensitivity with cladding diameter for a fibre with a CME of 45 ppm/%rh.

[§§]Many etched fibres met their end by breaking during handling.

4.7.3 P84 HT polyimide

For many (non-humidity sensing) applications water absorption is a problem, for example when polyimide is used as a circuit board. Because of this manufacturers focus on developing polyimides that have limited water uptake. This increases the potential of an enhanced humidity response from structural modifications to commercial polyimides. P84 HT was a high temperature polyimide that was particularly water absorbing. This polyimide has a wide range of uses due to its heat and chemical resistivity.

A 53 μm coating was applied to a 125 μm diameter fibre and exposed to humidity steps (Fig 4.21). The CME of 73.8 ppm/%rh (Table 4.4) was considerably higher when compared to other polyimides.

This was a significant increase from P84 (45 ppm/%rh), and was the most responsive coating investigated in this study. It gave a comparable response to other high performing polyimide coatings currently in the literature, such as HD microsystems Pyralin PI 2525 with a CME of 92 ppm/%rh [55].

The reasons for this significant increase in response can be explored by considering the chemical structure of P84 and P84 HT. P84 HT had the same backbone as the base P84, the exception being two additional repeating units added (Fig 4.17). The added units had a hydrophilic part (an imide of pyromellitic dianhydride) and a portion added for solubility. The increase of the CME for P84 HT can be attributed to the characteristics of the hydrophilic part which had:

- Four oxygen and two nitrogen atoms, which acted as water associating sites that were tightly packed around a central aromatic ring - resulting in a high water associating sites to aromatic ring ratio.
- Good water access to oxygen atoms - although not as good as a protruding side chain, it was more rigid and less likely to dissociate water.
- Reduced aromatic rings - this reduced pi-stacking with more voids for water to fill. The water associating sites were strategically located near these voids.

The exact ratio of each repeating unit was unable to be obtained (a possible trade secret) and as a result no comment can be made about its potential effect on the polymer. The results suggest that a high number of water associating sites to aromatic ring ratio has the potential to increase a polymers CME.

The long term performance of the P84 HT coated fibre was investigated with a set of 5 humidity cycles, followed by another set of 5 cycles one month later (Fig 4.22). The sets of cycles show a drift to shorter Bragg reflection peak wavelength as the cycles progress. The shift was particularly felt for lower relative humidity and the first cycle. The drift becomes less pronounced as the cycles progressed, finally resulting in reproducible values. Possible causes for this drift were:

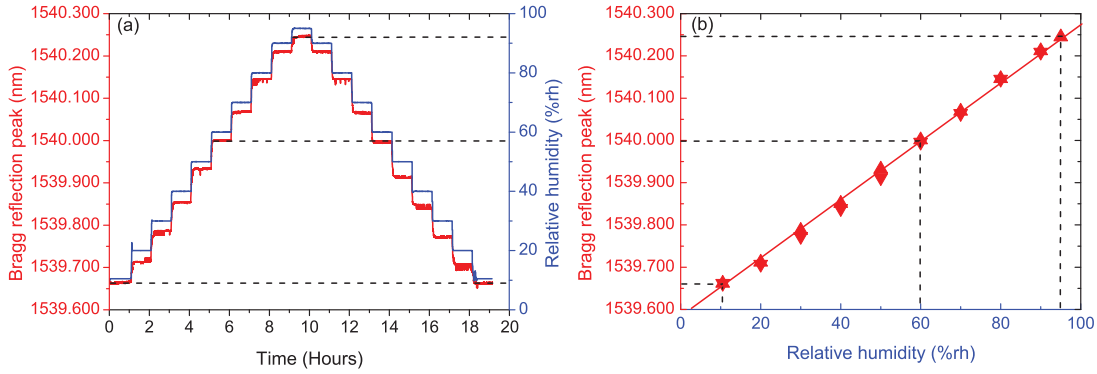


Figure 4.21 – Plots of (a) Bragg peak and humidity during a 19 hour humidity cycle and (b) Bragg peak stable values for the dry to humid (first 10 hours of the cycle), ▲, and humid to dry (last 9 hours of the cycle), ▼, humidity step changes for a P84 HT polyimide coating of 53 μm thickness. The lines are just for guides.

- The coating was under stress after coating due to solvent evaporation - the humidity (strain) cycles then release this stress allowing the coating to settle.

- Left over solvent from dip coating the fibre was occupying water associating sites. This was expelled when water fills the sites at high relative humidity. When subsequent cycles return to dry relative humidity the coating contracts further due to the absence of solvent.

- Initial voids in the polymer were being filled by polymer chains unraveling into them during the humidity (strain) cycles. This removes the void for subsequent cycles, preventing water from filling it.

The strongest explanation was the left over solvent from dip coating the fibre occupying the water associating sites. Strong polar aprotic solvents, NEP (CAS: 2687-91-4) and DMF (CAS: 68-12-2) with high boiling points 212 and 152 °C respectively, were required to dissolve polyimides, and left over solvent would likely be tightly held in the polymer associating sites.

The coatings were conservatively dried in a vacuum oven at 80 °C to prevent the coating cracking during drying, or the glue in the FC/APC fibre boot melting (around 100 °C). Glue melting would result in the fibre not being able to be coupled to the interrogator.

The Bragg gratings inscribed in the fibre core are resistant to high temperature, and will only be erased above 200 °C. Possible solutions to reduce or eliminate drift could be drying the coated Bragg grating portion (not the connector boot) at higher temperatures (180 °C)[¶¶]. Another solution could be a quick set of extreme humidity cycles, that would displace associated solvent and settle the

[¶¶]A hot plate could be used for this, as a vacuum oven requires a tight seal with the boot in the oven.

coating to reproducible values***. A small amount of drift is observed during the cycles conducted one month later. This is attributed to the sensor being stored in a laboratory and absorbing volatile organic compounds from the atmosphere. The drift could be eliminated by more rigorous storage, such as sealed vacuum storage.

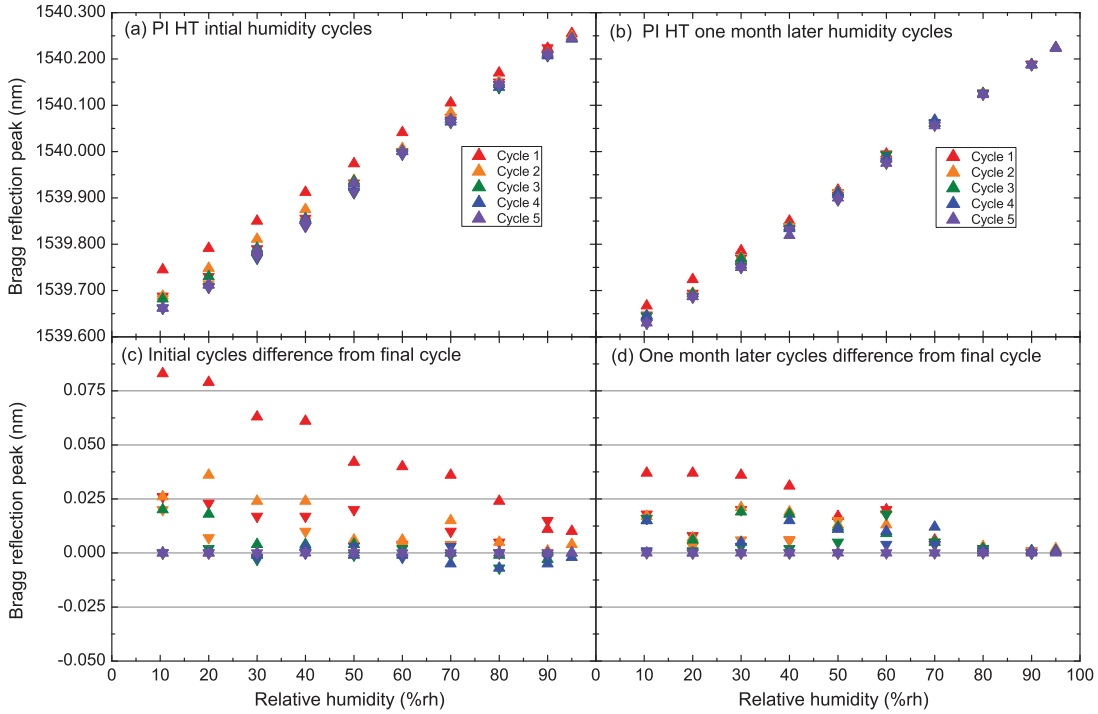


Figure 4.22 – Plots of Bragg peak and humidity for a 53 μm thick coating of P84 HT coated fibre with (a) an initial set of 5 humidity cycles and (b) another set of 5 humidity cycles done one month later. The differences between the cycles and the final cycle for each set are given in (a) and (b).

4.7.4 Adhesion promoter mechanism

A mechanism for the attachment of the adhesion promoter (3-APTS) to the polyimide was proposed. Here 3-APTS first polymerises with itself and attaches to the optical fibre forming a monolayer, via the mechanism outlined in reference [63].

The polyimide can undergo a ring opening with a free hydroxide ion (OH^-)††† [72], then react with 3-APTS via the mechanism proposed in Fig 4.23.

The 3-APTS could undergo a similar ring opening reaction with polyetherimide, but a different reaction with PMMA based polymers, where it would only react with the unpolymerised functional groups at the ends of the polymer.

***Sets extreme humidity cycles could be performed by the two-flow generator before a calibration cycle with the 2500 Thunder Scientific humidity generator.

†††The free hydroxide ion generated by the presence of water, where it is naturally occurring in an equilibrium with water.

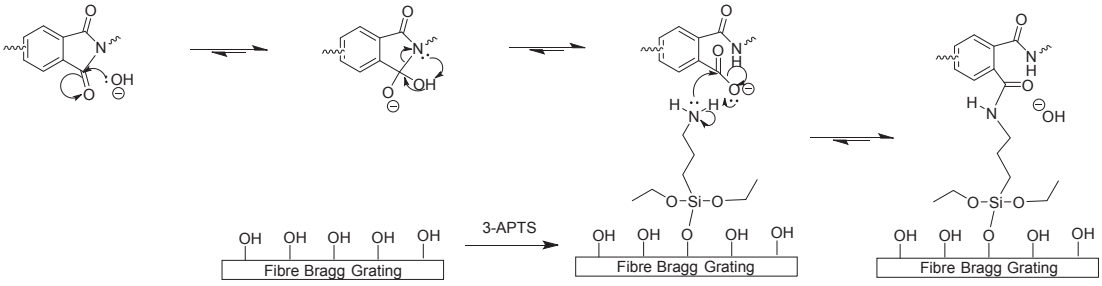


Figure 4.23 – A proposed mechanism of the adhesion promoter attaching to polyimide via a ring opening.

4.8 Other fibre coatings

In addition to the main investigation of PMMA, polyetherimide and polyimide based coatings, other coatings comprising of ormocer, polyvinyl alcohol-co-ethylene and acrylate were trialled for their humidity response.

4.8.1 Ormocer

Ormocer was an organically modified ceramic that had inorganic oxidic structures that were cross-linked or substituted by organic groups. This provided the coating extra sensitivity when used as a strain sensor, making ormocer a popular coating for fibre Bragg grating strain sensors [73].

An ormocer coated FBG was sourced from Draw Tower Gratings and used as provided. This fibre had a 125 μm cladding with a 33 μm ormocer coating and was exposed to a humidity cycle (Fig 4.24a). The fibre had a response slope of 2.1 pm/%rh, resulting in a CME of 44 ppm/%rh and sensitivity of 1.36 ppm/%rh.

The CME performance was approximately the same as a poorly performing polyimide coating. This coating was optimised for strain. It had a high Young's modulus (2.1 GPa [74]) and extremely good adhesion to the fibre from UV curing when the coating was applied.

This excellent strain transfer could help improve the CME of the coating [68]. However, the lower CME was unsurprising as the fibre is marketed as strain sensor, where changes in humidity would be a problem during strain measurements. This would make this fibre preferable to polyimide coated fibres for strain sensing applications. In practice FBG strain sensors are mounted to the structure they are measuring, where waterproof sealants could be used to remove the influence of humidity [73].

4.8.2 Polyvinyl alcohol-co-ethylene vinyl alcohol

Polyvinyl alcohol (PVOH) is highly moisture absorbing, able to absorb 10wt% of water at saturated relative humidity [75] and has a fast response time to humidity

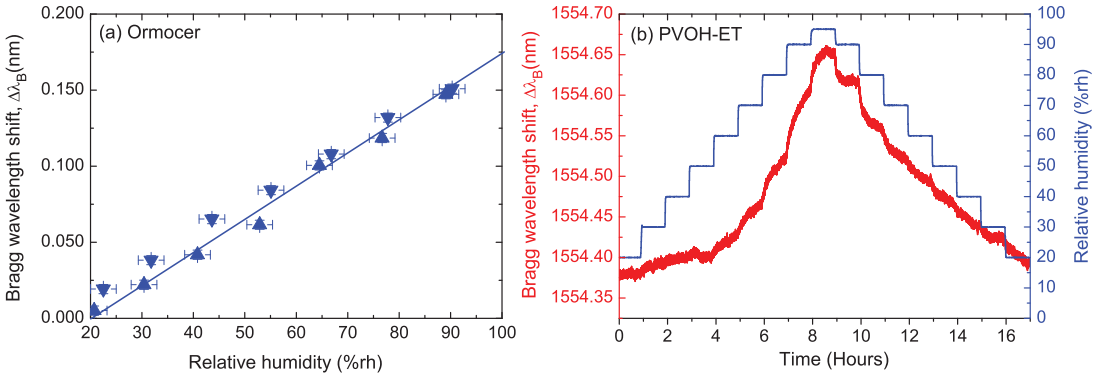


Figure 4.24 – Plots of Bragg wavelength shift with humidity for an (a) ormocer and (b) PVOH-ET coated fibre. The PVOH-ET fibre has an exceptionally slow response making it unsuitable for real time humidity measurements. The line is just a guide.

changes [76]. However, it breaks down with water over time, making it a good biodegradable material for fishing reel and plastic bags, but not good for a long-term moisture sensitive fibre coating.

Ethylene vinyl alcohol (EVOH) is widely used in food packages due to its low permeability to oxygen. It is capable of absorbing more than 10wt% of moisture at saturated relative humidity [77] and is not soluble in water.

The co-polymer polyvinyl alcohol-co-ethylene vinyl alcohol (PVOH-ET) has been shown to be stable in water for temperatures up to 80 °C [78]. This could be a good compromise between the large water uptake and fast time response provided by PVOH and the resistance to water solubility provided by EVOH.

PVOH-ET (PVOH 73 mol% and EVOH 27 mol%) (CAS: 25067-34-9) was sourced from Sigma Aldrich and used as provided. A 110 μm coating was dip coated on to a fibre and exposed to a humidity cycle (Fig 4.24b). The response of the coating was incredibly slow, with the chamber changing relative humidity step well before the coating had equilibrated. This meant the coating could not be used as a real time humidity sensor. The coatings response was skewed to the right, revealing it had a faster water desorption than absorption.

The slow response of the coating could be due to the low permeability of the ethylene vinyl alcohol part of the polymer and was exacerbated by the coating being thicker. The Bragg peak shifts a low 300 pm for the 20 to 95 %rh change. This was a poor response for a 110 μm thick coating, where PMMA based polymers outperformed this result. Although it was hoped to have the best properties of plain PVOH and EVOH, in reality the PVOH-ET co-polymer caused a small Bragg peak shift with an exceptionally slow response time. But at least it did not degrade with water.

4.8.3 Acrylate

An acrylate coated fibre was sourced from Draw Tower Gratings and used as provided. The fibre had an 125 μm cladding with a 36 μm acrylate coating and was exposed to a humidity cycle (Fig 4.25a).

No measurable response to humidity was observed. This was consistent with other studies on acrylate coatings [79]. A possible small response might be realised if the fibre was left for a very long time after a dramatic humidity step.

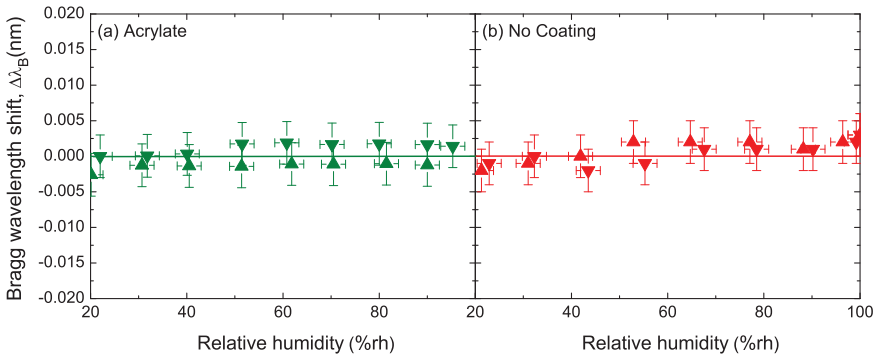


Figure 4.25 – Plots of Bragg wavelength shift with humidity for (a) an acrylate coating and (b) a bare 125 μm diameter fibre with no coating.

4.8.4 No coating

A stripped 125 μm diameter glass fibre with no coating was investigated for its humidity response and exposed to a humidity cycle (Fig 4.25b). No response to humidity was observed, consistent with water not penetrating the glass, resulting in no effect on the Bragg reflection peak.

4.9 Temperature response of coatings

The humidity free temperature response of the fibres were measured using an heated oil bath (Fig 4.26 and Table 4.5).

The most temperature responsive coating was the EA coating, with a response of 17 pm/°C observed. This was attributed to the strong adhesion the polymer has to the glass fibre. Ormocer gave a low temperature response of 12.6 pm/°C. However, this coating was optimised for strain measurements where temperature fluctuations are a problem. Another coating, ormocer-T, is marketed as a coating optimised for temperature measurements.

The uncoated bare fibre yielded the lowest response of 10 pm/°C. This suggests that having a polymer coating, regardless of what it is, can enhance the

temperature sensitivity.

The spray coated PEI coating gave a low response of 11.8 pm/°C, regardless of the thicker 73 μm coating. This could be a result of the poor adhesion that occurs when spray coating.

The acrylate coating possessed a low response of 11.1 pm/°C. This response could potentially be improved if a thicker coating was applied.

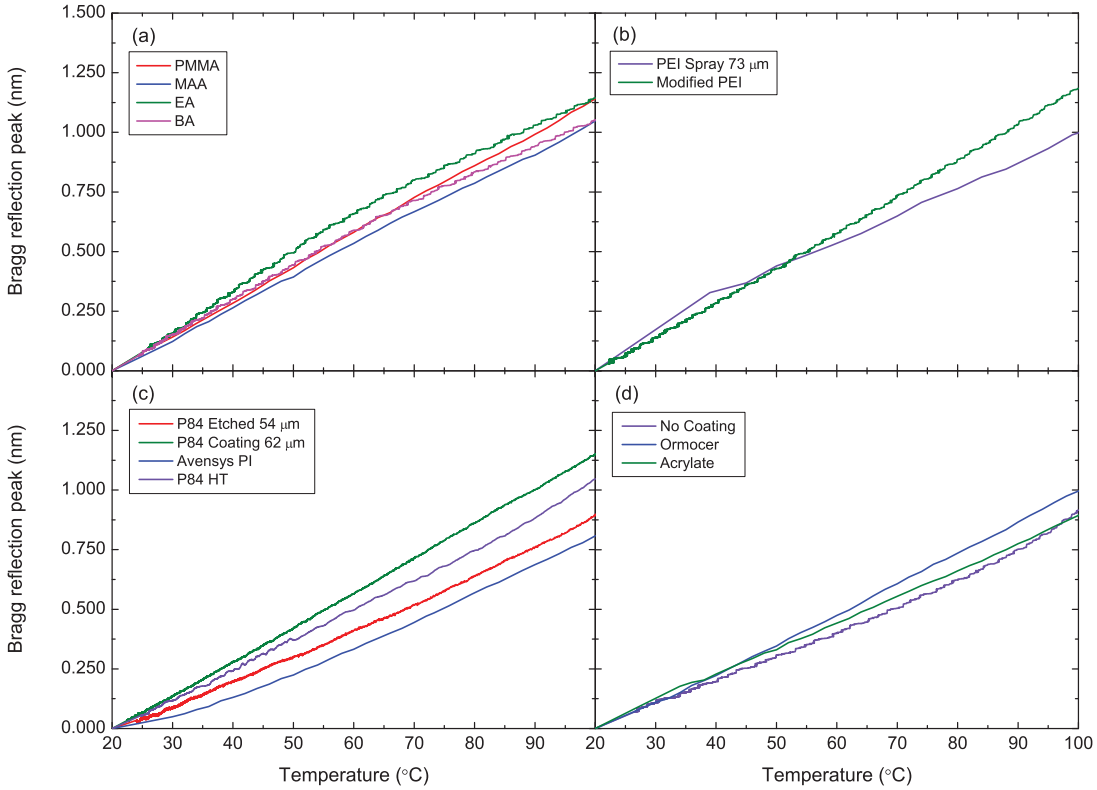


Figure 4.26 – The temperature response for (a) poly(methylmethacrylate) species, (b) polyetherimide species, (c) polyimide species and (d) other coatings investigated.

4.10 Summary and future work

In summary, a range of polyetherimide, poly(methylmethacrylate), polyimide and default factory coatings on retailed fibres were investigated for their humidity response. The study of these coatings lead to the development of a modified polyetherimide.

The investigation of PMMA and its co-polymers revealed that long carbon chain lengths decrease the coating humidity response, potentially due to chain whipping or shielding occurring. Structural modifications to polyetherimide enhanced its humidity response. The modifications involved adding more water

Table 4.5 – Humidity free temperature response of the coated FBGs investigated.

Polymer	Coating method	Cladding Diameter (μm)	Thickness (μm)	Slope (pm/°C)	S_T (ppm/°C)
PMMA	Dip	125	50	14.3	9.2
MAA	Dip	125	51	13.1	8.5
EA	Dip	125	48	17.0	11.0
BA	Dip	125	65	14.7	9.5
PEI	Spray	125	73	11.8	7.6
Mod PEI	Dip	125	60	14.7	9.5
P84	Dip	54	19	11.4	7.4
P84	Dip	125	62	14.4	9.3
Avensys PI	-	125	18	10.8	7.0
P84 HT	Dip	125	53	12.8	8.3
No Coating	-	125	0	10.0	6.5
Ormocer	-	125	33	12.6	8.1
Acrylate	-	125	36	11.1	7.2

associating sites and limiting carbon chain lengths, while using dip coating instead of spray coating. Polyimide based coatings were the most humidity responsive coatings, with P84 HT performing the best with a CME of 73.8 ppm/%rh achieved. This high response was attributed to the polymer having a high number of water associating sites to aromatic ring ratio.

A mechanism of the attachment of the adhesion promoter 3-APTS to polyimide was also proposed. After the initial coating of a fibre the Bragg reflection peak was observed to drift to lower wavelength, before yielding a reproducible response. This was attributed to residual solvent from coating being expelled.

The humidity sensitivity of a coating was able to be enhanced by either increasing the coating thickness or etching the fibre cladding. The temperature response of the coated fibre was investigated. The EA coating performed the best with a response 17.0 pm/°C achieved, where this high response was attributed to the very strong adhesion of the EA to its glass fibre.

Future work has two exciting directions it could go. Firstly, the humidity response of the coating could be further enhanced with variations based on P84 HT synthesised and its humidity response investigated. A good start would be to try to further increase the number of water associating sites to aromatic ring ratio. Solubility of the polyimide will be the greatest challenge to overcome, and trialling different solubility parts will be just as important as enhancing the hydrophilic parts of the polyimide[‡‡‡]. This fibre Bragg grating moisture sensor would have potential applications in fuel cells [80, 81], high temperature furnaces

[‡‡‡]Although numerous attempts were made to synthesise a modified polyimide, none of these was soluble to allow dip coating onto a fibre. As such they could not be reported in this thesis.

[82, 83], cold storage [84–86] and power transformers [87].

The second, and perhaps even more exciting direction, is to change the coating from sensing water vapour to sensing another vapour or gas. This could be done by changing the functionality of the coating, or by applying membranes over the coating to provide selectivity to certain vapours or gases. Here the greatest challenge will be resolving cross sensitivity. Potential applications for this sensor include sensing hydrogen in fuel cells [88], dissolved gas sensing in an oil filled power transformer [87] or ethylene during fruit ripening [89].

Chapter 5

Humidity time response of polymer coated fibre Bragg gratings

5.1 Introduction

Sensor response speed is of great practical importance in many applications, where a fast response is expected. This chapter builds on chapter 4 by investigating the time response to large humidity step changes. The rates of absorption and desorption of the coatings were investigated and models proposed for the response.

5.2 Basic concepts

In this section two models are proposed to fit the experimental data obtained when the fibre is exposed to a humidity step change in order to extract time constants and diffusion coefficients of the coated sensor. The first is a simplified version of existing models, which use stretched exponential functions to determine time constants [90]. The second is the basic diffusion equation solved using COMSOL to determine diffusion coefficients [91, 92].

5.2.1 Two-layer model

A two time constant model can be used to model the time response of a humidity step change. Here a fast time constant, τ_f, represents the fast humidity response from the surface layer of the polymer coating and a slow time constant, τ_s, represents the slower humidity response from the inner layer of the polymer coating, as illustrated by Fig 5.1.

To simplify the comparison of sensors that have different Bragg wavelengths the dimensionless relative wavelength change was used, $\Delta\lambda_{B\ rel}$ defined as the ratio of the deviation $\Delta\lambda_B$ of the gratings Bragg reflection wavelength from its original value to the maximum deviation $\lambda_{B\ max}$ caused by the relative humidity step change (5 to 95%rh or 95 to 5%rh), [93], i.e. $\Delta\lambda_{B\ rel} = \Delta\lambda_B/\lambda_{B\ max}$. This

normalises the response to be in the range of zero to one. The time constants τ_f and τ_s are determined by fitting equations 5.1 or 5.2 to the normalised transient response of a wetting or drying humidity step change respectively.

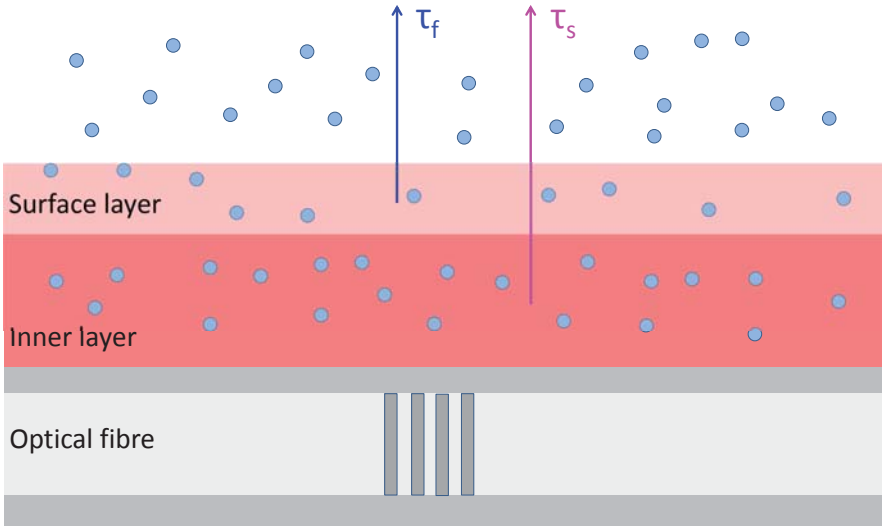


Figure 5.1 – A two layer model with the coating divided into a surface layer with a fast time constant, τ_f, and a inner layer with a slow time constant, τ_s.

$$\Delta\lambda_{B\ rel} = 1 - \left[w_f e^{-\frac{t}{\tau_f}} + w_s e^{-\frac{t}{\tau_s}}\right] \tag{5.1}$$

$$\Delta\lambda_{B\ rel} = w_f e^{-\frac{t}{\tau_f}} + w_s e^{-\frac{t}{\tau_s}} \tag{5.2}$$

Here t is the time since the initiation of step change, and w_f and w_s are the fast and slow weighting parameters respectively. By considering the weightings an effective time constant can be determined. The two time constants can be combined to give an overall effective time constant for the coating using equation 5.3.

$$\tau_{eff} = \left(\frac{w_f}{w_f + w_s}\right)\tau_f + \left(\frac{w_s}{w_f + w_s}\right)\tau_s \tag{5.3}$$

The thicknesses of the surface layer and inner layer are not specified, but the surface layer will make up a greater portion of a thin coating compared to a thick coating. So thin coatings or coatings that have a very fast diffusion might require a larger weighting on the fast time constant and vice versa [94].

5.2.2 Mesh model

The diffusion of a coating on a fibre Bragg grating was modelled with a mesh model to determine the diffusion coefficient. In this model the coated fibre is considered as a cross section with two concentric circles where the inner represents the fibre and the outer represents the coating. The outer circle is divided into a mesh using the appropriate boundary conditions on the inner and outer boundaries (Fig 5.2). The diffusion equation (equation 5.4) can be used to model the change in water concentration (C) with time ($\frac{\partial C}{\partial t}$). This can be simplified to equation 5.5 for a constant diffusion coefficient (D) and by considering symmetry, where r is the radius [95].

$$\frac{\partial C}{\partial t} = \nabla \cdot (D \nabla C) = D \left(\frac{\partial^2 C}{\partial x^2} + \frac{\partial^2 C}{\partial y^2} \right) \tag{5.4}$$

$$\frac{\partial C}{\partial t} = D \left(\frac{\partial^2 C}{\partial r^2} + \frac{1}{r} \frac{\partial C}{\partial r} \right) \tag{5.5}$$

This can be solved numerically using COMSOL with the boundary conditions of an impermeable inner boundary ($\frac{\partial C}{\partial t} = 0$), as the glass optical fibre does not absorb water, and a constant water concentration in the atmosphere surrounding the outer boundary (Dirichlet boundary condition) [91]. The initial conditions for a dry to wet step change has the coating uniformly at 5 %rh and the atmosphere uniformly at 95 %rh and vice versa for a wet to dry step change. Multiple constant diffusion coefficients were trialled and a best fit selected by eye, which may not be a mathematical best fit [95, 96].

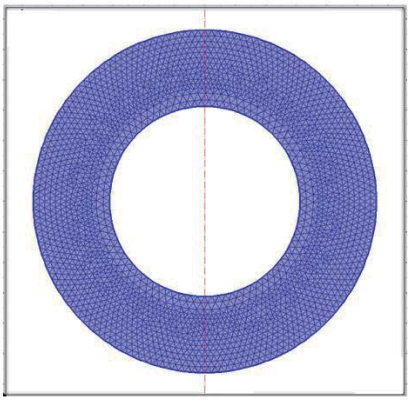
This model assumes Fickian diffusion was taking place with D as a constant independent of concentration. Diffusion in polymers can be separated into three cases:

- Case I: Fickian diffusion which assumes there are no changes in the polymer structure from interactions with the diffusing species and is based on the random walk with no interactions theory. This assumes the diffusion rate is slower than the polymer relaxation rate, so by the time the diffusion process is over the polymer structure is no longer changing and interacting with the diffusant.

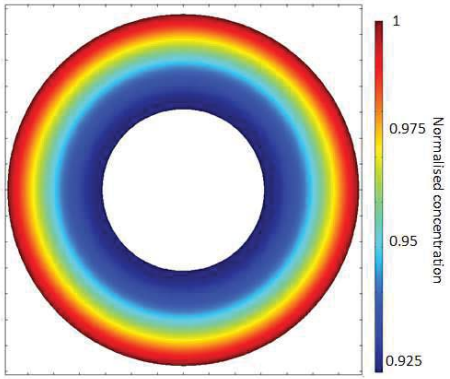
- Case II: Occurs when there are strong interactions between the polymer and the diffusant. Here the diffusion rate is faster than the polymer relaxation rate so when the diffusion process is over the polymer structure is still changing, giving the impression that interactions are still occurring.

- Case III: The final case is when the diffusion rate and polymer relaxation rate occur on the same time scale [91].

Fickian diffusion (case I) has been used to model the time response of diffusion in polymers [57, 91, 93, 97] and is a good place to start, before resorting to the more complicated models assuming non-Fickian diffusion in polymers [98–100].



(a) The fibre coating divided into a mesh.



(b) The fibre coating undergoing water absorption during a simulation.

Figure 5.2 – The mesh model where fibre coating water diffusion was modelled using COMSOL.

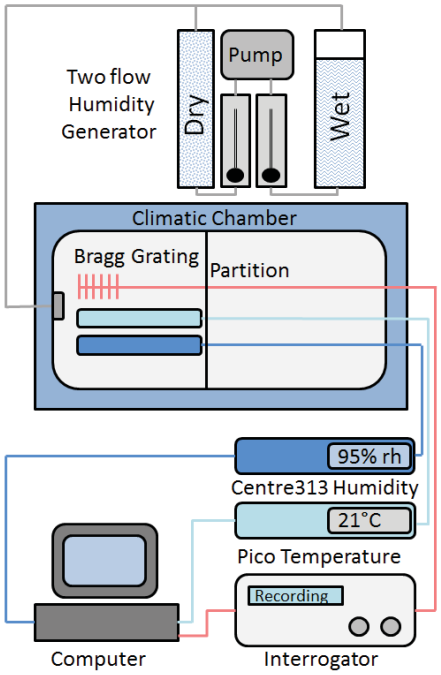
5.3 Experimental method

The humidity time response of the coated fibres was measured using an insulated climatic chamber where humidity could be step changed (Fig 5.3). The position of the Bragg reflection peak was monitored using an optical interrogator (OSA 150D) linked to a computer with a labview program that allowed recording of the peak. The humidity in the chamber was recorded with a Centre 313 probe and the temperature with a PT-104 data logger, with both probes linked to a computer for real-time recording.

A humidity step change in the chamber was controlled using a two-flow humidity generator that generates different humidities by combining a dry air source with a wet air source. This generator could simulate a humidity step change by switching quickly between the total dry (5 %rh) and total wet source (95 %rh) and vice versa. The 2500 Thunder Scientific humidity generator was unsuitable for generating humidity step changes as it relied on a two pressure method to generate humidity, and although highly precise it took minutes to change humidity. A partition was used to reduce the volume of the chamber*. The air entered the chamber through a distributor head to ensure that the fibre did not move with the air flow, which would have caused undesirable strain effects.

Temperature plays a crucial role with any humidity measurement and must be accounted for. Small temperature fluctuations can occur when using the total wet source due to the way the humid air flow is generated. The airflow blows across a saturated material, humidifying the air and drying the material, leading to evaporative cooling. To compensate for this a small heater was in-built into the humidity generator. The external temperature fluctuations were minimised using

*The 9 cm diameter cylindrical chamber was partitioned 6 cm from the air input giving a volume of 382 cm^3. The 6 l/min (6,000 cm^3/min) flow rate resulted in the chamber being replaced 15 times in a minute.



(a) Schematic of the humidity time response setup



(b) The actual setup during a time response measurement.

Figure 5.3 – Experimental setup used to generate humidity step changes.

a polystyrene casing around the chamber and laboratory temperature control was set to 21 °C. In practice small temperature changes did occur (up to 1 °C) which required consideration using the temperature response of the fibre as outlined in chapter 4.

The humidity step change was assumed to be a perfect step change, while in reality this was not the case. However, it approximates a step change when using a small chamber size with a sufficiently high flow rate and switching rapidly between air flows. Another way to simulate a step change involves enclosing the coated FBG in a needle and piercing membranes covering salt solutions [57].

5.4 Pore size measurements

Porous materials are classified by pore size as either microporous (diameter less than 2 nm), mesoporous (diameter between 2 and 50 nm) or macroporous (diameter more than 50 nm). The pore size can be measured by optical imaging, using a scanning electron microscope (SEM) or transmission electron microscope (TEM), or by gas adsorption techniques. Pictures of the fibre coatings using a SEM (Fig 5.4) did not have the resolution to measure the pore size and a TEM would be required. This requires ultra thin samples and would be an expensive time consuming method. Because of this a gas adsorption technique was the

preferred method of measuring the pore size.

The pore size of the polymer coatings was determined using a Micromeritics ASAP 2010 accelerated surface area and porosimetry system, a detailed description of which was given in chapter 3. Two types of 1 gram samples were run, a sample of a polymer film made with the same weight percent, solvent and drying conditions as the coated fibre and a sample of the polymer powder as provided from the supplier.

The P84 polyimide powder was unable to be measured as it was provided by the supplier in solution. Similarly no measurements were able to be made for the pre-coated factory fibres of Avensys polyimide, ormocer and acrylate.

The results of the surface area, total pore volume and pore size measurements are reported in Table 5.1. No difference between the powder and film samples for PMMA and its co-polymers was observed with all samples types exhibiting similar results for surface area, total pore volume and pore size. PVOH-ET also showed no difference between the powder and the film samples with surface area, total pore volume and pore size that was comparable to the PMMA based polymers. Interestingly for its extremely slow time response PVOH-ET has a pore size of 3.5 nm which was the largest of the film samples measured. While PEI possessed a similar pore size, a doubling in surface area and total pore size was observed when going from powder to film. The solution of P84 had results for surface area, total pore volume and pore size that were similar to PMMA and its co-polymers.

The modified PEI yielded interesting results of an increasing surface area and total pore volume and decreasing pore size upon going from powder to film. Both the surface area and total pore volume for the powder and film were significantly higher than that measured for the other polymers, with the exception of P84 HT.

This dramatic increase in total pore volume could be explained by the structural modifications. The reduction in aromatic rings and introduction of side chains protruding from the polymer backbone were postulated to reduce pi-stacking, increasing the voids in the polymer. The pore size decreased from 5.8 to 3.3 nm, which was consistent with other film samples. P84 HT possessed a large surface area that was reduced when dissolved in DMF to make the film sample. A large total pore volume was observed, which could be explained by the reduced aromatic rings leading to less pi stacking and more voids. When going from powder to film the pore size has a dramatic reduction from 7.9 to 3.4 nm.

Overall, the pore size of all the film samples were approximately 3.4 nm, which could be related to the solvent and drying conditions used. The powders provided from the suppliers would most likely have had different solvents and drying conditions used during manufacturing, which could result in the polymer

having different surface area, total pore volume and pore size.

A future study on the control of pore volume and pore size could be conducted, using different solvents and drying conditions. This could be followed up with an investigation of the effect of pore volume and pore size on time response.

Table 5.1 – Surface area, total pore volume and average pore size for the polymer coatings and their powders as supplied.

Polymer		Solvent	Surface area (m^2/g)	Total pore volume (cm^3/g)	Average pore size (nm)
PMMA	film	1,1,2-TCE	13.35	0.0302	3.39
	powder	-	14.36	0.0326	3.39
MAA	film	1,1,2-TCE	14.05	0.0318	3.35
	powder	-	13.82	0.0314	3.37
EA	film	1,1,2-TCE	13.96	0.0316	3.34
	powder	-	14.62	0.0331	3.38
BA	film	1,1,2-TCE	14.13	0.0324	3.35
	powder	-	13.27	0.0301	3.37
PEI	film	1,1,2-TCE	29.55	0.0668	3.36
	powder	-	13.44	0.0304	3.34
Mod PEI	film	1,1,2-TCE	68.11	0.1542	3.34
	powder	-	40.52	0.0915	5.82
P84	film	NEP	13.61	0.0309	3.36
P84 HT	film	DMF	26.72	0.0604	3.41
	powder	-	42.45	0.0978	7.93
PVOH-Et	film	1:1 water/propan-1-ol	14.50	0.0329	3.52
	powder	-	15.08	0.0319	3.34

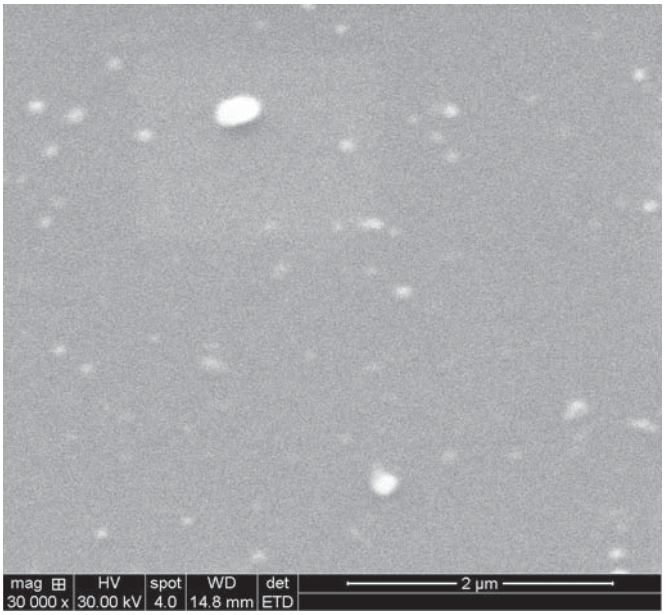


Figure 5.4 – SEM picture of the surface of a P84 film with 30,000x zoom where the particles on the surface are due to dust. The faint rectangle was due to damage caused by the SEM electron beam.

5.5 Poly(methyl methacrylate) fibre coatings

The pore size can influence the diffusion of a polymer, with larger pores having faster diffusion than smaller pores [101]. The coatings of PMMA and its co-polymers possess similar pore sizes of approximately 3.4 nm (Table 5.1), making it possible to directly compare the polymers. The time response to a large humidity step change was investigated (Fig 5.5) and the models fitted (Tables 5.2 and 5.3).

The two layer model gave a best fit with even weightings of the fast and slow time constants for both the water absorption and desorption. For water absorption, the coatings had similar fast time constants of about 3 minutes and slow time constants of approximately 10 minutes, leading to an effective time constants of about 6.5 minutes. The exception was the BA coating which had a slightly faster slow time constant of 7.6 minutes, leading to a slightly faster effective time constant of 5.5 minutes.

For water desorption the coatings had fast time constants ranging from 0.9 to 3.3 minutes and slow time constants of about 6 minutes, leading to effective time constants of around 3.5 minutes. Here the exception was EA, which had a slower slow time constant response of 10.5 minutes. This was reflected in the slower effective time constant of 6.9 minutes. The water desorption is faster than the absorption, which is consistent with other studies on PMMA based coatings [93].

The mesh model was applied to the response data to estimate the diffusion

constants. For water absorption the coatings were similar with diffusion coefficients in the range of 2 - 2.5×10^{-8} cm^2/s, with the exception of BA which had a slightly higher diffusion constant of 4.5×10^{-8} cm^2/s. This reflects what was seen with the time constants with BA having a slightly faster response. This diffusion constant was particularly large as it had the fastest response and was the thickest coating.

For water desorption the coatings of both PMMA and MA were about 3.5×10^{-8} cm^2/s, while EA was quite low at 2.3×10^{-8} cm^2/s which was slightly higher than its absorption rate and BA was the fastest at 6.0×10^{-8} cm^2/s. All the coatings had larger water desorption diffusion coefficients, meaning the water desorption was faster than absorption. This was consistent with observations from other studies. The diffusion coefficients for PMMA have been well studied and were of the same order as the values obtained here [92, 93, 102]. Differences in diffusion constants for the same material are not unexpected with variation due to influences like:

- How the step change is generated - experimentally salt solutions, two-flow generators and other humidity generators will have different abilities to simulate a humidity step change.

- The %rh range of the step - 5 to 95 %rh and vice versa was used here (the largest range used) with smaller ranges used in the literature.

- The pore size of the coating - different pore sizes due to different coating methods could lead to different diffusion constants [93].

- The temperature that the measurement was made - as diffusion constants are highly temperature dependent [103].

- The molecular weight - the length of the polymer chain could influence properties of the polymer such as pore size and volume leading to different diffusion dynamics [101].

- The model used - there are numerous models available to simulate diffusion with different ways to solve a particular model. Here the basic diffusion equation assuming Fickian diffusion was solved using a numerical package COMSOL, while others solve the same equation using different numerical methods [92].

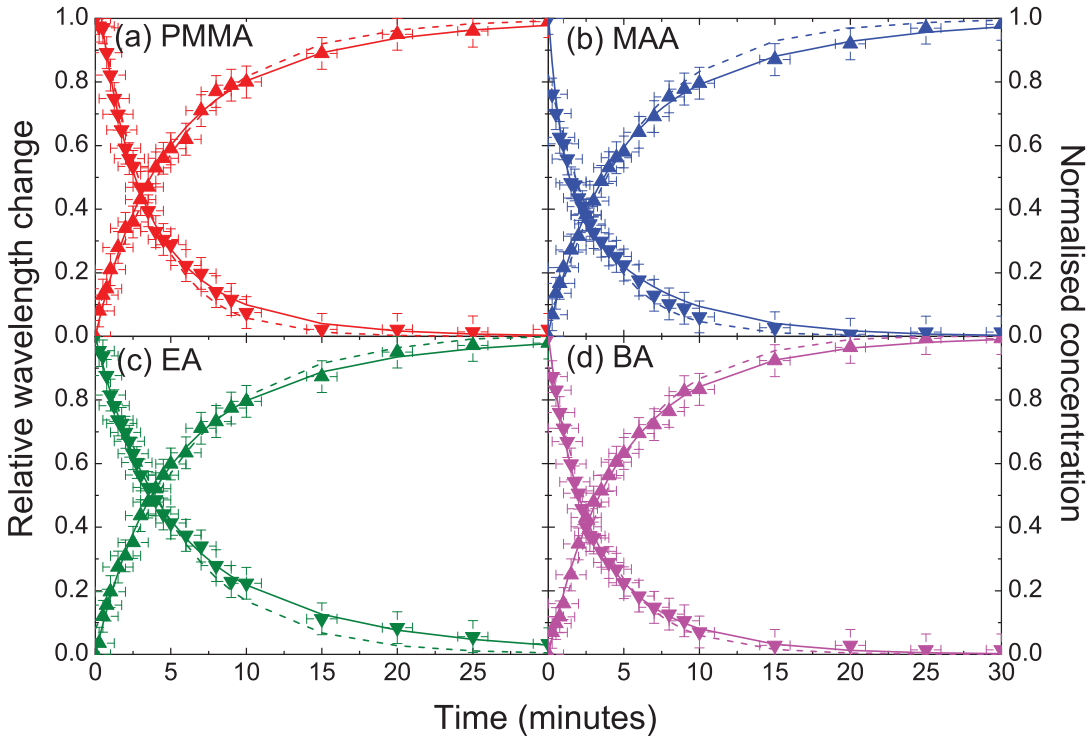


Figure 5.5 – Time response to a 5 to 95 %rh, ▲, and 95 to 5 %rh humidity step change, ▼, for coatings of (a) PMMA, (b) MAA, (c) EA and (d) BA. The solid line is the two layer model fit and the dashed line is the mesh model fit.

Table 5.2 – Table of water absorption parameters.

Polymer	Cladding Diameter (μm)	Thickness (μm)	w_f weighting	τ_f (min)	w_s weighting	τ_s (min)	$\tau_{effective}$ (min)	D (10^{-8} cm^2/s)
PMMA	125	50	0.50	3.2	0.50	9.5	6.3	2.3
MAA	125	51	0.50	3.1	0.50	10.3	6.7	2.5
EA	125	48	0.50	3.3	0.50	9.7	6.5	2.0
BA	125	65	0.50	3.3	0.50	7.6	5.5	4.5
Mod PEI	125	60	0.50	2.0	0.50	5.1	3.5	6.0
Avensys PI	125	18	0.50	3.2	0.50	6.5	4.8	0.4
P84	125	79	0.50	6.2	0.50	16.7	11.5	3.0
P84	125	62	0.50	4.4	0.50	13.5	9.0	2.8
P84	125	23	0.83	0.6	0.17	4.3	1.2	2.4
P84	80	20	0.77	0.4	0.23	4.3	1.3	2.2
P84	54	19	0.77	0.4	0.23	3.0	1.0	1.3
P84 HT	125	53	0.91	5.4	0.09	14.8	6.3	2.5
Ormocer	125	33	0.50	5.1	0.50	14.3	9.7	0.7
Centre313	-	-	-	-	-	-	1.0	-

Table 5.3 – Table of water desorption parameters.

Polymer	Cladding Diameter (μm)	Thickness (μm)	w_f weighting	τ_f (min)	w_s weighting	τ_s (min)	$\tau_{effective}$ (min)	D (10^{-8} cm^2/s)
PMMA	125	50	0.50	1.9	0.50	5.6	3.7	4.0
MAA	125	51	0.50	0.9	0.50	6.0	3.4	4.0
EA	125	48	0.50	3.3	0.50	10.5	6.9	2.3
BA	125	65	0.50	1.7	0.50	5.4	3.6	6.0
Mod PEI	125	60	0.50	1.5	0.50	8.6	5.0	5.0
Avensys PI	125	18	0.67	2.2	0.33	8.2	4.2	0.5
P84	125	79	0.50	2.9	0.50	13.6	8.2	4.8
P84	125	62	0.50	2.5	0.50	13.9	8.2	4.0
P84	125	23	0.50	0.2	0.50	0.6	0.4	5.0
P84	80	20	0.77	0.4	0.23	3.5	1.1	3.0
P84	54	19	0.77	0.3	0.23	1.1	0.5	1.3
P84 HT	125	53	0.77	3.7	0.23	16.3	6.6	2.5
Ormocer	125	33	0.50	2.5	0.50	12.6	7.6	0.9
Centre313	-	-	-	-	-	-	0.9	-

5.6 Polyetherimide fibre coatings

The time response of the modified polyetherimide to humidity step changes was investigated (Fig 5.6) with the responses fitted with the models (Tables 5.2 and 5.3). The best fit of the two layer model was with an even weighting with a fast time constant of 1.5 minutes and a slow time constant of 8.6 minutes, giving an effective time constant of 5.0 minutes. This result was fast given the 60 μm coating thickness, leading to the large absorption and desorption coefficients of 6.0 and 5.0×10^{-8} cm^2/s respectively, which were the highest values of the polymers investigated. This fast diffusion could be due to the larger pore volume formed by the addition of the side chain, where moisture can enter and escape with greater ease.

In addition, the diffusion coefficients might be slightly overstated as the mesh model struggled to fit the data, leading to a fit that was outside the errors of the data in some places. This could be due to the model being a Fickian model and might be improved if a non-Fickian model was developed.

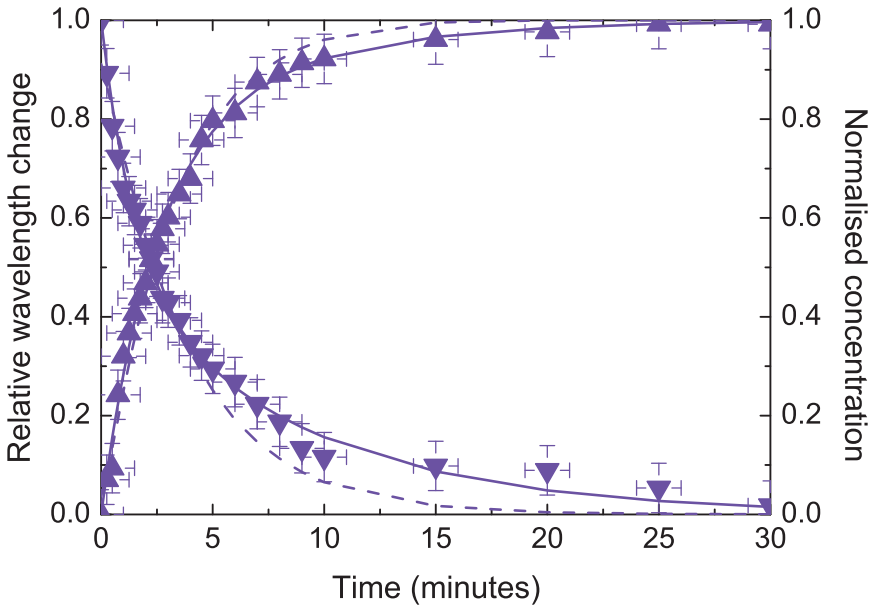


Figure 5.6 – Time response to a 5 to 95 %rh, ▲, and 95 to 5 %rh humidity step change, ▼, for a 60 μm coating of modified PEI. The solid line is the two layer model fit and the dashed line is the mesh model fit.

5.7 Polyimide fibre coatings

The time response of polyimide coatings to humidity step changes were investigated, including the effect of coating and fibre cladding thickness. A default factory polyimide coated FBG from Avensys and fibres dip coated with P84 and P84 HT were trialled.

5.7.1 Avensys polyimide

A pre-coated polyimide FBG from Avensys was exposed to humidity step changes (Fig 5.7a), and the response fitted with the models (Tables 5.2 and 5.3). The two layer model gave a best fit to the absorption data with an even weighting with a fast time constant of 3.2 minutes and a slow time constant of 6.5 minutes, leading to an effective time constant of 4.8 minutes. The best fit to the desorption data was with a weighting slightly loaded towards the fast time constant with a fast time constant of 2.2 minutes and a slow time constant of 8.2 minutes, leading to an effective time constant of 4.2 minutes. The mesh model gave a good fit with diffusion constants of 0.4×10^{-8} cm^2/s for absorption and 0.5×10^{-8} cm^2/s for desorption, with slightly faster diffusion than absorption. This followed the trend of PMMA and its co-polymers and some other polyimides reported in the literature [91]. This was a slow response, especially for a relatively thin 18 μm coating, leading to the the lowest diffusion coefficient values of the polymer coatings investigated.

5.7.2 P84 polyimide

As the polyimide P84 was provided in solution it gave excellent quality coatings of uniform thickness that were highly repeatable. As such, it was chosen for an investigation into the effect coating thickness and fibre cladding thickness.

Effect of coating thickness

Coatings of 23, 62 and 79 μm thickness were exposed to humidity step changes (Fig 5.8), and the response fitted with the models (Tables 5.2 and 5.3). The two layer model gave the best fits for absorption and desorption with even weightings, with an exception of the absorption data of the 23 μm coating, which was highly weighted towards the faster time constant. For the coatings of 79, 62 and 23 μm thickness the absorption effective time constants were 11.5, 9.0 and 1.2 minutes and the desorption effective time constants were 8.2, 8.2 and 0.4 minutes respectively. A clear trend was observed with the effective time constants becoming significantly faster as the coating thickness reduces (Fig 5.8a inset).

This could be attributed to the increasing ratio of the surface to inner layer. A larger portion of the 23 μm coating comprises of the surface layer, reflected by its larger fast time constant weighting. This faster response with thinner coatings was consistent with observations in other studies [57]. The absorption diffusion coefficients range from 1.3 to 2.4×10^{-8} cm^2/s and desorption coefficients range from 0.4 to 1.1×10^{-8} cm^2/s, with desorption being faster than absorption for all the coatings.

Effect of cladding thickness

Fibre cladding diameters of 125, 80 and 54 μm with P84 polyimide coatings of about 20 μm thickness were exposed to humidity step changes (Fig 5.9), and the

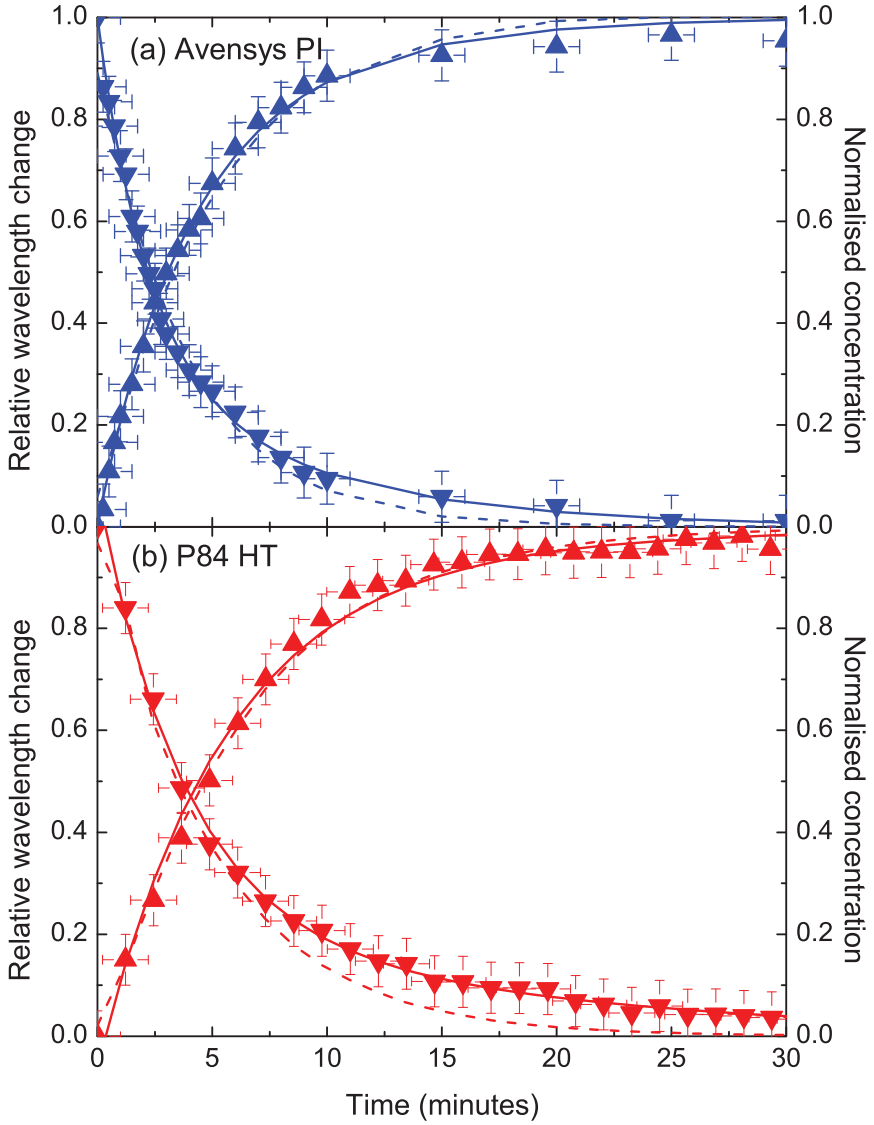


Figure 5.7 – Time response to a 5 to 95 %rh, ▲, and 95 to 5 %rh humidity step change, ▼, for coatings of (a) Avensys PI and (b) P84 HT. The solid line is the two layer model fit and the dashed line is the mesh model fit.

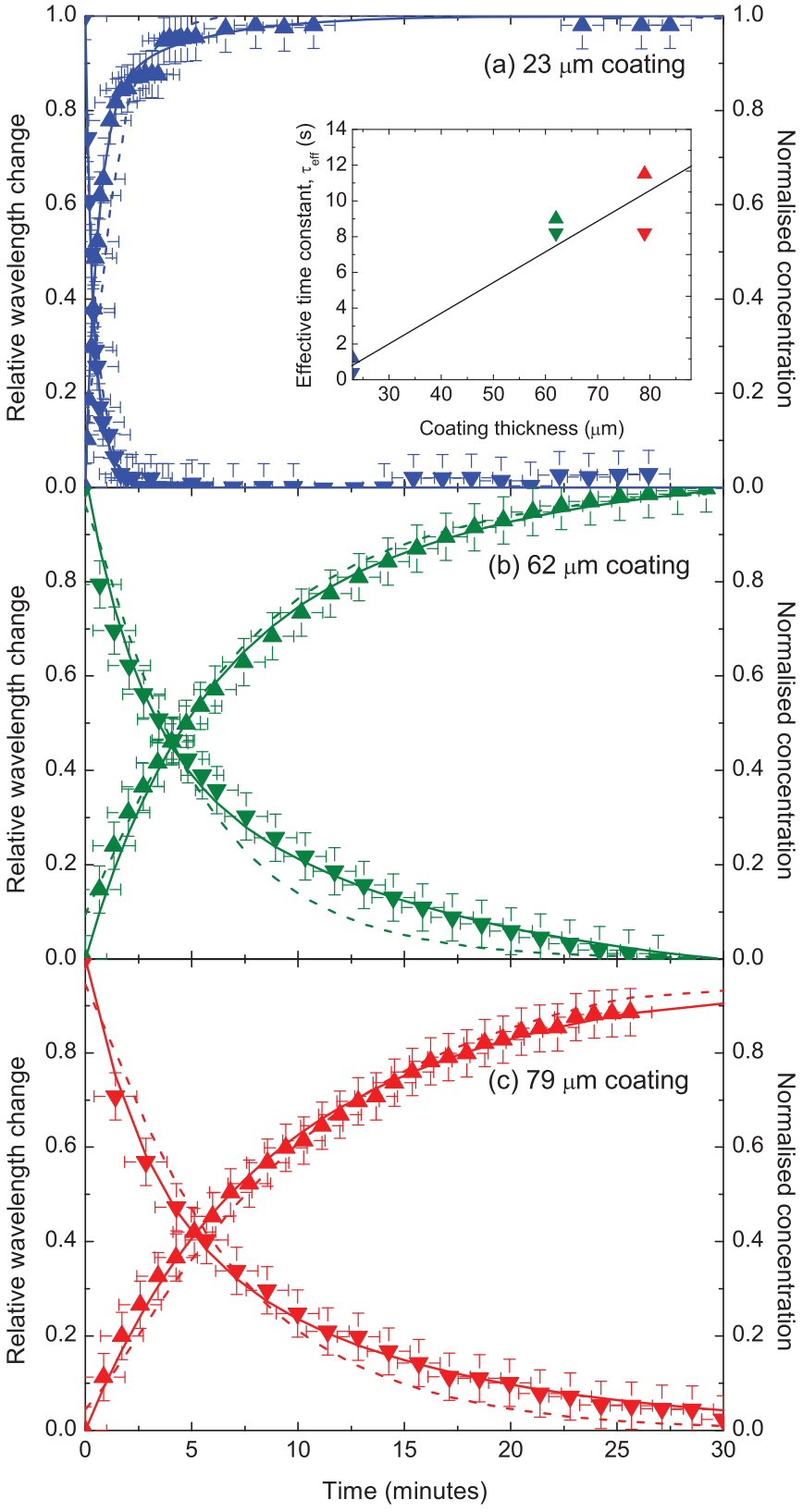


Figure 5.8 – Time response to a 5 to 95 %rh, ▲, and 95 to 5 %rh humidity step change, ▼, for P84 coatings of (a) 23, (b) 62 and (c) 79 μm thickness. The solid line is the two layer model fit and the dashed line is the mesh model fit. The inset shows effective time constant with coating thickness. The line is just a guide.

response fitted with the models (Tables 5.2 and 5.3). The two layer model had large weightings to the fast time constant for both absorption and desorption indicating that the surface layer comprised a large portion of the coating. The absorption fast time constants ranged from 0.4 to 0.6 minutes and the slow time constants from 3.0 to 4.3 minutes resulting in very similar effective time constants from 1.0 to 1.2 minutes. While the desorption fast time constants ranged from 0.2 to 0.4 minutes and the slow time constants from 0.6 to 3.5 minutes resulting in very similar effective time constants from 0.4 to 1.1 minutes (Fig 5.9a inset). This time response performance equaled or exceeded that of the independent commercial dielectric sensor used to monitor the chamber (Fig 5.10), which had an absorption effective time constant of 1.0 minutes and an desorption effective time constant of 0.9 minutes (Tables 5.2 and 5.3).

Even though the thickness of the coating on the fibres was approximately the same, the volume of the coating on a given fibre would be different due to different sized claddings. In this case no appreciable time difference was seen between the fibres, but at larger coating thickness an appreciable difference due to the volume might be observed.

The mesh model had similar absorption diffusion constants, between 1.0 to 1.3×10^{-8} cm^2/s, and desorption diffusion coefficients, between 0.4 to 1.1×10^{-8} cm^2/s. The model struggled to fit the 80 μm diameter fibre for both absorption and desorption, with fits outside the errors of the data in some places. The diffusion constants followed the same trend as the other P84 coated fibres where desorption was faster than absorption.

5.7.3 P84 HT polyimide

A fibre was coated with a 53 μm coating of P84 HT and exposed to humidity step changes (Fig 5.7b), and the response fitted with the models (Tables 5.2 and 5.3). The two layer model had large weightings to the fast time constant for both absorption and desorption. This model gave a best fit with an absorption fast time constant of 5.4 minutes and slow time constant of 14.8 minutes, leading to an effective time constant of 6.3 minutes.

For desorption a best fit was with an absorption fast time constant of 3.7 minutes and slow time constant of 16.3 minutes, resulting in an effective time constant of 6.6 minutes. Both absorption and desorption were similar, with absorption potentially being a faster. The mesh model gave a diffusion constant of 2.5×10^{-8} cm^2/s for both absorption and desorption. Here the model struggled with fitting the desorption data, possibly overstating the diffusion constant by a small amount. The diffusion constants were of the same order as those obtained for P84.

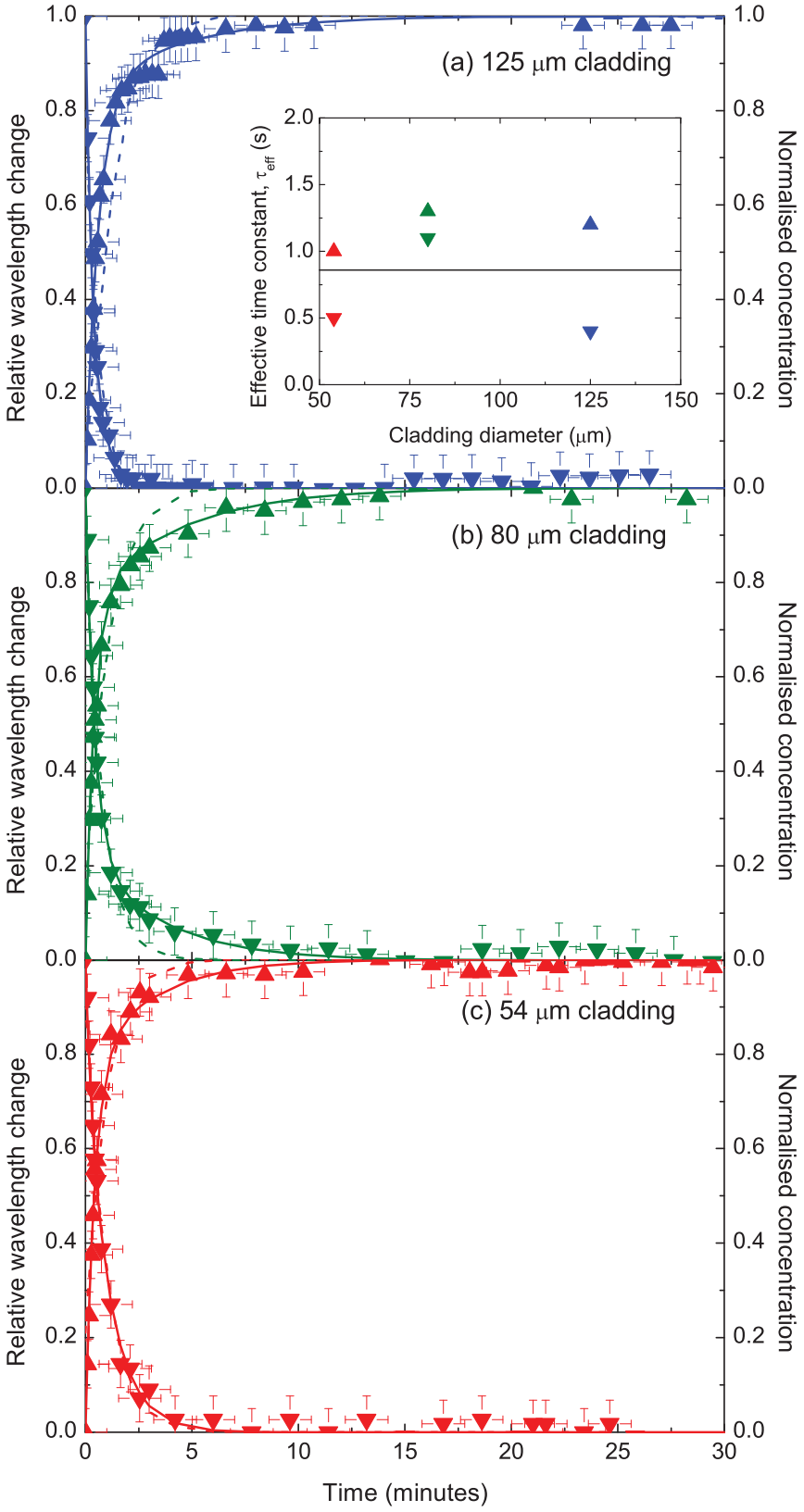


Figure 5.9 – Time response to a 5 to 95 %rh, ▲, and 95 to 5 %rh humidity step change, ▼, for a P84 coating of about 20 μm thickness on fibres with cladding diameter of (a) 125, (b) 80 and (c) 54 μm thickness. The solid line is the two layer model fit and the dashed line is the mesh model fit. The inset shows effective time constant with cladding diameter. The line is just a guide.

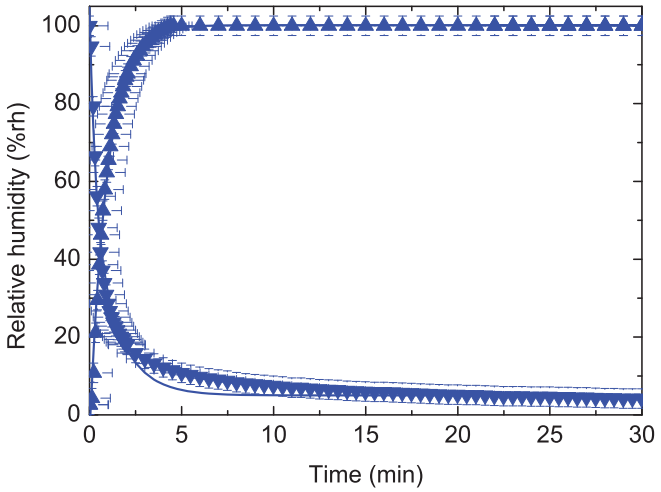


Figure 5.10 – Time response to a 5 to 95 %rh, ▲, and 95 to 5 %rh humidity step change, ▼, for the commercial dielectric centre 313 humidity probe. The solid line is an exponential model fit.

5.8 Other fibre coatings

Of the other coatings investigated, the acrylate coating and no coating (bare glass fibre) had no observed humidity response, and the PVOH-ET coated fibre had an extremely slow time response and was not measured, leaving only ormocer to be investigated.

A pre-coated fibre with a 33 μm coating of ormocer was exposed to humidity step changes (Fig 5.11), and the response fitted with the models (Tables 5.2 and 5.3). The two layer model gave a best fit with even weightings with an absorption fast time constant of 5.1 minutes and slow time constant of 14.3 minutes, leading to an effect time constant of 9.7 minutes and a desorption fast time constant of 2.5 minutes and slow time constant of 12.6 minutes, leading to an effect time constant of 7.6 minutes. This was quite slow given the coating was only 33 μm. The diffusion coefficients gave a best fit with 0.7×10^{-8} cm^2/s for absorption and 0.9 x 10×10^{-8} cm^2/s for desorption, giving faster desorption rate. These diffusion constants were among the lowest of the coatings investigated.

5.9 Summary and future work

In summary, the time response of coated fibre Bragg gratings to humidity step changes of 5 to 95 %rh and 95 to 5 %rh were investigated for poly(methyl methacrylate), polyetherimide, polyimide and ormocer based coatings. A two layer model was proposed with a fast time constant representing the portion of the coating that can have humidity easily occupy and exit and a slow time constant for the deeper part of the coating that is slower to respond.

This model was able to give good fits to the experimental data and give an in-

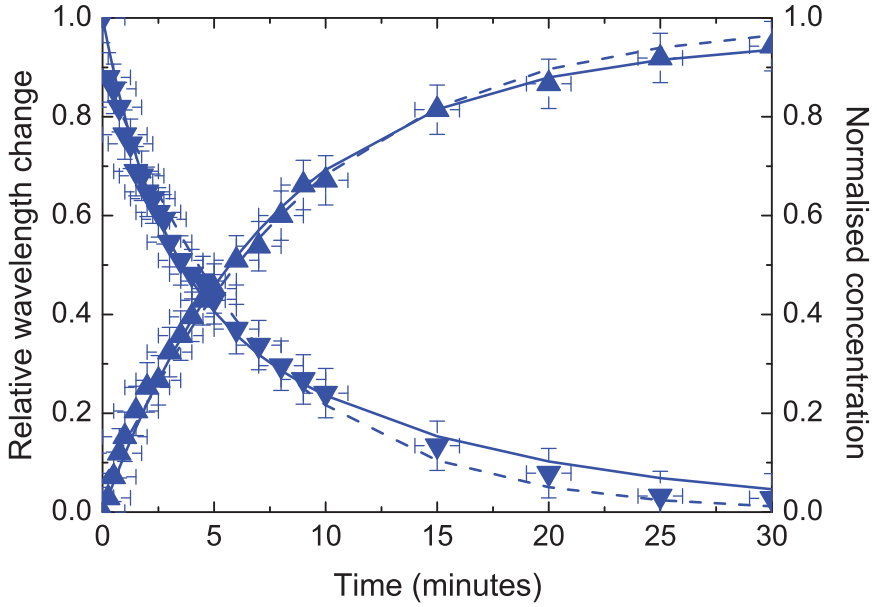


Figure 5.11 – Time response to a 5 to 95 %rh, ▲, and 95 to 5 %rh humidity step change, ▼, for a 33 μm coating of ormocer. The solid line is the two layer model fit and the dashed line is the mesh model fit.

sight into the coatings humidity response, allowed the time response performance to be compared. A mesh model assuming Fickian diffusion was modelled using COMSOL to extract the diffusion constants for water absorption and desorption of the coatings. This model sometimes struggled with fitting and potentially could be improved by utilising a non-Fickian diffusion model. The pre-coated polyimide fibre from Avensys had the lowest absorption and desorption diffusion constants, it was not possible to speculate why, as the chemical structure or any pore size and volume information was not known. The modified PEI had the highest absorption and desorption diffusion constants which could be possibly due to its large pore volume caused by the addition of the side chain. The effect of coating thickness and fibre cladding diameter was examined with the time response increasing dramatically with increasing coating thickness. No significant time response difference was observed for a coating of the same thickness on fibres with different cladding diameters. The thin P84 coatings of approximately 20 μm possessed effective time constants that were comparable or exceeding that of the commercial dielectric centre313 humidity probe.

Future work could focus on investigating methods of controlling the pore size and pore volume, such as blending a filler polymer that can be washed out in a solvent that only the filler polymer is soluble in [104], and investigating the effect on time response. There will a delicate trade off between a fast response and maintaining a large humidity response (nm shift). This can be optimised depending on the application the sensor is being used for.

Another study could look at an investigation of different solvents and drying

conditions to determine if there is an effect on the formation of pore size and pore volume and how that affects the time response. A different focus could be adapting the coatings to sense a different vapour or gas instead of humidity. Cross sensitivity will be a key concern, which could be addressed by using membranes to selectively screen the gas.

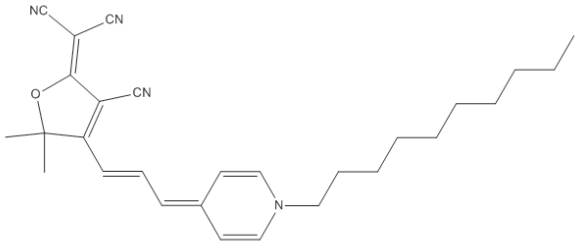
Chapter 6

Fabrication of planar dye-doped polymer Bragg grating sensor

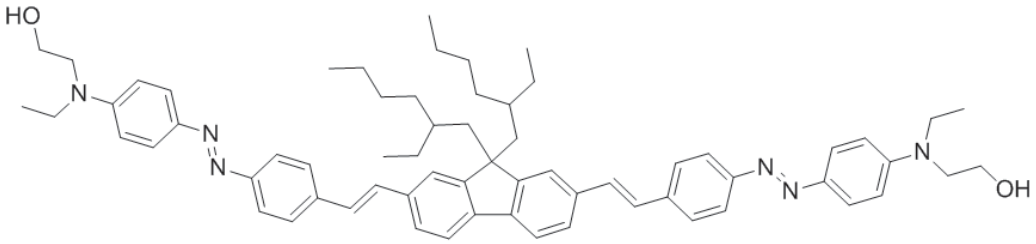
6.1 Introduction

Bragg gratings in silica fibre were first demonstrated in the 1970s and are now widely available for telecommunications and sensing applications [1]. While traditionally focused on strain and temperature sensing, recent attention has been given to their use as chemical and humidity sensors [55]. Bragg gratings can also be written in plain and micro-structured PMMA polymer fibre using UV light [105]. They have been shown to be more sensitive to humidity changes than silica fibre, as the entire fibre absorbs water rather than just the fibre coating. However, they have a significantly slower response time [106–108]. Waveguides and Bragg gratings have been written in planar PMMA films, taking advantage of the same permanent refractive index change from UV light exposure and are promising sensors [54, 109, 110]. Planar dye-doped polymer films with waveguides and Bragg gratings have been demonstrated using DR-1 doped polymer films with Bragg reflections observed [111–117]. This chapter outlines the development of a planar dye-doped polymer film sensor for the purpose of strain temperature and chemical sensing. The design concept and details on sensor fabrication are given in this chapter with its use as a sensor detailed in chapter 7.

Planar films offer advantages of a thinner sensor, while still maintaining the structural integrity that a similar sized fibre would not have. It also allows the creation of two dimensional structures, like rosettes where strain tensors can be resolved. The planar film only needs to be bound by a cladding on one side to achieve a single-mode waveguide. This allows vapour access to the waveguide on the unbound side increasing the response speed. It also allows access to the evanescent wave, analogous to side polished fibres, opening up new sensing opportunities. However, initially planar films are more challenging to mass produce as they require spin coating compared to polymer optical fibre that is extruded. Utilising dye doping offers advantages of controlling the induced refractive index by doping loading and a greater refractive index difference compared to polymer and silica optical fibre. A highly polarised zwitterionic dye offers the potential



(a) The dye PYR-3 (4[2-(N-decylpyridin-4(1H)-ylidene)ethenyl]-3-cyano-5,5-dimethyl-2(5H)-furanylidene propanedinitrile).



(b) The dye BAF-1 (2,7-bis(4-((4-(ethyl(2-hydroxyethyl)amino)phenyl)diazenyl)-styryl) (9,9-bis(2-ethylhexyl)-fluorene)).

Figure 6.1 – Dyes used in the fabrication of the film sensors.

of enhanced sensitivity during strain, temperature and vapour sensing due to a greater induced refractive index change. However, the drawbacks of dye-doping include the additional cost of the dye and extra fabrication step of doping the polymer. Initially photo-degradation is an advantage, allowing structures to be created. However, once created any light in the absorption band in the presence of oxygen will degrade the structure [118–121]. This gives the requirement of enclosing the sensor for long term use, protecting it from ambient light or oxygen, and using non-absorbing light in the waveguide.

6.2 Basic concepts

6.2.1 Introduction to dye doping

The refractive index of a polymer can be increased by doping with a dye, which can then be selectively photo-degraded (bleached) lowering the refractive index. This allows structures like waveguides and Bragg gratings to be created in planar dye-doped polymer films. The dyes used in this thesis are PYR-3, a second-order non-linear optical chromophore and BAF-1, a photo-switchable chromophore (Fig 6.1). Dyes get their distinctive colour by absorbing light in a particular wavelength range. In the case of PYR-3 this occurs via a charge transfer along its conjugated π-bridge. This absorption is what causes the refractive index increase, with the increase extending to wavelengths where the dye does not absorb. The dyes absorption is lost when the conjugated π-bridge is broken, lowering the induced refractive index.

The main mechanism of bridge breaking is via the addition of singlet oxygen ($^1O_2$) (Fig 6.2) [118]. Due to its small size, oxygen readily permeates the polymer where the dye acts as an effective sensitizer in generating singlet oxygen. It does this by absorbing light in its absorption band, transitioning from its ground state to an excited state, then via an inter-system crossing to a long life time triplet state which is quenched by triplet ground state oxygen ($^3O_2$) forming singlet state oxygen ($^1O_2$) (Fig 6.3) [118–125]. This singlet oxygen can then react with the dye to photo-degrade it. The lifetime of the singlet state of PYR-3 is between 0.5 ns and 3.3 ns depending on dye concentration. The life time of the PYR-3 triplet excited state is unknown. However, typically for dyes it is in the ms to s range [126, 127]. After this the photo-degraded dye remains in the polymer leaving a small residual refractive index increase, rather than returning to the undoped polymer refractive index.

The above photo-degradation mechanism applies to PYR-3 only, which has been extensively studied [118–123]. However, the photo-degradation of BAF-1 has not been studied and the mechanism is unknown. A possible mechanism of photo-degradation could follow that of other azo dyes. Here BAF-1 would follow a similar process as PYR-3 and absorb a photon then transition via an inter-system crossing to a long life time triplet state, which is subsequently quenched by triplet ground state oxygen ($^3O_2$) forming singlet state oxygen ($^1O_2$). This singlet oxygen could then react directly with BAF-1 to break the conjugated π system, or it could react with water to form peroxide which subsequently reacts with the dye [128].

6.2.2 Film sensor design concept

The central sensing component of the doped polymer film sensor is the Bragg grating housed in a waveguide. The sensor is formed by spin coating a solution of polymer and dye to form a thin film. Next a waveguide is formed by placing a lithographic mask over the film and selectively photo-degrading the uncovered portion of the film. Finally, the Bragg grating is inscribed into the waveguide by bleaching a refractive index modulation using a two beam interference pattern created by a phase mask (Fig 6.4).

By controlling the film thickness and the width of the lithographic mask the dimensions of the waveguide can be controlled to create a single-mode waveguide. The refractive index contrast between the waveguide and its claddings determine the single-mode waveguide dimension range. If the waveguide is smaller than this range then no light can propagate in the waveguide and conversely if it is larger then multiple modes are propagated. The waveguide is bounded on its sides by claddings of bleached polymer with air bounding it from above and below. To obtain a single-mode waveguide for a film in the 4 to 8 μm range* one or two

*The calculations for single-mode conditions were determined using the vectorial mode solver

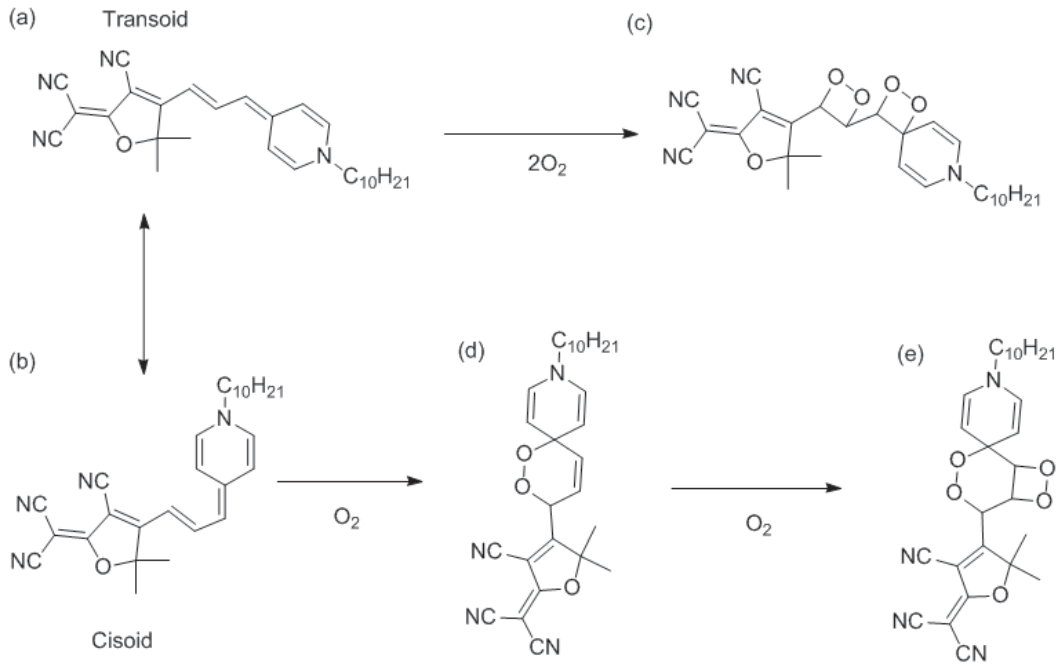


Figure 6.2 – The transoid (a) and cisoid (b) structures of PYR-3 and its expected products formed after photo-oxidation (c), (d) and (e) [118, 122].

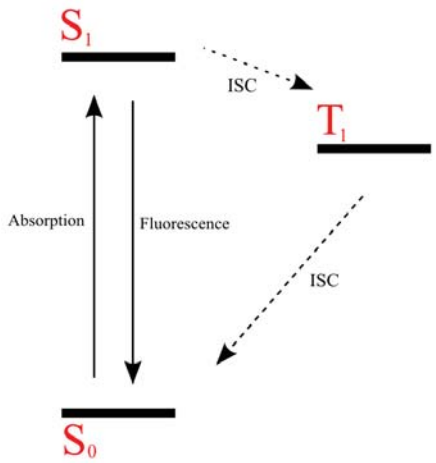


Figure 6.3 – Three level model for the dye absorbing light and transitioning from its ground state (S_0) to its excited state (S_1), then undergoing an inter system crossing (ISC) to a long lifetime forbidden state (T_1). This state was then quenched by triplet ground state oxygen ($^3O_2$) forming singlet state oxygen ($^1O_2$), returning the dye to its ground state [118, 122].

cladding layers on the film are required. If no claddings are used then the film is multi-mode with multiple Bragg reflections observed, making tracking their shift while sensing difficult [129]. For this reason single-mode waveguides resulting in a single Bragg reflection are desirable. Although the design used in this thesis is a single linear waveguide, as a planar film is used more exotic waveguides with multiple Bragg gratings, such as a rosette, can easily be created.

To allow the polymer film sensor to be connected to optical components a single-mode glass optical fibre is glued to the end of the waveguide with an additional glass slide housing unit used to give support and strength to the connection (Fig 6.5).

6.3 Sensor fabrication

The sensor manufacture involves a step wise process of dye-doped film fabrication, waveguide inscription, Bragg grating writing and coupling to give the Bragg reflection.

6.3.1 Film fabrication

The foundation of the sensor is the dye-doped polymer film, which is formed by spin-coating a solution onto a glass substrate. The 25 × 25 × 1 mm square glass substrates are rigorously cleaned using a standard procedure [45] and stored in an 80 °C oven before use. As the film is removed from the glass slide before coupling, the refractive index of the substrate is not important. The film thickness is controlled by the solution viscosity and spin speed (Fig 6.6).

The solutions used for spin coating were prepared by dissolving the dye and polymer in 1,1,2-trichloroethane (50 °C with a stir bar at 500 rpm for 48 hours) at the weight percent required for the desired film thickness[†]. They were filtered through a 0.45 μm filter and an optional 0.2 μm filter followed by a 15 minute degas with a sonicator and left to stand for 10 minutes. This removes undissolved solids and air bubbles introduced during filtering that would spoil the film quality.

The films were prepared in a clean room to minimise the effects of dust and other particles that could reduce the film quality. Before spin coating the glass substrates were removed from the oven and allowed to cool to room temperature before labelling and using compressed air to remove any dust. Part of the solution was quickly poured to cover the substrate and the spin cycle commenced. If the solution was left to stand it could dry giving an uneven film. After coating the films were left for 24 hours to dry in ambient conditions before drying in a Labline programmable temperature vacuum oven (Model 3618PDM) with a vacuum

MODE from Lumerical Solutions with the method outline in reference [7].

[†]For example a typical solution used for spin coating 7 μm 3wt% PYR-3 doped PMMA films was a 15 g 14wt% solution containing solids of 0.0630 g PYR-3 and 2.0370 g PMMA with 12.9 g 1,1,2-TCE spin coated at 2000 rpm.

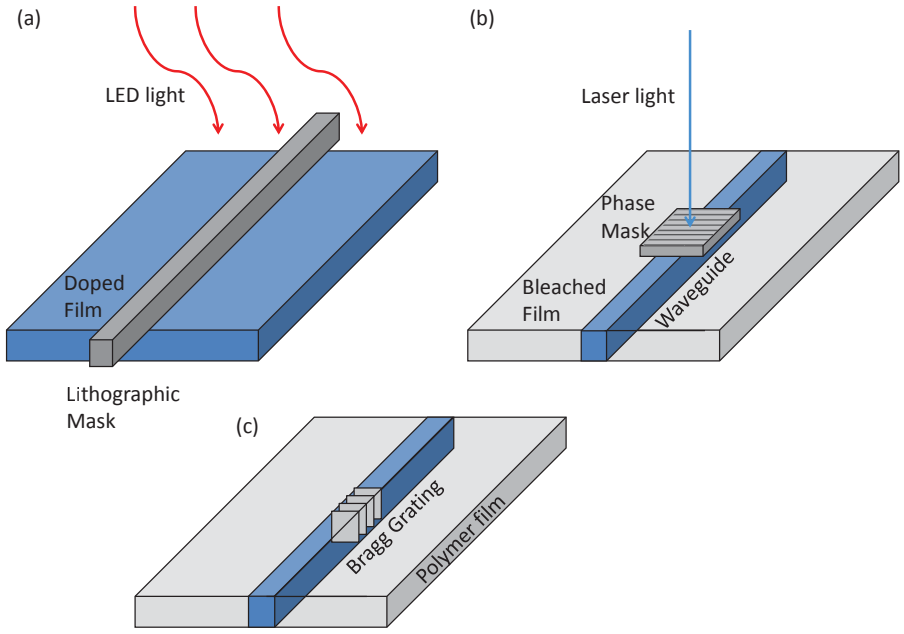


Figure 6.4 – The sensor is fabricated by making a dye-doped polymer film and (a) bleaching a waveguide then (b) using a phase mask to write a Bragg grating giving (c) a sensor that is analogous to fibre Bragg gratings.

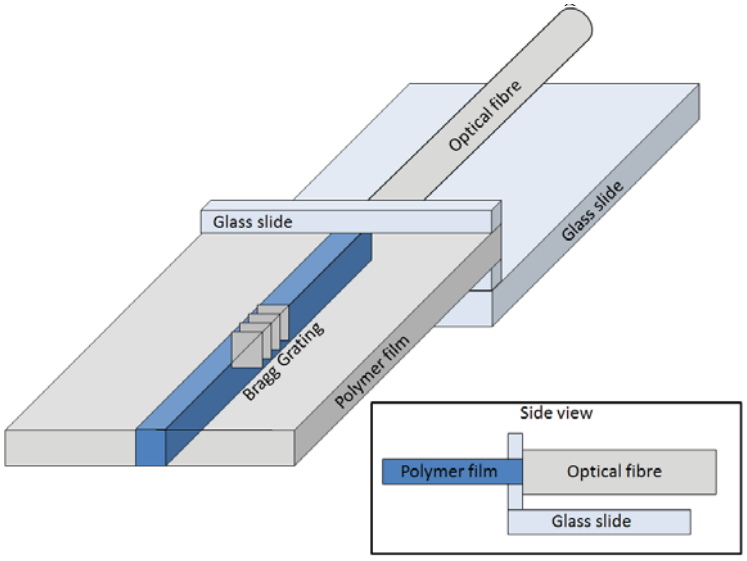


Figure 6.5 – Glass slide housing to secure the optical fibre connection to the polymer film.

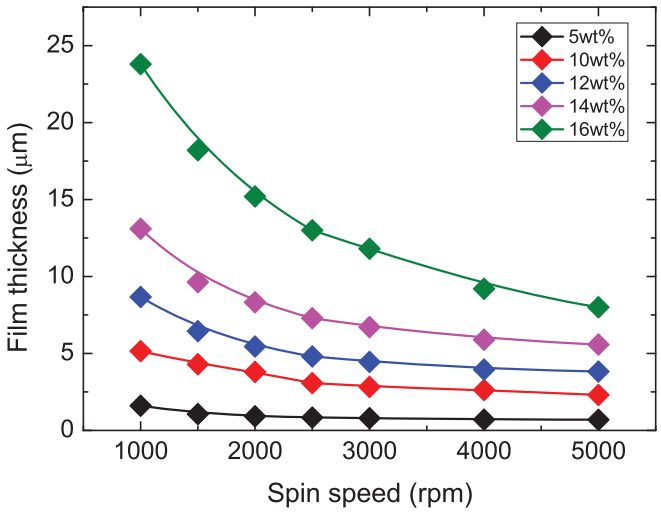


Figure 6.6 – Effects of spin speed and solution viscosity on film thickness for PMMA (MW 350k) in 1,1,2-TCE.

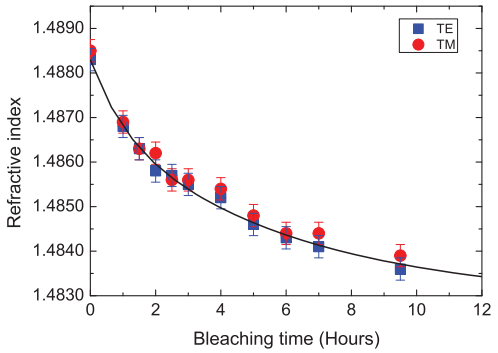
of 110 Torr. A heating ramp from room temperature of 1 °C per minute to 50 °C was applied and held for 8 hours, before a ramp of 0.5 °C per minute up to 80 °C held for 8 hours, after which the oven was allowed to cool to room temperature.

The number of modes in a waveguide can be greatly reduced by adding a lower refractive index cladding. For PMMA films it was possible to add one or two undoped PMMA cladding layers by spin coating additional layers directly on top of dried previous layers. No distortion of the layers was observed and this can be attributed to PMMA taking a long time to be dissolved in the 1,1,2-trichloroethane. This method did not work using amorphous polycarbonate (APC) or when using other solvents, where the film was immediately distorted. An alternative cladding for PMMA is to use a cyclic olefin polymer, which is soluble in solvents that PMMA is not [107]. If only one cladding was required the doped layer was spin coated first to maximise film evenness with the refractive index and thickness of the films measured using a Metricon 2010 prism coupler before successive layers were added.

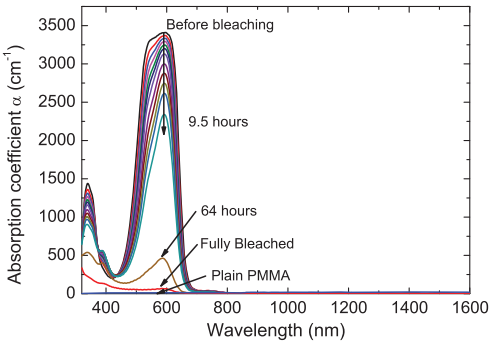
6.3.2 Waveguide inscription

Waveguides were formed by placing a lithographic mask of the desired waveguide dimension on the film and selectively photo-degrading the uncovered portion of the film. The lithographic masks were formed by photo-lithography [130], and had a selection of waveguides ranging from 5 to 120 μm with alignment markers to aid with the precise position of the film. When forming waveguides in PYR-3 doped films a 525 or 625 nm LED was used, with optimum bleaching times of 48 and 12 hours respectively. In Fig 6.7 an exponential decay rate during bleaching is observed, where the rate depends on the concentration of the dye [45, 118, 122, 123]. The photo-products in a 'fully'[‡] bleached film are still absorbing, this

[‡]Even after weeks of bleaching a trace amount of dye could be remaining in the film.



(a) Refractive index change during bleaching with no birefringence observed.



(b) Absorption change during bleaching. A plain undoped PMMA film is also plotted.

Figure 6.7 – The refractive index and absorption change over time of a 7 μm thick 3wt% PYR-3 doped PMMA film during bleaching with a 625 nm LED held 50 mm from the film surface.

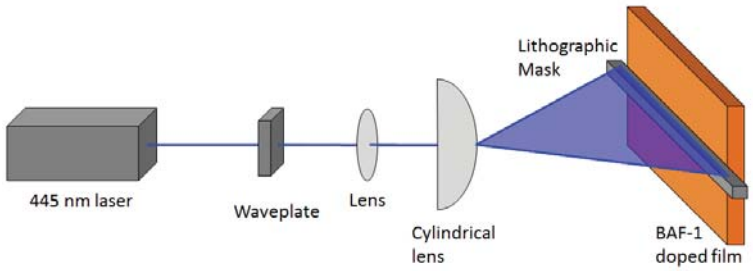
accounts for the refractive index of a 'fully' bleached film being higher than an undoped film[§].

Care had to be taken while bleaching waveguides, for if the waveguide was under-bleached then there was an insufficient refractive index difference between the waveguide and its cladding to support light propagation. Conversely, if the waveguide was over-bleached from scattered light then the waveguide was erased. The BAF-1 dye was significantly more photo-stable than PYR-3 and required much more intensive bleaching when forming waveguides. Light from a 600 mW 445 nm diode laser was focused with a cylindrical lens to form a thin strip along the waveguide and bleached for 6 hours. The laser light was linearly polarised so a half-wave waveplate was used to convert it to a circular polarisation. This deters the dye from aligning with the laser light, preventing effective bleaching (Fig 6.8).

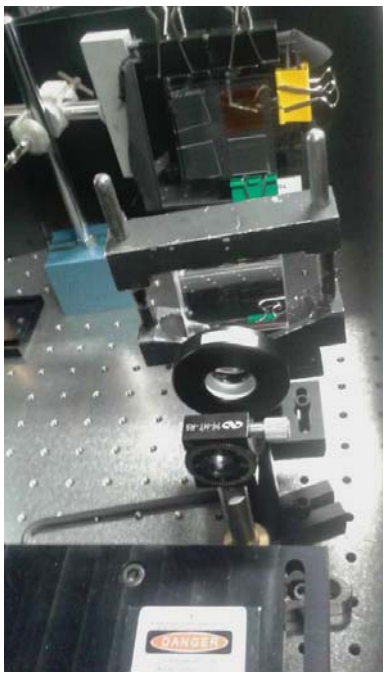
Square waveguides were preferred to simplify the calculation of the single-mode conditions, with 7 μm waveguides formed in 7 μm thick films (Fig 6.9). The single-mode conditions were calculated using the vectorial mode solver MODE from Lumerical Solutions and determined to be 4 - 8 μm for double cladded waveguides and 5 - 8 μm for single cladded waveguides. These dimensions did not take into consideration the shape of the input beam, as a single-mode input was used the waveguide might still have had a single-mode output with dimensions slightly larger than 8 μm [7].

The refractive index increase on doping and its subsequent removal by bleaching with light in the absorption band of the dye is the basis of formation of waveguides and Bragg gratings. The expected refractive index of the film was

[§]A residual refractive index increase of 0.0010 due to residual photo-products was observed for a fully bleached 3wt% PYR-3/PMMA film at 1550 nm.

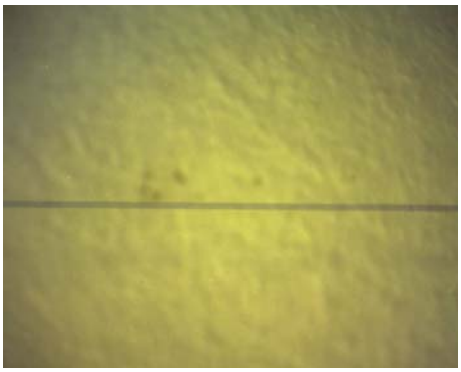


(a) Schematic of the setup used for bleaching waveguides in BAF-1 doped films.

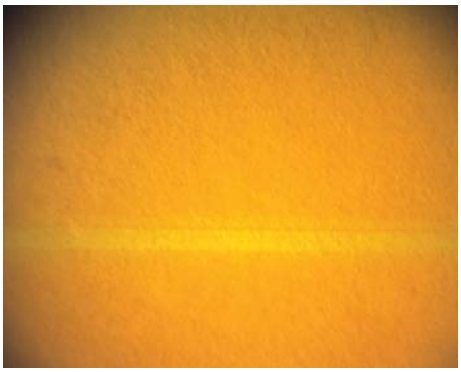


(b) Actual setup used for bleaching waveguides.

Figure 6.8 – The experimental setup used to photo-bleach waveguides in BAF-1 doped films.



(a) A 7 μm waveguide formed in a 7 μm thick PMMA film doped with 3wt% PYR-3.



(b) A 20 μm waveguide formed in a 7 μm thick PMMA film doped with 3wt% BAF-1.

Figure 6.9 – Microscope pictures of photo-bleached waveguides.

calculated by adding the refractive index induced by dye doping (Δn) to the base refractive index of the undoped polymer ($n_{polymer}$). The refractive index induced by doping, $\Delta n\left(\omega^{'}\right)$, can be estimated by the Kramers-Kronig transform (equation 6.1) of the absorption coefficient change ($\Delta\alpha\left(\omega\right)$), where c is the speed of light, λ is the incident wavelength, ω is the angular frequency ($2\pi c/\lambda$) and $\Delta n\left(\omega^{'}\right)$ is the change in the real component of the refractive index at angular frequency $\omega^{'}$ [131].

The base refractive index of the undoped polymer (non-absorbing medium) can be estimated by the Sellmeier equation (equation 6.2), where B_i and C_i are the Sellmeier coefficients ($B_1 = 0.99654$ and $C_1 = 7.870\times10^{-15}$ m^2, $B_2 = 0.18964$ and $C_2 = 2.191\times10^{-14}$ m^2, $B_3 = 0.00441$ and $C_3 = 3.857\times10^{-12}$ m^2 for PMMA [132] and $B_1 = 1.3654$ and $C_1 = 1.4\times10^{-14}$ m^2 for APC [45]).

$$\Delta n\left(\omega^{'}\right) = \frac{c}{\pi}\int_0^{\infty}\frac{\Delta\alpha\left(\omega\right)}{\omega^2-\omega^{'2}}d\omega \tag{6.1}$$

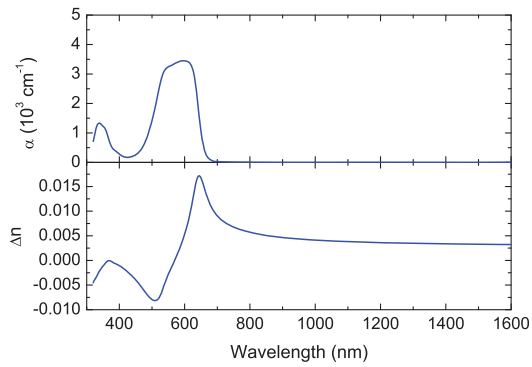
$$n^2\left(\lambda\right) = 1+\sum_{i=1}^{3}\frac{B_{i\lambda^2}}{\lambda^2-C_i} \tag{6.2}$$

The expected refractive indices for dye-doped films of PYR-3/PMMA (Fig 6.10), PYR-3/APC (Fig 6.11) and BAF-1/PMMA (Fig 6.12) were calculated and compared with refractive index measurements made with the Metricon 2012. The PYR-3/PMMA expected refractive index was considerably lower than the measured values and could be due to the dye's aggregation or interaction with the PMMA; a study of dye loading weights and comparison to other doped polymers might reveal a possible explanation. The PYR-3/APC expected refractive index was in good agreement with the measured values and the BAF-1/PMMA expected refractive index was broadly in line with the actual values. The absorption coefficient plots for the PYR-3 doped polymers show the main peak contains a shoulder on the left as part of the peak due to dye aggregation[¶]. This effect becomes more pronounced as dye loading concentration increases [118]. No shoulder indicating aggregation was observed with the BAF-1 dye which could be attributed the ethylhexyl groups on the fluorene preventing the dye molecules from stacking [45].

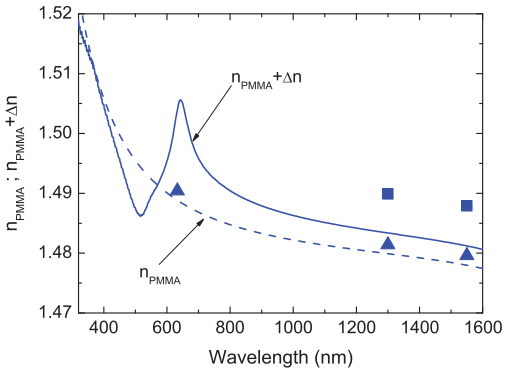
6.3.3 Bragg grating writing

Bragg gratings were inscribed into waveguides using phase masks, as these allowed reproducible gratings that would be in the range of the broadband light source and detector. The masks had a period of 1045 nm for PMMA films and 1000 nm for APC films. The inscribed Bragg grating had a period that is half that of the

[¶]As bleaching progresses the shoulder on the main peak due to aggregation disappears as dye concentration is reduced. Dye aggregation occurs when dye molecules stack on each other head to tail, cancelling out the overall effective dipole.

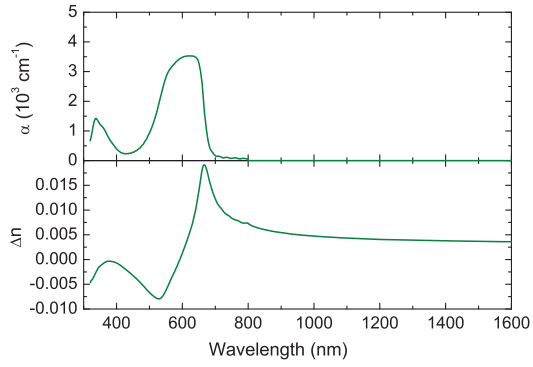


(a) The change in refractive index induced by the dye (bottom) calculated using the Kramer-Kronig transform of the absorption coefficient (top).

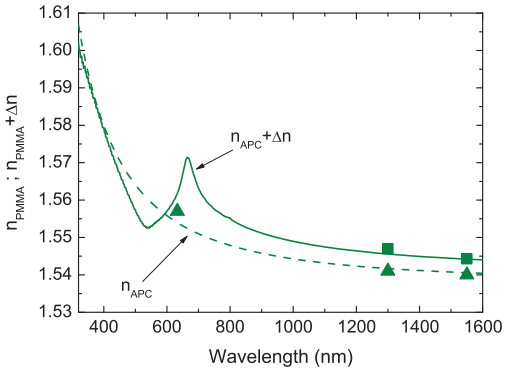


(b) The calculated refractive index for a doped (solid line) and undoped (dashed line) film with doped (■) and undoped (▲) measured values.

Figure 6.10 – Effect of doping for a 7 μm thick 3wt% PYR-3/PMMA film.

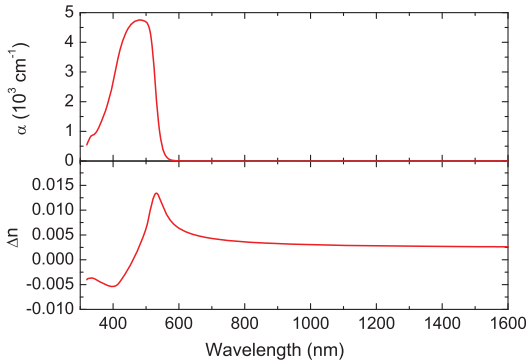


(a) The change in refractive index induced by the dye (bottom) calculated using the Kramer-Kronig transform of the absorption coefficient (top).

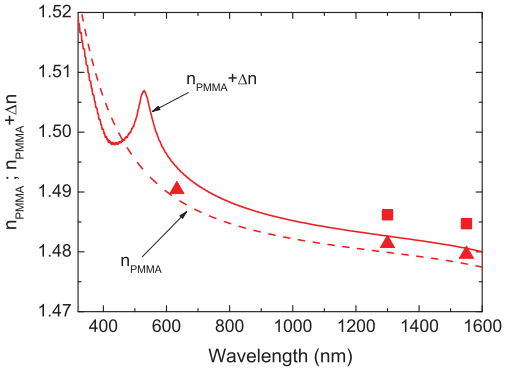


(b) The calculated refractive index for a doped (solid line) and undoped (dashed line) film with doped (■) and undoped (▲) measured values.

Figure 6.11 – Effect of doping for a 7 μm thick 3wt% PYR-3/APC film.



(a) The change in refractive index induced by the dye (bottom) calculated using the Kramer-Kronig transform of the absorption coefficient (top).



(b) The calculated refractive index for a doped (solid line) and undoped (dashed line) film with doped (■) and undoped (▲) measured values.

Figure 6.12 – Effect of doping for a 7 μm thick 3wt% BAF-1/PMMA film.

phase mask used, regardless of the wavelength of light used to write the grating [133, 134]. A critical step of the fabrication of the sensor involves the precise alignment of the phase mask while writing; where only slight variations in the alignment can effect the grating spectra significantly. A single peak will only occur when the incident beam is perfectly normal with respect to the film [135]. If the phase mask was misaligned by up to 5° a tilted grating will be written where two Bragg reflection peaks will be observed, one from the core mode and the other from the ghost mode [31].

Alignment was achieved by aligning the waveguide with the phase mask and tightening the phase mask holder so the film was held firmly against the mask. The reflection of the incident light from the phase mask surface was then guided back along its own path by adjusting tilt and rotation of the phase mask holder (Fig 6.13). The 488 nm line from an Ar ion laser was used to write the gratings, the 1 mm beam was expanded to 10 mm using 30 mm and 300 mm focal point lens in a beam expander configuration, with irises used to maintain the spatial quality of the beam (Fig 6.14). The choice of a 10 mm beam size was arbitrary as much smaller gratings can achieve 99% reflectance due to the much larger expected refractive index difference of dye-doped Bragg gratings compared to gratings formed in silica [136]. Bragg gratings in PYR-3 doped films were written with a power of 20 mW for 30 minutes. The BAF-1 doped films were written with a power of 60 mW for 5 hours with a waveplate included to prevent dye alignment.

In addition to the remaining photo-products some of the dye can break down and out-gas from the polymer during bleaching, creating a thickness reduction of up to hundreds of nanometers generating small surface relief effects [130]. After the completion of waveguide and grating writing the final cladding layer was spin coated in order to avoid any distortion effects caused by the layer during

waveguide bleaching and grating writing. The oven drying of this layer should also remove any small surface relief effects.

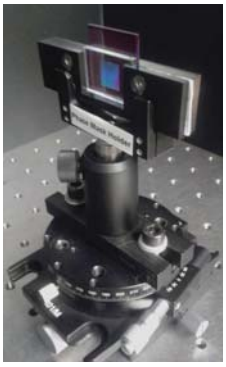


Figure 6.13 – Phase mask holder with tilt and rotation capability.

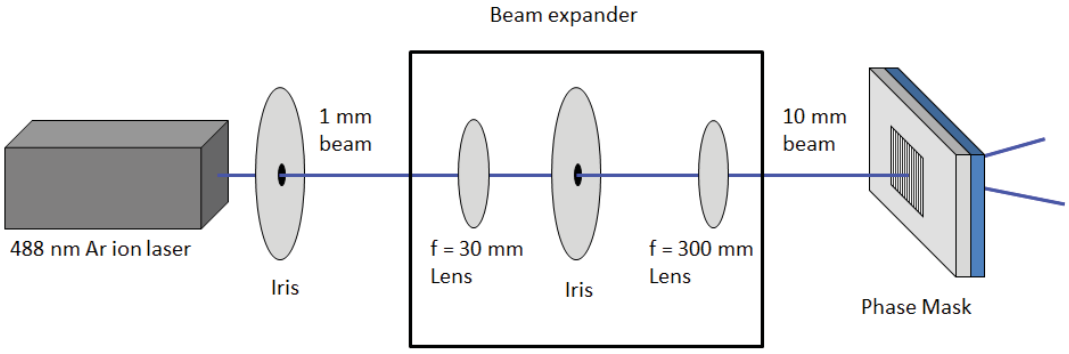
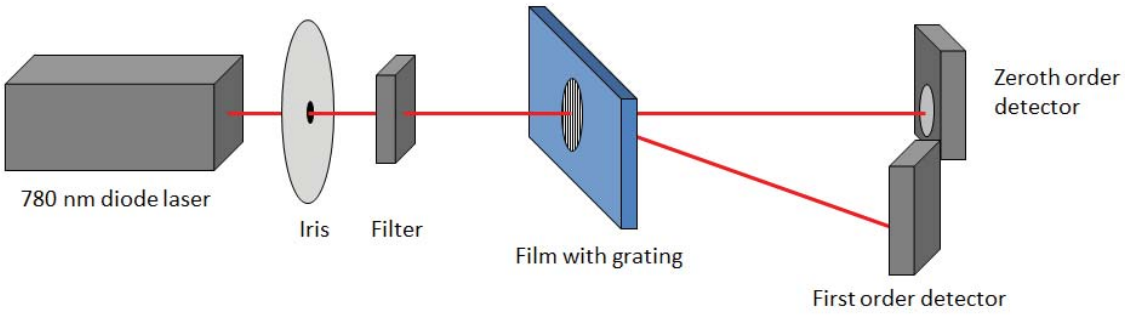


Figure 6.14 – Setup used to write Bragg gratings in dye-doped films.

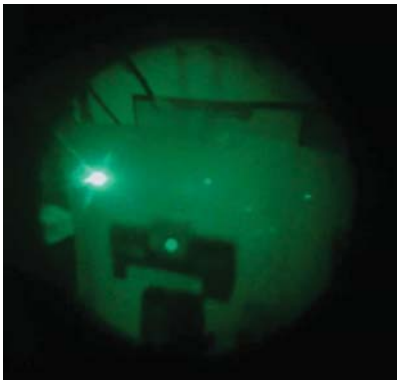
Bragg grating efficiency

The efficiency of the grating written needs to be determined in order to maximise the Bragg reflection intensity. A method to do this is to treat the grating as a thin transmission diffraction grating, where the spacing of the modulations become the period of the grating [45]. By illumination with a probe laser and recording the intensity of the diffracted orders the diffraction efficiency can be determined. This is a proxy measure of the refractive index difference induced during writing and is directly linked to the Bragg reflectivity [19, 45, 137].

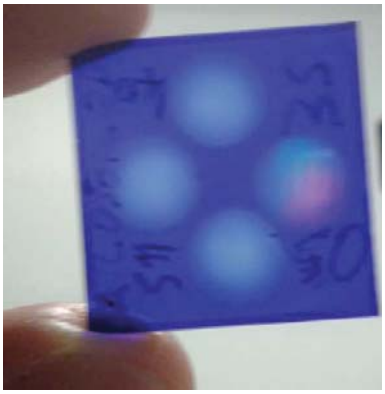
As a phase mask was used, a probe beam to determine diffraction efficiency cannot be used during writing as the diffracted orders overlap. Instead a set of gratings were written with different durations using the same writing conditions and probed separately with a 780 nm diode laser. A 780 nm narrow pass filter was used to remove any non 780 nm light produced by the diode laser that might be in the absorption band of the dye (Figs 6.15 & 6.16). Bragg gratings



(a) Schematic of 780 nm probe beam setup.



(b) Diffracted orders seen through a camera that could see 780 nm light.



(c) A Bragg grating diffracting room light to form a rainbow like pattern.

Figure 6.15 – Dye-doped film used as a diffraction grating.

written in PMMA films had a modulation spacing of 552.5 nm and were probed at an angle of 50° with the first diffracted order observed at 43.5° (the first diffracted order was observed at 50° for APC films with a modulation spacing of 500 nm) (Fig 6.17). The efficiency modulates during inscription due to the multiple processes occurring during bleaching [138] with the maximum diffraction efficiency of 0.12% achieved after writing for 30 minutes; this was the duration used when writing 3wt% PYR-3 doped gratings.

A better method to determine the optimum writing time is to write the grating in situ to a waveguide that has already been coupled to a fibre, and monitoring the Bragg reflection evolution.

Phase masks are specially designed to have most of the diffracted laser light in the first diffracted orders ($\geq$90%) with a high zeroth order suppression. In practice there was still a small amount of undiffracted light (about 5%) that causes an interference pattern with the first diffracted orders and writes a grating with the same period as the phase mask. This weak grating will cause a Bragg grating with a reflection that is outside the range of the 1550 nm broadband light source.

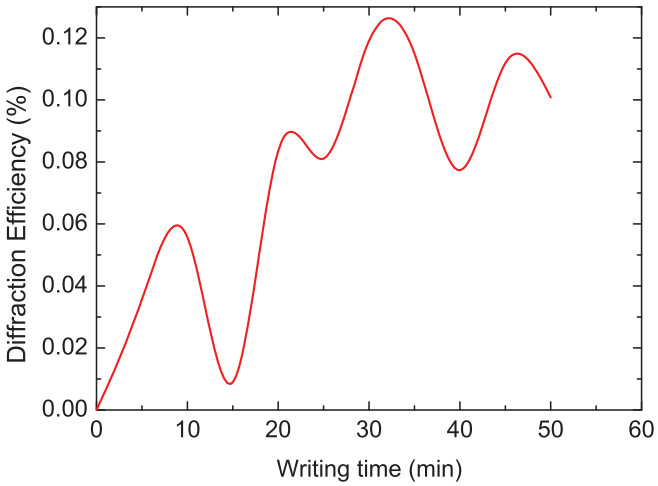


Figure 6.16 – Diffraction efficiency with time of a Bragg grating in a 3wt% PYR-3 doped PMMA film written with a 30 mW 488 nm laser using a 780 nm probe beam.

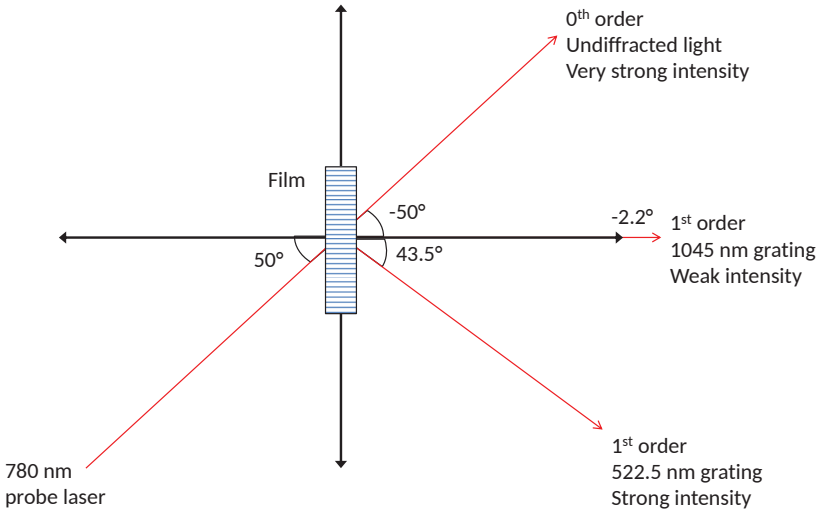


Figure 6.17 – Schematic of the diffraction seen from a grating written in a 3wt% PYR-3 doped PMMA film.

6.3.4 Coupling

Coupling the dye-doped film to optical components to allow it to be used as a sensor was the most challenging aspect of this research. This section gives extensive details on how this was achieved. Butt coupling with a single-mode silica fibre was the preferred coupling method, the input light was single-mode and allowed for easy connection to other optical components (Fig 6.18). It also gave the sensor the mobility that was needed, freeing it from the optical table that other coupling methods required.

The input optical fibre used was an FC/APC fibre patch cable that was cut in half and a portion of the coating stripped with a Miller dual hole optical fiber stripper (FO 103-D-250), before being polished with lapping paper using an 8°** angled puck (D50-FC/APC) (Fig 6.19a). After marking the location of the Bragg grating on the film, it was removed from the glass substrate and cut at an angle of 8° using a razor from a polymer fibre cleaver set (Fig 6.19b). This enabled the fibre and film to be coupled to each other (Fig 6.19c).

The optical fibre was held by a fibre clamp (SM1F1-250) that was threaded into a rotational mount, allowing the fibre to be rotated along the axis of the fibre. This fibre launch mount was connected to an XYZ-movement stage, giving the input fibre some coarse movement. The film was attached to a glass housing unit, consisting of a microscope slide and two thin glass spacer strips between which the films was housed (Fig 6.5). The lower glass strip was glued and cured to the microscope slide using a UV curable glue and uncured glue was used between the film and the spacer strips. The UV curable glues used were the medium viscosity glues NOA 68 (n=1.540) and NOA 148 (n=1.480) from Norland. NOA 148 suffered from oxygen inhibition so was more difficult to cure and was only used for single cladded films where the glue refractive index was important. Medium viscosity glue was preferred as the low viscosity glue would form a thin layer on the microscope slide without immersing the fibre. Conversely, high viscosity glue would cause a very slow responses to changes in fibre position making coupling challenging.

The film was positioned so that it was protruding out from the spacer strips by a very small amount. This keeps the film as level as possible for optical fibre coupling as the films had a tendency to curl and roll up. The film and its glass mount was placed on a piece of white card so that a microscope with a digital camera attachment could be used for assisting coupling. A desktop lamp with a low heat light bulb†† was used for illumination, as heat can disrupt the alignment. The position of the film was controlled by a micro-positioning stage (NBM413/M), which gave precise control of y and z movement as well as pitch and yaw. The x movement, the distance of the fibre from the film, was controlled by the fibre launch stage. A 1550 nm broadband light source and an optical

**The 8° angle was used to reduce back reflections from the broadband light.

††Alternatively an LED could be used for illumination.

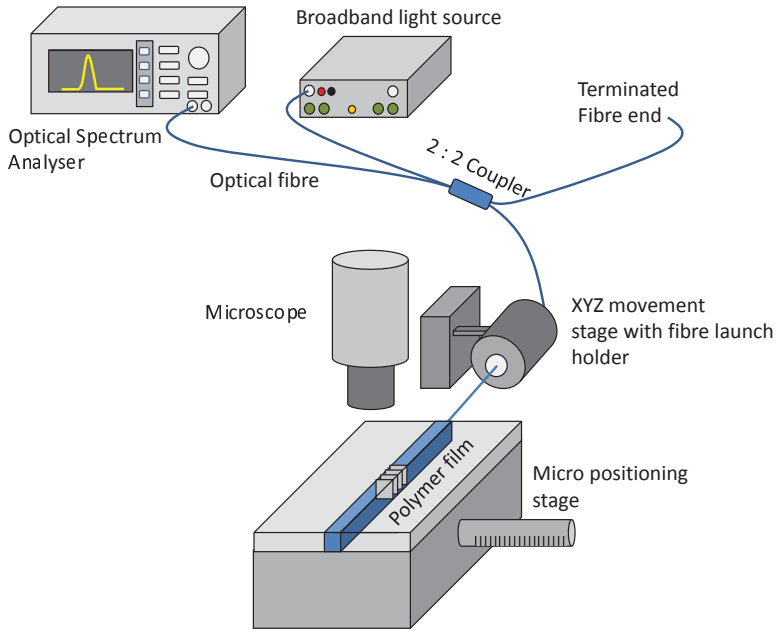


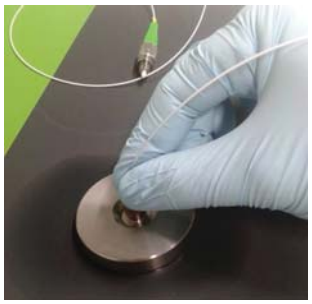
Figure 6.18 – Coupling setup used to attach a single-mode silica fibre to a dye-doped polymer film.

spectrum analyser were connected to the fibre using a 2:2 coupler. This meant that one end had to be terminated. The optical spectrum analyser was preferred as it was much more sensitive than the interrogator. However, the interrogator could be used with strong Bragg reflections after coupling.

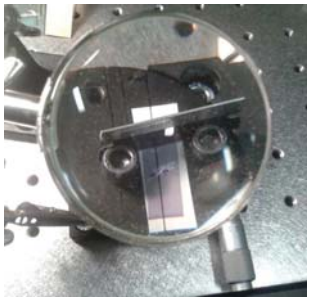
The general procedure used for coupling was to first check the back reflection of the polished fibre; if a high back reflection was observed the fibre was re-polished. Then using the microscope camera the optical fibre, polished at an angle of 8°, was rotated so that the 8° was horizontal. This allows the film and fibre to fit together at an 8° angle (Fig 6.19c). An initial rough alignment was done by hand where the mounted film was placed on the stage and lined up with the coupling fibre. A small bead of UV curable glue was placed on the end of the fibre using a stick dipped in glue (Fig 6.20). This was to prevent an air gap interference pattern from the 1550 nm light as the fibre approached the film. The 1550 nm broadband source was replaced with a 860 nm broadband light source, which is visible to the microscope camera, aiding with fibre and waveguide alignment. It was possible to see guided light coming out the other end of the waveguide when aligned properly. The 1550 nm source was then reintroduced and fine adjustments made with the micro-positioning stage until a Bragg reflection was observed.

If no reflection was observed then the 860 nm source was reconnected and the process repeated a number of times. If still no reflection was observed then the film could either be re-cleaved with a razor or replaced with another film. The lack of a Bragg reflection could be due to insufficient waveguide bleaching[‡‡],

[‡‡]Due to insufficient refractive index difference between the waveguide and its cladding to



(a) Silica fibre polished at an 8° angle.



(b) Film cut with a razor at an 8° angle.



(c) Fibre and film butt coupled together at an 8° angle.

Figure 6.19 – Preparing the fibre to couple with the dye-doped waveguide.

misalignment during phase mask writing or poor coupling. Occasionally the fibre was polished poorly and also needed to be replaced. This could be checked by examining the beam quality of the light coming out the fibre using an IR card. Once a small Bragg reflection was observed fine micro-positioning stage adjustments could be made to maximise the Bragg reflection. A 365 nm LED was used to precision cure the small bead of UV curable glue. At this stage a LED was used instead of a Black-Ray UV lamp to prevent misalignment from heat. After initial curing the fibre and the area near the spacer glass was immersed in glue and piecewise curing is continued with the LED (Fig 6.21). Fine adjustments with the micro-positioning stage were required during curing as glue shrinkage would occur moving the fibre. As the glue cured it became more viscous and slower fine adjustments were needed. This method can suffer large losses due to misalignment during curing. The final cure can be done with a 100 W 365 nm Black-Ray UV lamp before the sensor is left overnight to allow the glue to mostly cure - full cure occurs over a week from UV exposure [139].

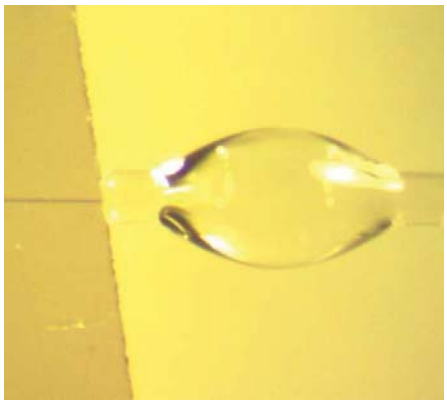
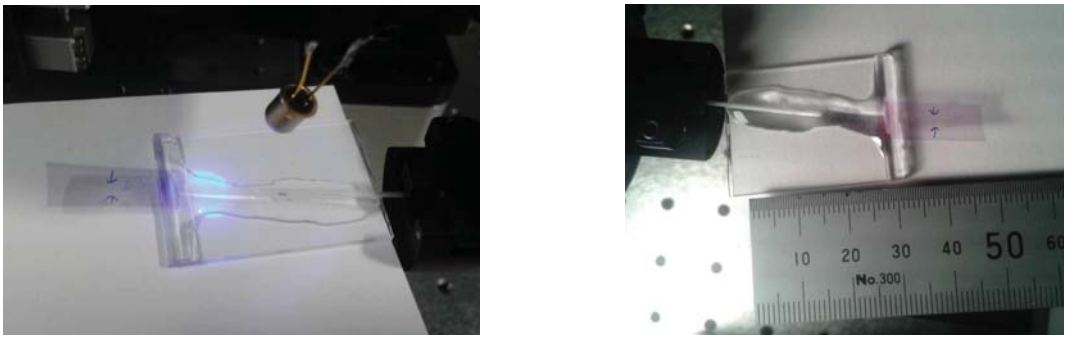


Figure 6.20 – An optical fibre coupled to a waveguide with a bead of UV curable glue.

support light modes.



(a) Glue securing the fibre to the film undergoing curing with a UV LED.

(b) The film sensors small size makes it an attractive niche sensor.

Figure 6.21 – A PYR-3 doped film coupled to an optical fibre. The arrows mark the position of the Bragg grating.

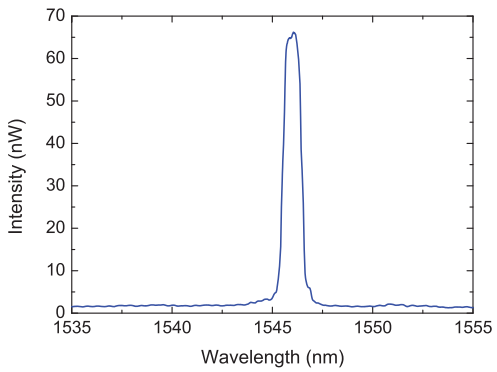
6.3.5 Bragg reflections

Bragg reflections were observed in PMMA films doped with PYR-3 and BAF-1 and an APC film doped with PYR-3. A single-mode Bragg reflection was observed in a 3wt% PYR-3 doped PMMA film with a single-mode waveguide (7 $\times$ 7 μm) with two PMMA cladding layers (Fig 6.22) with a peak at 1546 nm and a full width half maximum (FWHM) of 1 nm (much larger than the typical 0.1 nm seen with FWHM silica FBGs). The FWHM is much larger than silica fibre based Bragg reflections due to the much larger refractive index difference induced by doping (equation 2.13).

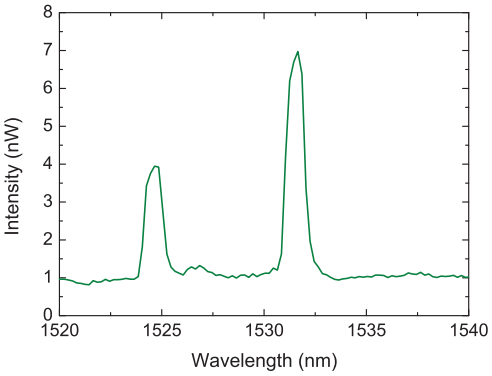
A multi-mode Bragg reflection was observed in a 3wt% BAF-1 doped PMMA film with a multi-mode waveguide (20 $\times$ 7 μm) with a single PMMA cladding layer (Fig 6.23a). Additional peaks are due to photo-switching (Fig 6.23b) which occurs when the dye switches from cis-trans isomers due to the absorption of light around a particular band (around 530 nm for BAF-1), with some switching naturally occurring due to thermal effects [140, 141]. There are two portions of the dye that is photo-switchable allowing trans-trans, trans-cis (as the dye is symmetrical the two trans-cis states are the same) and cis-cis configurations. Each of these configurations induce a different refractive index difference in the polymer and a different corresponding Bragg reflection. The central Bragg reflection is located at 1545.570 nm with an estimated FWHM of 0.540 nm using peak fitting program.

A double peak Bragg reflection, characteristic of a tilted grating written due to phase mask misalignment [31, 135], was observed for a 3wt% PYR-3 doped APC film with a single-mode waveguide (7 $\times$ 7 μm) with a single PMMA cladding layer (Fig 6.22b). The central Bragg reflection is located at 1531.650 nm with a FWHM of 0.950 nm.

Multiple Bragg reflection peaks were seen for a 3wt% PYR-3 doped PMMA film with a multi-mode waveguide (30 $\times$ 7 μm) with no claddings (Fig 6.24).

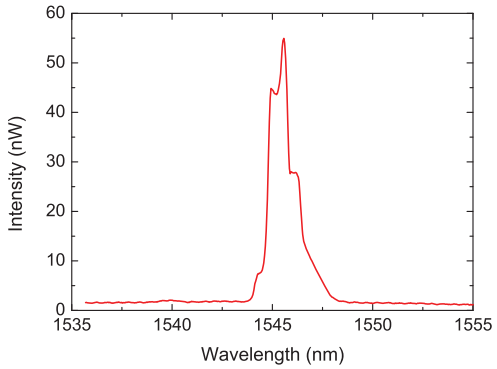


(a) Bragg reflection of a 3wt% PYR-3 doped PMMA film with a single-mode 7×7 μm waveguide with two PMMA cladding layers.

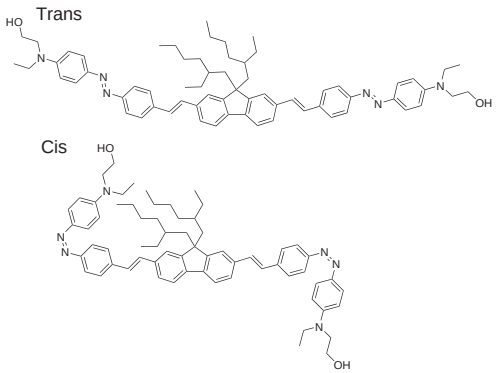


(b) Bragg reflection of a 3wt% PYR-3 doped APC film with a single-mode 7×7 μm waveguide with one PMMA cladding layer.

Figure 6.22 – Bragg reflections observed in PYR-3 doped polymers.



(a) Bragg reflections of a 3wt% BAF-1 doped PMMA film with a multi-mode 20×7 μm waveguide with one PMMA cladding layer.



(b) The BAF-1 dye undergoing photo-switching between its cis and trans states.

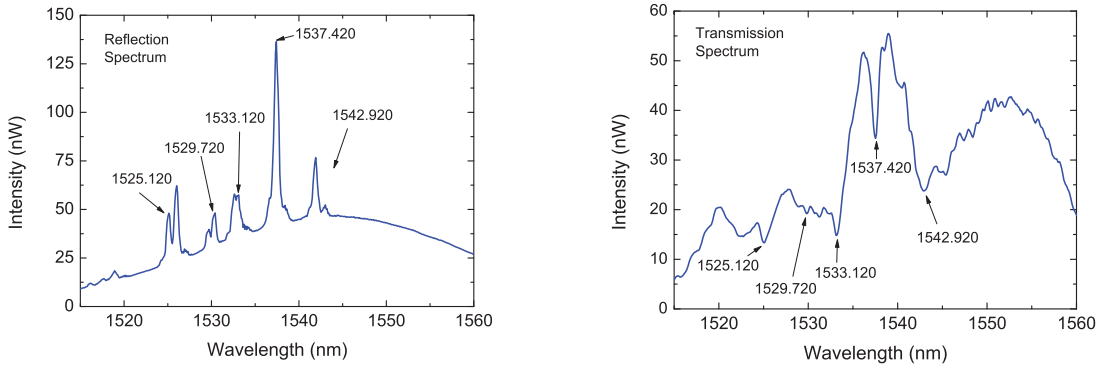
Figure 6.23 – Bragg reflection observed in BAF-1 doped PMMA.

Different modes were able to be excited by moving the input fibre, resulting in different Bragg reflections being observed. A small amount of the broadband light was seen in the reflection spectrum which could be removed by better polishing of the input fibre.

Film shrinkage

The observed Bragg reflections are at a different wavelength than expected given the refractive index of the film and phase mask period[§§]. Here a set of calculations is done that provide evidence of film shrinkage upon removal from the glass

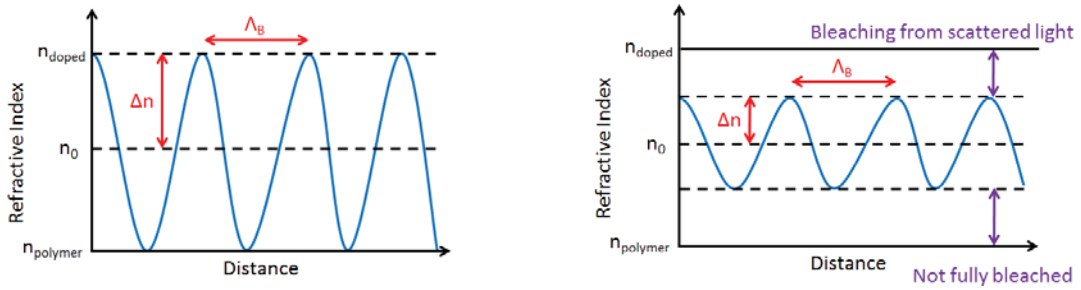
[§§]The manufacturer error for the phase mask period is ± 0.1 nm, leading to a refractive index error range of 0.0003. This alone can not explain the Bragg wavelength shift.



(a) Reflection spectrum.

(b) Transmission spectrum.

Figure 6.24 – Bragg grating in a 3wt% PYR-3 doped PMMA film with a multimode 30 × 7 μm waveguide with no claddings.



(a) Perfect grating profile with unbleached portions of the doped refractive index and bleached portions of the polymer refractive index.

(b) Actual grating profile with scattered light causing additional undesired bleaching and unbleached dye remaining.

Figure 6.25 – Bleaching profile of a Bragg grating in a dye-doped film.

substrate as a possible explanation.

The expected Bragg reflection peak (λ_B Expected) can be calculated using the expected spacing of the modulations (Λ_B Expected), simply half the phase mask modulations Λ_{PM} ($\Lambda_B = \Lambda_{PM}/2$), and the expected effective refractive index[¶¶] (n_e Expected). The expected effective refractive index is estimated as the mid-point between the the doped and undoped polymer refractive indices[***].

Using the observed Bragg reflection peak (λ_B Observed) and the expected spacing of the modulations (Λ_B Expected), simply half the phase mask modulations Λ_{PM} ($\Lambda_B = \Lambda_{PM}/2$), the observed effective refractive index (n_e Observed) can be determined ($\lambda_B = 2n_e\Lambda_B$) (Table 6.1). This effective refractive index is unphysical as it is below the refractive index of the plain undoped polymer (Table 6.2). In a perfect case the Bragg grating written would have a perfect profile of refractive index modulations ranging between the fully doped to fully bleached refractive index (Δn Expected) (Fig 6.25a). However, in reality there will be some light scattering causing additional bleaching and some remaining dye in the bleached areas, leading to a smaller refractive index modulation (Δn Observed) (Fig 6.25b).

Table 6.1 – Parameters of the dye-doped polymer Bragg reflection.

Dye/Polymer	PYR-3/PMMA	PYR-3/APC	BAF-1/PMMA
Λ_{PM} (nm)	1045	1000	1045
Λ_B Expected (nm)	522.50	500.00	522.50
Λ_B Observed (nm)	520.85	469.60	521.06
λ_B Expected (nm)	1550.885	1542.150	1549.840
λ_B Observed (nm)	1546.000	1531.650	1545.570
n_e Expected	1.4841	1.5422	1.4831
n_e Observed	1.4794	1.5317	1.4790
Δn Expected	0.0041	0.0022	0.0031
Δn Observed	0.0019	0.0019	0.0010
FWHM Expected (nm)	2.140	1.070	1.620
FWHM Observed (nm)	1.000	0.950	0.540
Grating length, l (mm)	10	10	10

The observed refractive index modulation (Δn Observed) can be calculated from the observed FWHM (FWHM Observed) using equation 6.3, where S[†††] is 1, n_0 is the average refractive index ($n_0 = n_{eff}$) and N is the number of grating planes ($N = \frac{l}{\Lambda_B}$, where l is the grating length - 19,138 planes for PMMA and

[¶¶]This is reasonable as in practice the real film effective refractive index should be quite close to the expected.

[***]This could be slightly higher due to the small increase in refractive index from residual photo-products.

[†††]S is a factor which is 1 for strong gratings (near 100% reflection) or 0.5 for weak gratings.

Table 6.2 – Refractive index data for 3wt% dye-doped films measured using a Metricon 2010 at 1550 nm.

Dye/Polymer	PYR-3/PMMA	PYR-3/APC	BAF-1/PMMA
n_{plain} (undoped polymer)	1.4800	1.5400	1.4800
n_{doped}	1.4882	1.5443	1.4862
n_0	1.4841	1.5422	1.4831
Doping effect	0.0082	0.0043	0.0062

20,000 for APC based films) [1].

The reflectivity at the Bragg reflection peak can be calculated using equation 6.4, where γ is equal to κ the coupling coefficient (equations 6.5 & 6.6) as there is no wave vector detuning ($\Delta\beta = 0$) [20]. This was calculated for the dye-doped films (Table 6.3) with a large reflectivity (greater than 95%) achieved for 0.5 mm gratings, this is a distinguishing feature of dye-doped Bragg gratings. For comparison silica fibre based Bragg gratings have a much lower induced refractive index modulation, a typical optical fibre Bragg grating (core index = 1.47, cladding index = 1.457, $\lambda_B = 1550$ nm and $\Delta n_{eff} = 1 \times 10^{-4}$) the grating length required for greater than 95% reflectivity exceeds 10 mm [20].

The expected FWHM (FWHM Expected) can be calculated using the expected induced refractive index difference (Δn Expected) and compared to the actual FWHM (FWHM Actual). This was smaller than the calculated value due to the smaller refractive index difference induced in practice (Δn Observed)[‡‡‡].

$$FWHM = \lambda_B S \sqrt{\left(\frac{\Delta n}{2n_0}\right)^2 + \left(\frac{1}{N}\right)^2} \tag{6.3}$$

$$R(L, \lambda) = tanh^2(\gamma L) \tag{6.4}$$

$$\kappa = \frac{\pi \Delta n_{eff}}{\lambda} \tag{6.5}$$

$$\gamma = \sqrt{\kappa^2 - \Delta\beta^2} = \kappa \tag{6.6}$$

The observed modulation spacing (Λ_B Observed) can be determined by using the observed Bragg reflection and the expected effective refractive index. The observed modulation spacings are smaller than the expected modulation spacing and can be explained by the film contracting once it was removed from the glass substrate. When the film was spin coated the solvent evaporated, shrinking the film and leaving it in a strained state on the glass. The Bragg grating was then

[‡‡‡]Even at 3wt% dye loading, the induced refractive index difference was significantly higher than that observed with silica fibre. It can be made to exceed the induced refractive index difference of PMMA fibre by increasing the dye loading (Table 2.1).

Table 6.3 – Calculated reflectivity at 1550 nm of the 3wt% dye-doped polymer films.

Grating length (mm)	PYR-3/PMMA reflectivity (%)	PYR-3/APC reflectivity (%)	BAF-1/PMMA reflectivity (%)
0.05	15.46	4.60	9.25
0.07	27.45	8.76	17.10
0.10	46.38	16.82	31.01
0.15	71.79	32.96	54.22
0.20	86.58	49.30	72.27
0.30	97.30	74.58	91.19
0.40	99.48	88.47	97.41
0.50	99.90	95.01	99.26
1.00	100.00	99.93	100.00
10.00	100.00	100.00	100.00

written on the strained film with the expected modulation spacing. The film was subsequently removed from the glass and contracted to give the smaller unstrained observed modulation spacings.

This shrinkage can be estimated by calculating the change in modulation spacing ($\Delta\Lambda_B = \Lambda_B$ Observed - Λ_B Expected) and applying the change across the 10 mm grating to find the change in grating length Δl ($\Delta l = \Delta\Lambda_B$ N). This can then be scaled to estimate the shrinkage across the whole 25 mm film. The shrinkage across the whole film was calculated as 79 μm (0.31%) for the PYR-3/PMMA film, 170 μm (0.68%) for the PYR-3/APC film and 69 μm (0.28%) for the BAF-1/PMMA film. Although this shrinkage was very small, any slight change in the modulation spacing can cause an appreciable change in the Bragg reflection peak position. The greatest shrinkage occurs for the APC film and could explain why APC films are particularly prone to peeling off the substrate and curling, as they are under the greatest stress.

6.3.6 Summary and future work

In summary, waveguides and Bragg gratings were written in PYR-3/PMMA, BAF-1/PMMA and PYR-3/APC dye-doped films with Bragg reflections observed. A method was developed for the preparation and coupling of the films with a single-mode fibre - where the phase mask and input fibre alignment were found to be critical steps. Single Bragg reflections were only observed in a single-mode waveguide after using correct phase mask alignment with a non photo-switchable dye, otherwise multiple peaks were observed. The Bragg reflection peak was observed at a shorter wavelength than expected after writing with a phase mask. This was attributed to the film being strained by shrinkage occurring during drying after spin coating, which was released once the film was removed from the

substrate.

Future work has a wealth of possible directions. It could extend the work done here such as reducing the coupling loss from misalignment during curing, writing Bragg gratings in-situ to optimise the reflection or trying smaller length gratings to allow the fabrication of multiple Bragg gratings in a much smaller space than conventional silica fibre. Other directions include trialling alternative dyes, such as poled electro-optic or tethered dyes that could have an enhanced sensitivity due to a higher strain optic coefficient [142], or more exotic waveguide and multiple grating configurations featuring rosettes for strain tensor determination or temperature compensation.

Chapter 7

Planar dye-doped polymer Bragg grating sensor

7.1 Introduction

Bragg gratings have been inscribed in glass [1], plain polymer [93, 109] and dye-doped polymer fibre [112]. Each of these methods rely on photosensitivity, where light is used to induce a physical mechanism resulting in a permanent refractive index change. Originally observed in glass, Bragg gratings were written in photosensitive Germanium-doped silica fibre where UV light triggered permanent structural changes via the formation of Germanium-silica wrong bonds. Since then a range of other dopants have been shown to exhibit photosensitivity, with refractive index modulations of upto 10^{-3} achieved [1]. Using ultra-short pulse lasers Bragg gratings have recently been demonstrated in undoped silica [143].

There has been a rise of polymer optical fibres (POFs) that have become a cheap short distance fibre used extensively in consumer products. Traditionally these fibres are PMMA, which has been shown to be photosensitive to UV light. The mechanism of photosensitivity in polymers is via ablation - where light damages the material through the build up of heat in a small area, bond breaking - where the polymer chain is broken up by the light making the polymer a lower molecular weight, photopolymerisation - where the light initiates polymerisation of unreacted monomers and cross linking - where light causes nearby polymer chains to form a link with each other[6, 93, 109].

Polymer fibre can also be made to be photosensitive by doping it with a dye. The addition of a dye increase the refractive index, which can be subsequent lowered by degrading the dye using light in the dyes absorption band. This enables the refractive index contrast to be controlled by the loading of the dye dopant with much larger refractive index modulations of 10^{-2} possible. This method allows the formation of waveguides and sensing elements like Bragg gratings and micro-rings [112, 144].

This chapter presents the basic concepts and experimental results of the dye-

doped polymer film sensors, developed in the previous chapter, being used as strain, temperature and chemical sensors. The chapter is separated into three main themes of dye-doped polymer films as humidity and temperature sensors, chemical sensors and strain sensors, with a basic concepts and results given for each theme. Here 2,4-dinitrotoluene (DNT) is focused on in the chemical sensing theme, although humidity sensing is strictly a form of chemical sensing (the detection of water vapour) it is treated in a separate section as it is a critical consideration when conducting temperature measurements.

7.2 Basic concepts

7.2.1 Dye-doped polymer films as humidity and temperature sensors

Dye-doped polymer film sensors can be used as humidity and temperature sensors, where the sensing element is the Bragg grating that is formed in the dye-doped waveguide. As a humidity sensor this operates in a similar way as to a polymer coated glass optical fibre Bragg gratings - water enters the polymer causing swelling and straining the underlying Bragg grating, and is sensed by the increasing the period of the Bragg grating modulations. Unlike the coated optical fibre the insensitive glass fibre is removed so that water can enter the entire sensor - including the waveguide (Fig 7.1). When water enters the waveguide it causes a refractive index increase that enhances the Bragg reflection shift. This enhancement is further increased when a dye is used as the water changes the local electric field of the dye and by doing so the refractive index.

These factors mean that a dye-doped polymer film sensor should be significantly more responsive to humidity than an analogous polymer coated glass optical fibre. There should also be an enhancement in the sensor's time response to a humidity step change, as water can diffuse from both above and below the free-standing film.

This diffusion can be modelled using a modified two layer model, similar to the model introduced in chapter 5, except that the time constants now represent different regions. The key differences are that the inner layer contains the waveguide and that diffusion can occur from above and below, as it is not bound by the impermeable optical fibre.

As a temperature sensor the film acts in a similar way as glass and polymer fibre Bragg gratings. In response to a temperature increase there are two effects that shift the Bragg wavelength ($\Delta\lambda_B$), a thermal expansion of material represented by the coefficient of thermal expansion, α_Λ, and a change in refractive index with temperature represented by the thermo-optic coefficient, α_n (equation 7.1). When using a dye-doped polymer there is an additional contribution within the thermo-optic coefficient from the dye, this should give it an enhanced response over undoped polymer sensors. For PMMA-based sensors there is a

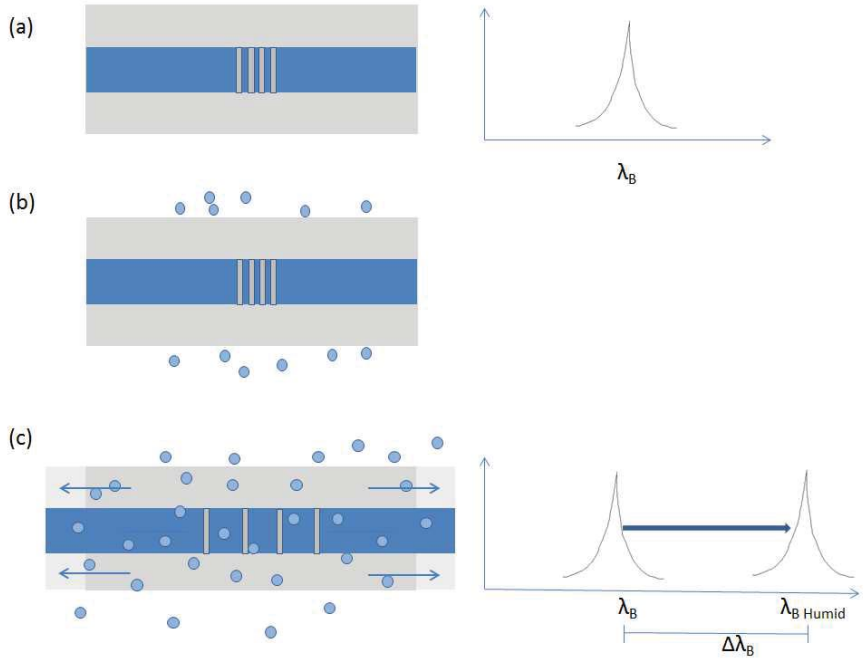


Figure 7.1 – The dye-doped film Bragg grating senses humidity by both the polymer swelling with moisture, straining the underlying Bragg grating, and the water entering the waveguide, causing a refractive index change. This process is illustrated by (a) a film sensor in dry conditions with a dry Bragg reflection wavelength of λ_B, then (b) the film is exposed to moisture and (c) the moisture is absorbed by the film, straining the Bragg grating and entering the waveguide, shifting the Bragg reflection wavelength to $\lambda_{B\ Humid}$. The film core is expanded for clarity and is not to scale.

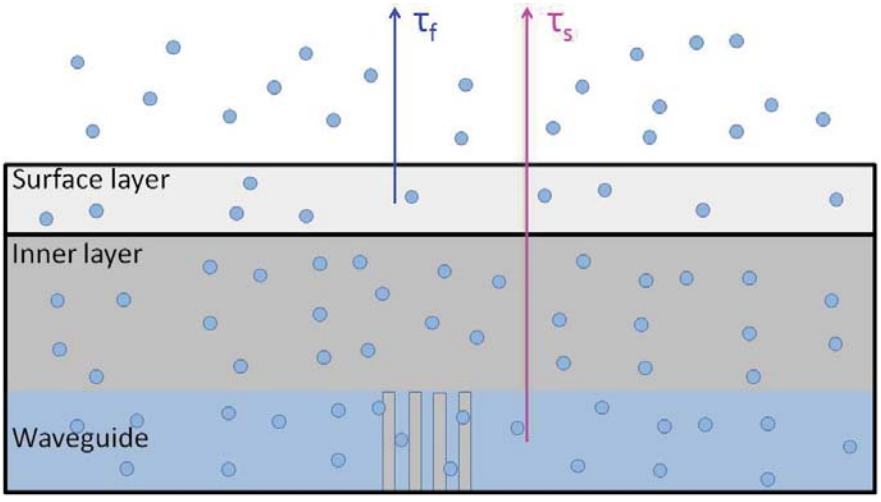


Figure 7.2 – A two layer model with the film divided into a surface layer with a fast time constant, τ_f, and a inner layer with a slow time constant, τ_s. As it is a film there will be a continuation of the inner layer and another surface layer below. An important feature is the waveguide and Bragg grating is included in the inner layer.

characteristic shift to shorter Bragg reflection peak wavelength with increasing temperature [145].

$$\Delta\lambda_B = \lambda_B \left(\alpha_\Lambda + \alpha_n\right) \Delta T \tag{7.1}$$

7.2.2 Dye-doped films as chemical sensors

By utilising the dye the film sensor can be used as a chemical sensor to detect the vapour of a highly polarised chemical species, such as an explosive. The non-explosive and volatile species 2,4-dinitrotoluene (DNT) is analogous to the well known explosive trinitrotoluene (TNT). The mechanism of detection involves the nitroaromatic species associating with the dye and changing the local electric field environment of the dye, modifying its absorption spectrum and refractive index [144]. A possible mechanism for DNT associating with the dye PYR-3 is proposed in Fig 7.3. Here the DNT and dye associate due to their dipole charges, with the additional possibility of π-π interactions.

Water is also a highly polarised molecule, that is much smaller and more mobile than DNT. This could lead to it competing with DNT to associate with the dye, interfering with DNT sensing. Studies on highly dye-doped (20wt%) PMMA have shown that on exposure to DNT the dye's absorption spectra shifts to shorter wavelength generating a refractive index change of up to 0.012 [144, 146]. If this refractive index change occurred to a dye-doped film sensor it would generate a Bragg reflection peak shift of 12 nm to longer wavelength. This result can be scaled back for a 3wt% doped film to give an estimated shift of 2 nm to longer wavelength.

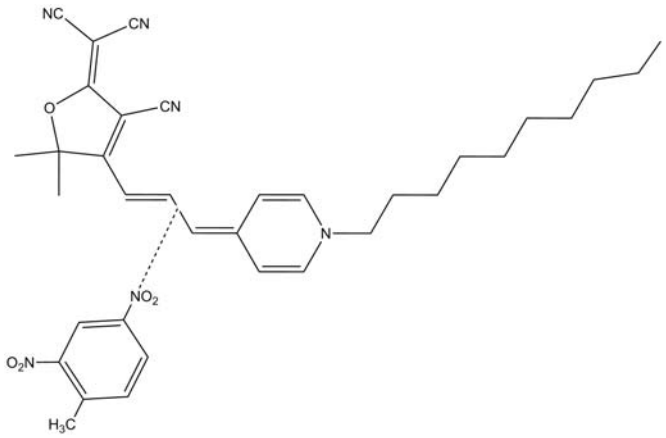


Figure 7.3 – The nitroaromatic species DNT associating with the II-bridge of the zwitterionic dye PYR-3.

7.2.3 Dye-doped polymer films as strain sensors

Bragg grating sensors are ideally suited for sensing strain. Here strain induces two changes, both the grating period (Λ_B) and a refractive index change ($\partial n/\partial l$),

causing a shift in the Bragg reflection peak (λ_B). Dye-doped film sensors work in the same way, except that the refractive index change can be enhanced by using a polarised dye, giving greater sensitivity to strain.

There are many ways to conduct a strain calibration experiment, including adhering the film to a tensile strain bar and straining it, adhering the film to a micrometer stage and moving the film a known amount or by hanging free weights off the film. Attaching the film to a tensile bar proved challenging as the film was under an extreme angle resulting in light being decoupled from the waveguide, together with a high risk of the film tearing. To be effectively mounted to the tensile bar a larger film would need to be made, requiring larger than 25 × 25 mm glass substrates. Using a micrometer stage to extend the film presents the challenge of accurately measuring the extension where less than a micron extensions typically occur. Any slippage with the glue would significantly increase the error associated with the measurement. For these reasons using free weights was the preferred method of straining the film. By simply hanging a known weight off the film the strain imparted to the film can be accurately measured by knowing the cross sectional area of the film (Fig 7.4). As no glue is used there is no risk of slippage and the film feels the full force of the weight.

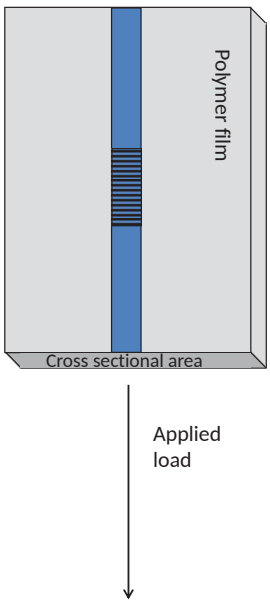


Figure 7.4 – Schematic of the dye-doped film sensor and the applied load.

Using free weights the sensitivity of the sensor can be determined by the slope of a linear plot of Bragg wavelength shift $\Delta\lambda_B$ with applied tensile strain ε. A free weight can be converted into a tensile stress σ by determining its applied force F ($F = mg$ where m is the mass of the free weight and g is acceleration due to gravity) over the cross sectional area A of the film (equation 7.2). The tensile stress can be converted into a tensile strain by dividing by the polymer's Young's

modulus E (equation 7.3).

$$\sigma = \frac{F}{A} \tag{7.2}$$

$$\varepsilon = \frac{\sigma}{E} \tag{7.3}$$

To separate the contributions due to the change in period and the change in refractive index the elongation can be calculated to determine the change in period contribution (equation 7.4).

$$\varepsilon = \frac{\partial l}{l} \tag{7.4}$$

Here l is the length of the Bragg grating and ∂l is the elongation which is assumed to be evenly spread across the entire grating. The grating period extension $\partial\Lambda_B$ can be estimated by considering the extended grating length ($l+\partial l$) and dividing this by the number of grating planes N ($N = l/\Lambda_B$). The extended grating period $\Lambda_{B\ extended}$ can be determined by considering the elongated grating length ($\Lambda_{B\ extended} = (l + \partial l)/N$), allowing the change in period to be calculated ($\partial\Lambda_B = \Lambda_{B\ extended} - \Lambda_B$). The change in period with change in length ($\partial\Lambda_B/\partial l$) is found by dividing by the change in length.

By considering the Bragg wavelength shift and strain of a free weight (the maximum weight for example), the change in refractive index with change in grating length ($\partial n_{eff}/\partial$ l) can be estimated using equation 7.5 [54].

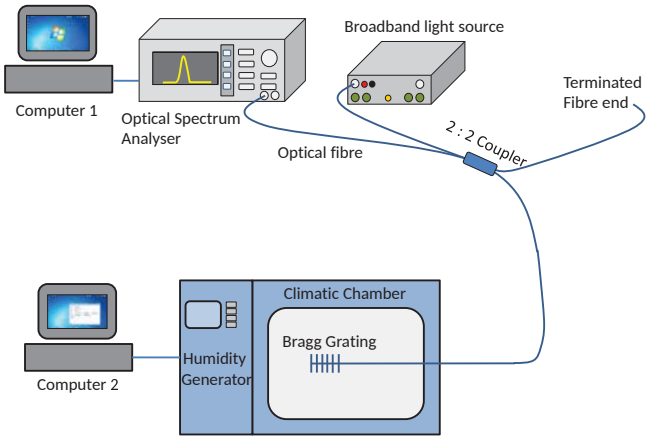
$$\Delta\lambda_B = 2\left(\Lambda_B\frac{\partial n_{eff}}{\partial l} + n_{eff}\frac{\partial\Lambda_B}{\partial l}\right)\Delta l \tag{7.5}$$

7.3 Humidity and temperature response of doped film sensors

7.3.1 Experimental setup

Humidity and temperature measurements were carried out in a calibration chamber designed to minimise temperature gradients and fluctuations. The calibration chamber used was a Thunder Scientific Model 2500 humidity generator with a temperature controlled jacket and was used for automatic generation of relative humidity in the range from 12 %rh to 95 %rh. A smaller container was used in the calibration chamber to reduce the size of the atmosphere to better control the climate (Fig 7.5b). A broadband 1550 nm light source from Southern Photonics was the preferred light source as it was more powerful than the interrogators in built source.

A high sensitivity optical spectrum analyser (OSA) (MS9740A) from Anritsu Corporation was used to observe the Bragg reflection peak. The film sensor coupled to a single-mode FC/APC fibre was linked to the broadband light source and



(a) Schematic of setup.



(b) The insides of the calibration chamber where the sensor was housed in a smaller chamber for more accurate results.

Figure 7.5 – Experimental setup used to investigate the humidity and temperature response of the dye-doped film sensors.

optical spectrum analyser via a 2:2 coupler with FC/APC connectors (Fig 7.5). As the OSA has a FC/PC connector port an additional patch cable with FC/PC and FC/APC connectors was used, this would cause additional light losses. The calibration chamber was linked to a computer with auto profile software allowing the duration of each humidity and temperature step to be automated. A computer linked to the OSA with a labview program was used to track the Bragg reflection peak.

For calibration measurements the chamber was kept at a constant temperature and an auto profile cycle consisting of dry to humid steps of 12, 20, 30, 40, 50, 60, 70, 80, 90 and 95 %rh and the reverse humid to dry steps to return to the dry 12 %rh start was used. The chamber was left for two hours for equilibration from ambient conditions or when a temperature change occurred to the first dry step, then held at each step for an hour. If multiple cycles were investigated the second and subsequent cycles would commence immediately after the completion of the previous cycle. For humidity time response measurements the chamber was left for an hour for equilibration from ambient conditions to the driest humidity setting before commencing 30 minute cycles between dry (5 %rh) and wet (95 %rh) air flows.

7.3.2 Humidity and temperature response

Humidity response

The humidity response of a 27 μm thick 3wt% PYR-3/PMMA film with two undoped PMMA claddings was investigated with a calibration chamber (Fig 7.6 and Table 7.1). A linear humidity response of 57.5 pm/%rh was observed for the humidity range 12 to 60 %rh. This was a slightly larger response than sim-

ilar undoped PMMA based FBG sensors reported in the literature. A humidity response of 42 pm/%rh (35 to 85 %rh range) was reported for a 1.1 mm thick planar PMMA sensor [109] and responses of 33.6 pm/%rh (30 to 90 %rh range) [93] and 35.2 pm/%rh (50 to 95 %rh range) [145] were reported for PMMA polymer optical fibre sensors. For these sensors water vapour can enter the entire sensor, including the waveguide, causing a refractive index change that is additional to the refractive index change induced from the strain alone. The larger humidity response of the dye-doped sensor could be due to the water vapour interacting with the dye in the waveguide, changing the dye molecule's electronic environment, leading to an enhanced refractive index change. The polymer film based sensors above have a significant increase in humidity response when compared to coating traditional glass fibre Bragg gratings with polymer coatings, where a modest 0.97 pm/%rh (12 to 60 %rh range) response was observed for a 50 μm PMMA coating.

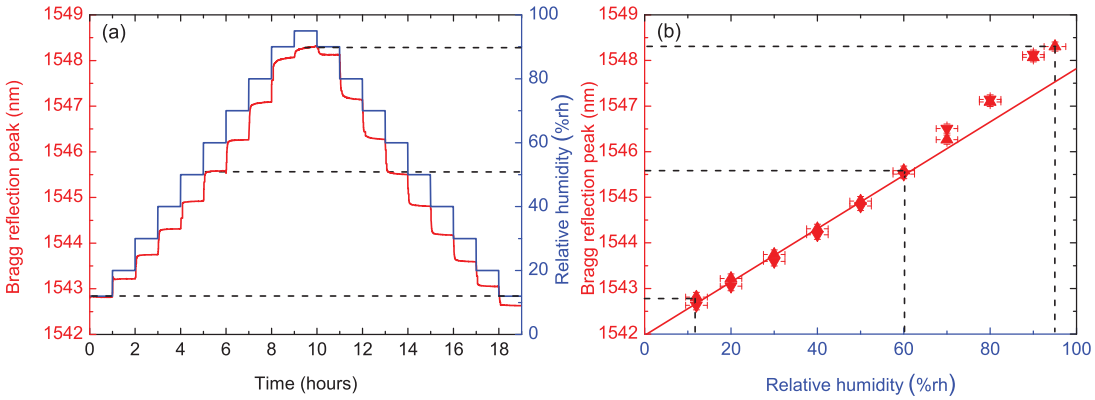


Figure 7.6 – A 3wt% PYR-3/PMMA film of 27 μm thickness (two undoped PMMA claddings) had its (a) humidity response at 21 °C investigated with the (b) stable wavelength value at each humidity plotted.

Table 7.1 – Dye-doped film humidity response.

Dye / Polymer	Thickness (μm)	Waveguide dimensions (μm)	Humidity response[a] (pm/%rh)
PYR-3 / PMMA	27	7 × 7	57.5
PYR-3 / PMMA	17	7 × 7	44.6
BAF-1 / PMMA	17	7 × 20	62.1

[a]Only the linear portion below 70 %rh was used for the response.

In Fig 7.6a a slower time response to a higher relative humidity change and non-linear deviation above 60 %rh was observed, this can be attributed to the formation of water clusters [65]. A small amount of hysteresis was observed for the cycle with the decreasing humidity values being of shorter wavelength, and could be due to solvent being expelled or the polymer relaxing.

The power of the Bragg reflection peak was monitored during the humidity

cycle (Fig 7.7). A loss of power was observed with increasing humidity, that was reversible upon decreasing humidity with the power returning to its original level. The change in power is caused by the glue used to secure the optical fibre to the film being affected by humidity changes, swelling and shifting the alignment of the coupled fibre.

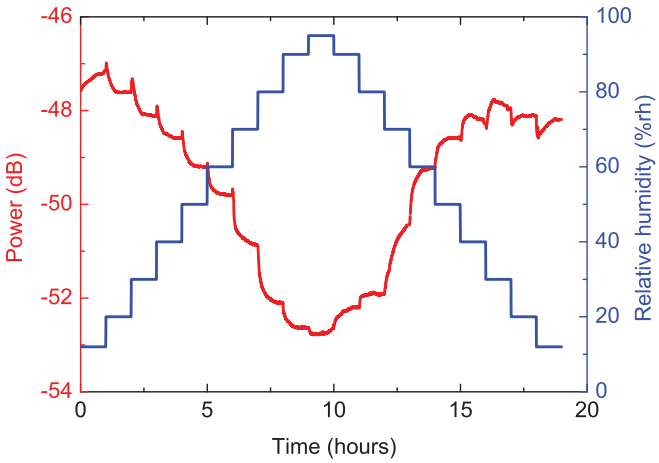


Figure 7.7 – Bragg reflection peak power changing with humidity for a 3wt% PYR-3/PMMA film of 27 μm thickness (2 undoped PMMA claddings).

The effect of multiple humidity cycles was investigated for a 3wt% PYR-3/PMMA film of 17 μm thickness with a single undoped PMMA cladding (Fig 7.8 and Table 7.1). A linear humidity response of 44.6 pm/%rh (12 to 60 %rh) was observed, which is slightly lower than the double cladded film sensor.

This decrease in response may be due to the film thickness decrease or different bleaching occurring during waveguide writing and Bragg grating inscription. The latter occurs due to different light scattering during writing for each film. Here excessive bleaching would cause a lower refractive index contrast and less dye for the water to associate with, leading to a reduced response. An investigation of different thickness films and using different dye loadings might reveal a trend. As the cycles progress hysteresis is observed with a shift to shorter wavelength (Fig 7.8b). This can also be attributed to solvent being expelled or the polymer settling in.

The humidity response of a 17 μm thick 3wt% BAF-1/PMMA film with one undoped PMMA cladding was investigated with a calibration chamber (Fig 7.9 and Table 7.1). A linear humidity response of 62.1 pm/%rh was observed for the humidity range 12 to 60 %rh. This was a larger response than the 3wt% PYR-3/PMMA film sensor of the same thickness. This indicates that the enhancement of the humidity response could be due to the different dye being used. Aside from the enhanced response, the same characteristics as the PYR-3 doped films are observed. A slower time response to a higher relative humidity change, non-linear deviation above 60 %rh and a small amount of hysteresis were observed.

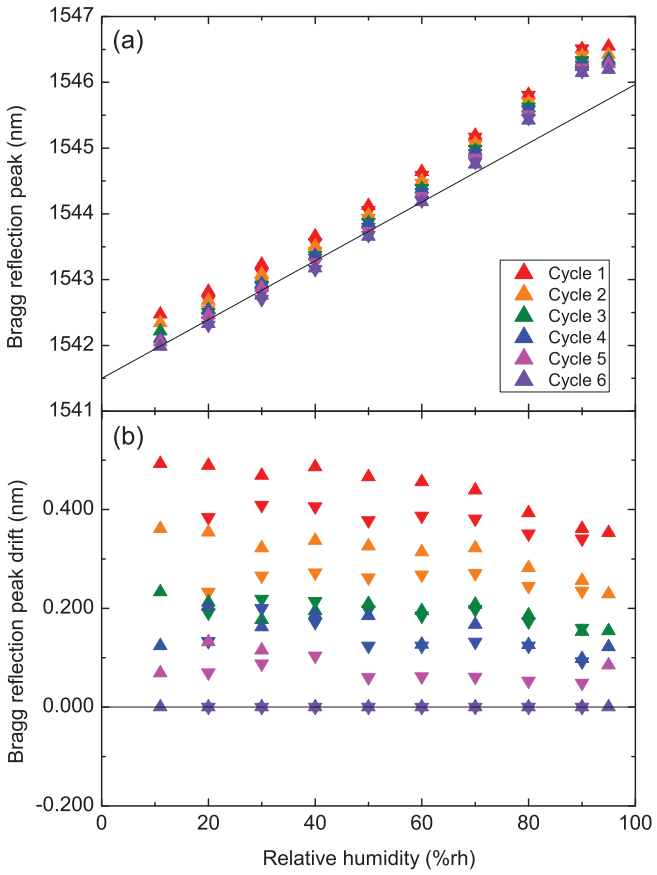


Figure 7.8 – A 3wt% PYR-3/PMMA film of 17μm thickness (1 undoped PMMA cladding) was exposed to 6 humidity cycles at 21 °C with its (a) stable wavelength value at each humidity and (b) difference from the final cycle (cycle 6) plotted. The lines are a guide to the eye.

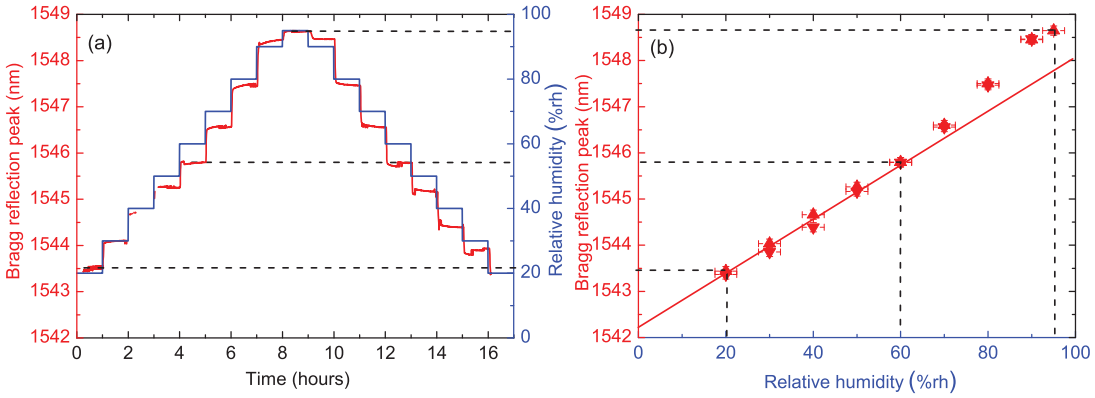


Figure 7.9 – A 3wt% BAF-1/PMMA film of 17 μm thickness (one undoped PMMA cladding) had its (a) humidity response at 21 °C investigated with the (b) stable wavelength value at each humidity plotted. The lines are a guide to the eye.

Time response

The time response to a humidity step change (5 to 95 %rh and vice versa) was investigated for 17 μm thick 3wt% PYR-3 and BAF-1/PMMA film sensors (Fig 7.10 and Tables 7.2 & 7.3). The two layer model gave similar effective time constants for both water absorption (3.8 and 3.6 minutes) and desorption (9.3 and 10.5 minutes) for the PYR-3 and BAF-1 doped films respectively. This follows the expected trend for PMMA based sensors where the water absorption is faster than desorption. The 17 μm thick films can be compared to a 50 μm coating of the same PMMA on an silica optical fibre. This shows the films have significantly faster effective time responses for both absorption and desorption.

This can be attributed to the films having a smaller thickness than the coating and the ability of the film to diffuse from two sides, unlike the coated optical fibre that was bounded on one side by an impermeable glass core.

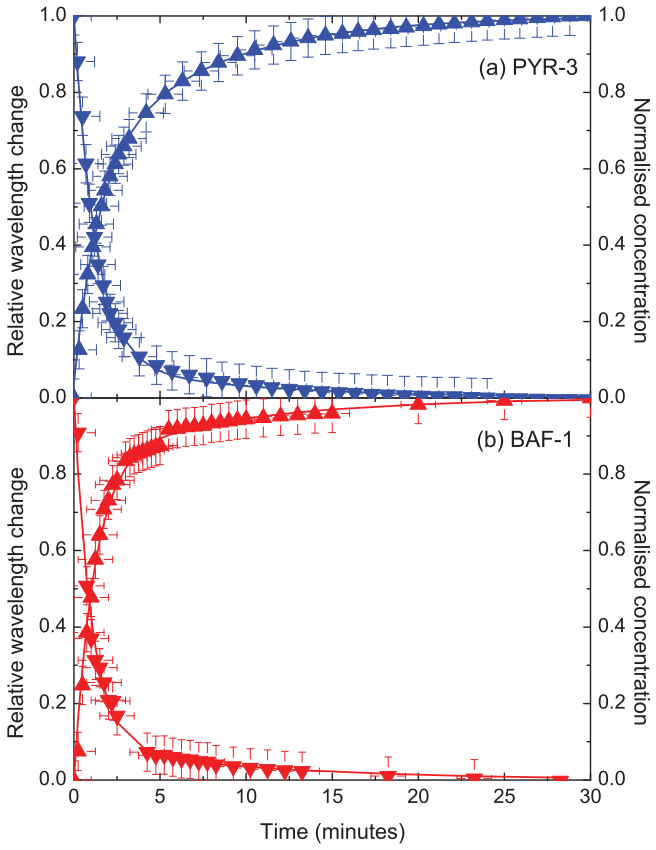


Figure 7.10 – Time response to a humidity step change (5 - 95 %rh and vice versa) for 17 μm thick films of (a) 3wt% PYR-3/PMMA and (b) 3wt% BAF-1/PMMA.

Polymer optical fibres can achieve a large humidity response but can come at a cost of a slow time response, a 150 μm diameter PMMA fibre has a response time of 53 minutes for a 80 to 70 %rh step change at 25 °C [93]. Dye-doped films offer an attractive alternative, having a large humidity response and an extremely

Table 7.2 – Table of water absorption parameters.

Dye / Polymer	Thickness (μm)	w_f weighting	τ_f (min)	w_s weighting	τ_s (min)	$\tau_{effective}$ (min)
PMMA[a]	50	0.50	3.2	0.50	9.5	6.3
PYR-3	17	0.59	1.4	0.41	7.1	3.8
BAF-1	17	0.83	1.3	0.17	15.4	3.6

[a]Polymer coated silica FBG for comparison only.

Table 7.3 – Table of water desorption parameters.

Dye / Polymer	Thickness (μm)	w_f weighting	τ_f (min)	w_s weighting	τ_s (min)	$\tau_{effective}$ (min)
PMMA[a]	50	0.50	1.9	0.50	5.6	3.7
PYR-3	17	0.91	1.3	0.09	9.3	2.0
BAF-1	17	0.91	1.0	0.09	10.5	1.9

[a]Polymer coated silica FBG for comparison only.

fast time response.

In chapter 5 a mesh model was used in combination with the two-layer model to fit time response data. However, the mesh model was unable to provide a satisfactory fit to the data in Fig 7.10. This could be due to the model using a very basic diffusion equation that did not account for the refractive index change induced by water being in the waveguide, and a more sophisticated model would be required.

Temperature response

The temperature response of a 17 μm thick 3wt% PYR-3/PMMA film sensor was determined by a set of temperature controlled humidity cycles (Fig 7.11). The Bragg reflection peak wavelength for the 10 °C and 21 °C cycles were identical with shifts to shorter wavelength that become larger as temperature increases (Fig 7.11b).

A large contribution of this shift to shorter wavelength comes from:

- The refractive index difference change with temperature represented by the thermo-optic coefficient, α_n, which is *negative* for PMMA (-1.2×10^{-4} [23]).

- The minor thermal expansion coefficient, α_Λ, contribution which is *positive* for PMMA (7.0×10^{-5} [23]), causes a shift to longer wavelength. This effect is overwhelmed by thermo-optic coefficient contribution.

Additional small wavelength contributions could be due to:

- Remaining solvent being removed during the temperature cycles.

- Dye migration occurring that reduces the effective refractive index.
- Voids in the polymer being filled with unraveling polymer chains.

All of these effects would become more pronounced at higher temperature and could account for the larger shifts seen at higher temperature.

The time response to a humidity step change becomes slower at higher temperature and relative humidities. During the 50 °C and 60 °C cycles the sensor does not equilibrate within the hour before the next humidity step occurs. This data required a mathematical fit to estimate the stable values for Fig 7.11b.

During the 60 °C cycle the glue became mobile and allowed the coupled optical fibre to move. This was a critical failure of the sensor, although the glue was rated to 80 °C the alignment was severely affected at 60 °C, resulting in a permanent loss of signal. A possible solution to this problem would be to trial a high temperature optical glue (such as NOA83H which is rated to 150 °C) and to coat the cured glue with an impermeable layer to give to resistance to humidity changes - preserving the alignment of the fibre. This will enable the sensor to measure temperatures up to 105 °C, the glass transition temperature of PMMA as the dye PYR-3 is thermally stable up to 289 °C.

No hysteresis was observed for the 10 to 30 °C cycles, with hysteresis appearing at 40 °C becoming more severe as temperature increases. This could be due to the slower time response observed at higher temperature and could be explored by conducting multiple higher temperature humidity cycles with humidity holding times of greater than an hour.

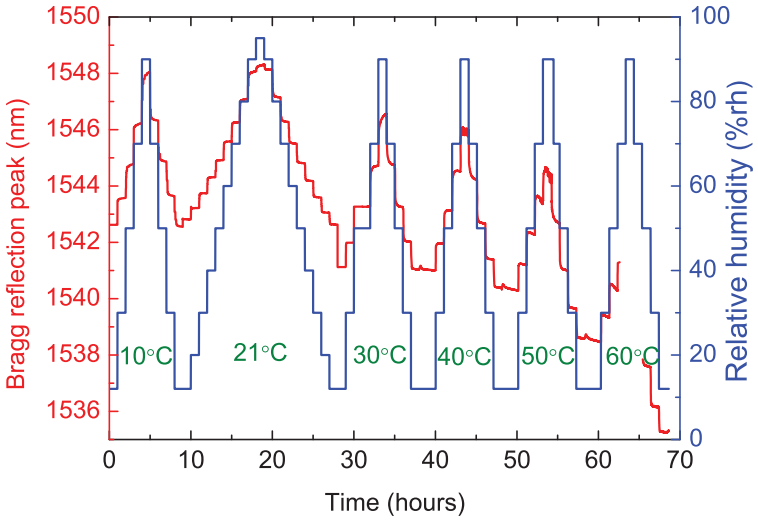
Unfortunately, the repeatability could not be tested because of the sensor failure.

7.4 Chemical response of doped polymer film sensor

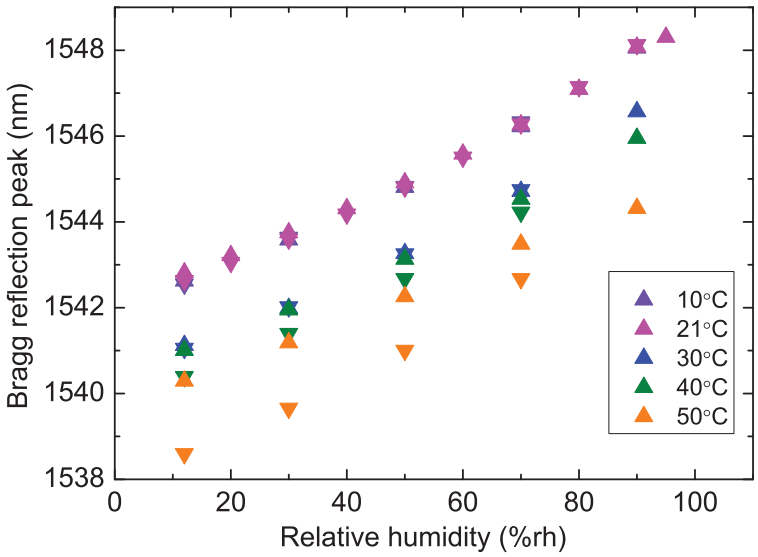
7.4.1 Experimental setup

Two experiments were conducted to observe the effects of DNT exposure. The first experiment has a chamber with a lid that could be opened to add or remove DNT while the second experiment has a closed chamber to greatly reduce the effects of room humidity.

In first experiment the film was sealed in a chamber with lids (Fig 7.12). From previous work it is known that the film sensors are highly responsive to humidity; as such, humidity must be carefully controlled. The humidity in the chamber was stabilised by filling the chamber with silica beads, assisted by a



(a) Cycles of temperature and humidity.



(b) Stable values at each temperature and humidity.

Figure 7.11 – Temperature and humidity response of a 17 μm thick (one cladding) 3wt% PYR-3/PMMA film sensor.

pre-purge with dry air from a two-flow humidity generator where air exits via a bubbler. The film's fibre connector exits the chamber from a glass side tube with a rigorous para-film seal and was connected to a 1550 nm broadband light source and OSA via a 2:2 coupler. The temperature of the chamber was monitored by an external pico technology PT-104 data logger temperature probe attached to the outside of the chamber with insulation wool wrapped around the setup to minimise temperature fluctuations (Fig 7.12b).

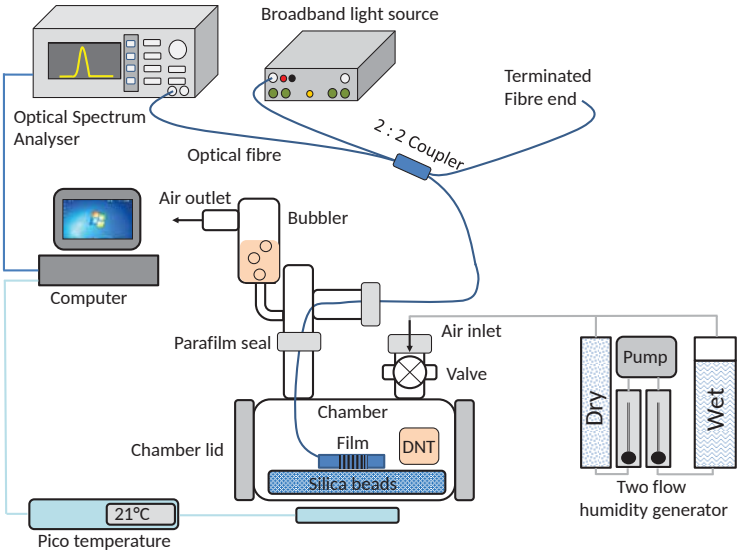
The chamber was left to equilibrate for an hour with a dry air pre-purge running, then the valve was closed and the purge stopped and left for another hour before starting measurements. The chamber's base Bragg reflection peak reading was recorded for two hours before opening the chamber and inserting and removing DNT at hourly intervals.

The second experiment was designed to minimise the effect of humidity fluctuations. Here two chambers, one containing the film sensor and the other the DNT, are separated a valve (Fig 7.13). The film chamber has a side port where the Centre 313 humidity and temperature probe was housed. The chamber was filled with silica beads to minimise humidity fluctuations with the openings rigorously sealed with para-film. A pico technology PT-104 data logger temperature probe was attached to the outside of the chamber with insulation wool wrapped around the entire setup. The DNT chamber was also filled with silca beads and packed lightly with cotton wool to keep the DNT and silica beads separate. The film's fibre connector was connected to a 1550 nm broadband light source and OSA via a 2:2 coupler and the OSA, Centre 313 probe and PT-104 were linked to a computer with software to record the Bragg peak, humidity and temperature.

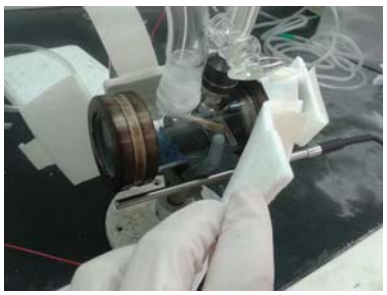
The chamber was left for 24 hours to allow the humidity in the chamber to stabilise, after which the valve was opened to release DNT vapour into the film chamber. After an hour of DNT exposure the DNT was heated intensively with a heat gun for 5 minutes to fill the film chamber with a high concentration of vapour.

7.4.2 DNT response

The room temperature vapour concentration of DNT is 100 to 120 ppb [144] which is significantly lower than the water vapour concentration 7,500 ppm for 50 %rh at 21 °C (typical lab conditions), this concentration is reduced to 3,000 ppm for 20 %rh. Previous experiments have shown the critical role humidity plays with a response of 44.6 pm/%rh observed for the 17 μm thick film (one cladding) of 3wt% PYR-3/PMMA film sensor used in the DNT sensing experiments. One PMMA cladding was used to allow the DNT better access to the dye in the Bragg grating. Before use the DNT was stored with silica to remove water taken up by the DNT. All experiments done in a fume hood with proper PPE (as it was unsafe to use the humidity calibration chamber), although DNT is not explosive it is highly toxic. Here the results for the single chamber and dual chamber experiments are

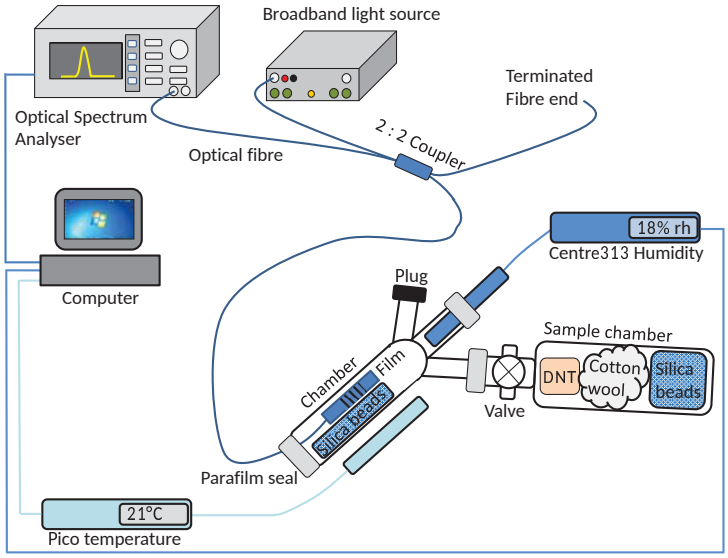


(a) Schematic of the single chamber setup.



(b) Single chamber during an experiment.

Figure 7.12 – The first chemical sensing experiment where a 17 μm thick film (one cladding) of 3wt% PYR-3/PMMA film sensor was exposed to DNT in a single chamber.



(a) Schematic of the dual chamber setup.



(b) Dual chamber during an experiment.

Figure 7.13 – The second chemical sensing experiment where a 17 μm thick film (one cladding) of 3wt% PYR-3/PMMA film sensor was exposed to DNT using a dual chamber.

presented.

Single chamber results

The film sensor was exposed to DNT in a single humidity controlled chamber by opening the chamber with hourly cycles of inserting and removing the DNT (Fig 7.14). An initial stable baseline Bragg wavelength was achieved after leaving the chamber to dry for 24 hours. When the chamber was opened a rush of water vapour immediately entered the chamber from the room, leading to the Bragg wavelength spiking to longer wavelength before settling to a stable value (Fig 7.14a).

The stable values of the empty chamber and chamber containing DNT were unreliable with the Bragg wavelength of an empty chamber being the same as one containing DNT (Fig 7.14b). This could be due to residual DNT vapour remaining in the chamber, but is more likely to be water vapour. Throughout the experiment the temperature remained constant with less than a 1 °C fluctuation (Fig 7.14c). In this experimental setup the humidity in the chamber was not recorded.

This experiment highlights the extreme and fast cross sensitivity to water vapour, showing the critical need to control and monitor humidity when using the film sensor. It shows that opening the chamber during the experiment and doing cycles of introducing and removing DNT was undesirable.

Dual chamber results

The experiment was refined by introducing a dual chamber that was also humidity controlled, with humidity monitoring included. The second chamber containing the DNT and its vapour was released into the chamber holding the film by opening the valve separating the chambers (Fig 7.15). A slight temperature increase occurred when the chamber was opened resulting in a slight decrease in Bragg wavelength, the air in the second chamber could have been warmer as it was closer to the edge of the fume hood. However, no apparent Bragg wavelength shift to longer wavelength due to DNT exposure was observed after an hour. The concentration of DNT at room temperature and pressure was about 100 to 120 ppb [144], while the water vapour concentration in the chamber at 17.5 %rh was more than twenty thousand times greater at 2,640 ppm.

To increase the DNT vapour concentration it was then heated intensively with a heat gun for 5 minutes creating an atmosphere saturated with DNT vapour to try and generate a measurable response. Although slight Bragg wavelength modulations occurred with temperature changes, there was no apparent 2 nm shift (as was expected with DNT exposure). The humidity remained relatively constant for the duration of the experiment. The film sensor may still be responsive to

DNT, but the DNT concentrations generated here may be below the threshold detection limit for this sensor.

To get an improved and more selective response to DNT and highly polarised explosives, a non-humidity responsive polymer could be used to host the dye. There still may be a small humidity effect due to water associating with the dye, in the same way DNT does, changing the refractive index even if the polymer itself does not swell. In addition, using a higher weight percent of dye might yield a greater response [144]. Although increasing dye loading could introduce problems of aggregation, where dye molecules stack head to tail in such a way that their dipoles cancel each other out, and insolubility during film solution preparation.

Response could be improved by using other molecules with more effective DNT capture mechanisms, such as the incorporation of an organometallic complex [147] or other dyes [144]. Another method to increase the response could have DNT chemically bond with the dye molecule via a chemical reaction. This would alter the electronic environment of the dye, and hence the refractive index, much more than simply associating via van der Waals forces. However, using this method reversibility of the sensor would be an issue, making it suitable for one use only.

An estimation of the size of the DNT molecule can be estimated by determining its kinetic diameter (σ), this is the diameter of the smallest cylinder the molecule will fit. This can be expressed mathematically as $\sigma = 0841 V_c^{1/3}$ where V_c is the critical volume in $cm^3\ mol^{-1}$ [148]. The critical volume of 2,4-DNT is 521.76 $cm^3\ mol^{-1}$ [149] giving a kinetic diameter σ of 0.8 nm, which is much smaller than the 3 nm pore size measured for PMMA. This pore size represents the average of a distribution of pore sizes and the actual diameter may be slightly different due to small changes in size due to it folding into different conformations, forming dimers or associating with water. As such, increasing the pore size to allow better access of the DNT molecule into the polymer might enhance performance.

7.5 Strain response of doped polymer film sensor

The strain response of the film sensor was measured by hanging free weights from the film [54].

7.5.1 Experimental setup

The film sensor was hung vertically by clamping it to a plate next to a Centre 313 probe to record humidity and temperature (Fig 7.16). Strain was applied to the film by attaching a hanger from which slotted free weights could be hung. The hanger consisted of either a small or large clip with a bar and were 8 g and 43 g

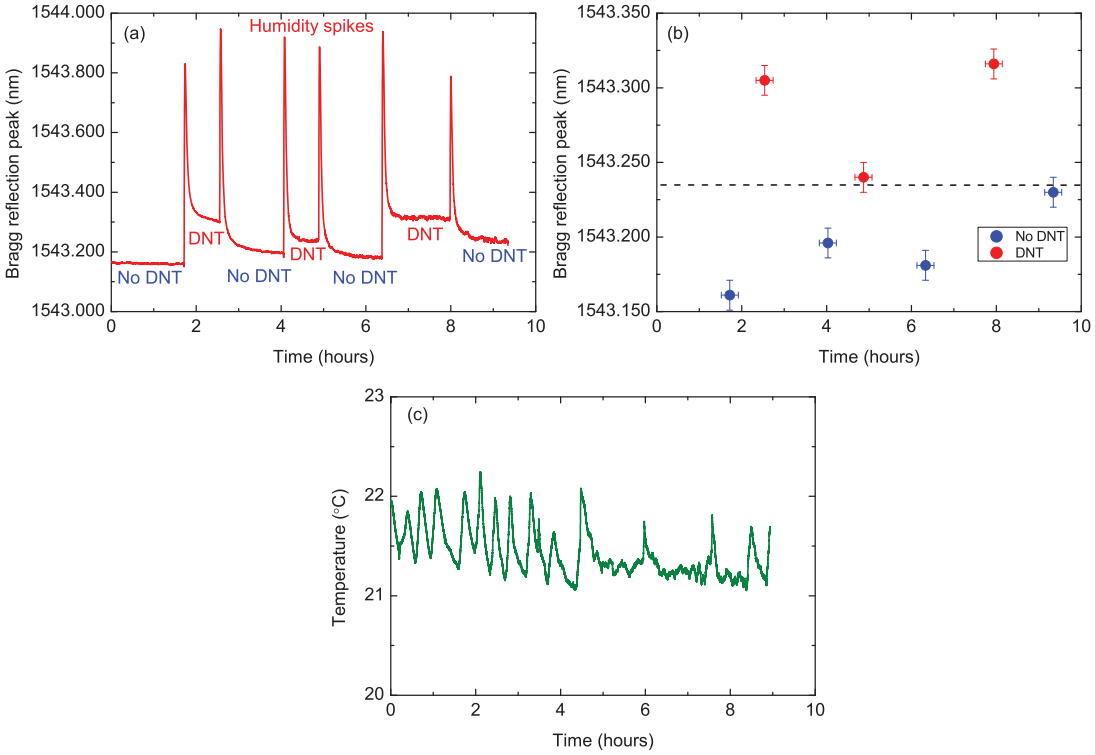


Figure 7.14 – Results from the first chemical sensing experiment for a 17 μm thick film (one cladding) of 3wt% PYR-3/PMMA film sensor exposed to DNT in a single chamber. The (a) Bragg peak wavelength and its (b) stable value and (c) temperature were recorded with time.

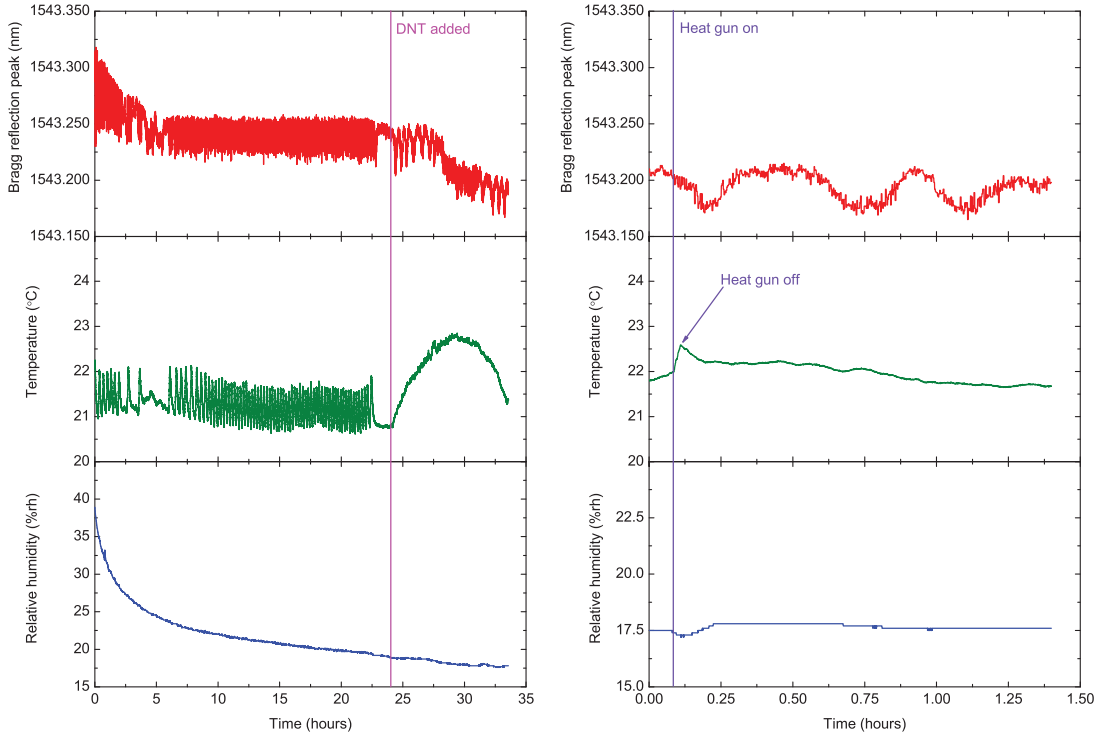
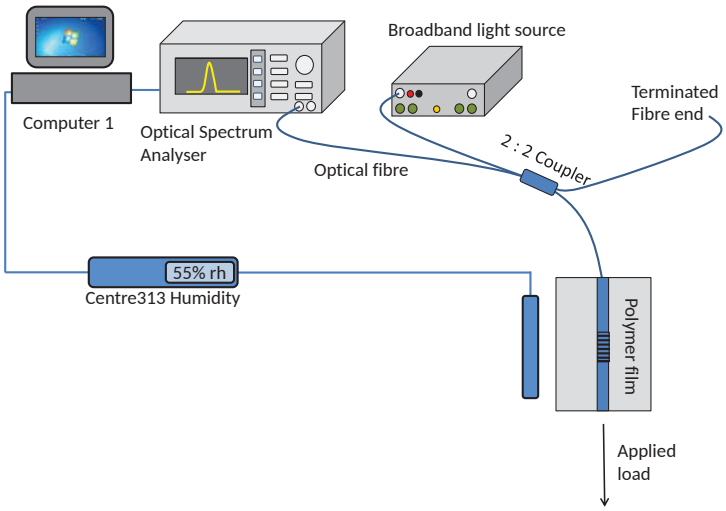


Figure 7.15 – Results from the second chemical sensing experiment for a 17 μm thick film (one cladding) of 3wt% PYR-3/PMMA film sensor exposed to DNT in a dual chamber. Bragg reflection peak, temperature and relative humidity were monitored. The left hand side graphs show the effect of opening the valve to release DNT vapour and the right hand side graphs show the effect of heating the DNT once the valve was opened.



(a) Schematic of the free weight strain setup.



(b) The actual setup used to measure strain.

Figure 7.16 – The free weight strain experimental setup.

respectively. A large clamp was used for large weights as it had a bigger clamp force so it did not slip off the film. The films' fibre connector was connected to a 1550 nm broadband light source and OSA via a 2:2 coupler with the OSA and Centre 313 probe linked to a computer with software to record the Bragg peak, humidity and temperature.

The unweighted film was left for 30 minutes to stabilise to room conditions before starting a strain cycle. The strain cycle consisted of stepwise loading and unloading of a hanger and free weights with a 10 minute waiting period before a weight change. This waiting period was to allow any oscillations induced by the weight change and any effect on temperature and humidity to return to ambient conditions. During measurements the film sensor was isolated to minimise any undesired air-flows.

7.5.2 Strain response

The strain response of two dye-doped film sensors was investigated, 3wt% PYR-3 and 3wt% BAF-1 doped PMMA films. The PYR-3 doped film had two claddings with a total thickness of 27 μm and the BAF-1 doped film had one cladding with a total thickness of 17 μm, these were the same films used for the humidity calibration experiment.

The PYR-3 doped film was subjected to an initial experiment of small strain cycles then it was loaded to failure, while the BAF-1 doped film was subjected to a set of strain cycles below the breaking strain.

PYR-3 doped polymer film sensor strain response

Small strain cycles, well below the expected breaking strain, were simulated by loading and unloading a set of slotted weights (max 12 g) in addition to an 8 g holder (Fig 7.17). As it was strained the Bragg reflection peak shifted to longer wavelength with humidity spikes observed when the weights were changed due to humidity from the operator. Due to the films' extreme response to humidity and the risk of undesirable air flows causing the film and weights to oscillate the area was vacated during the experiment. The unloaded state at the end of the cycle is shifted 180 pm to shorter wavelength from the initial unloaded state, this corresponds to the 3 %rh humidity drop observed (59.3 pm/%rh sensitivity). A set of 5 strain cycles were conducted with a linear response observed (Fig 7.18). There is no clear hysteresis shift to short wavelength that can be seen with newly prepared films. This can be attributed to the films having been well cycled by previous humidity experiments. Some fluctuations in the Bragg reflection peak was observed and could be explained by small humidity fluctuations during the experiment. These humidity fluctuations are evident in the Bragg peak position of cycle 4 (Fig 7.19), which was particularly affected.

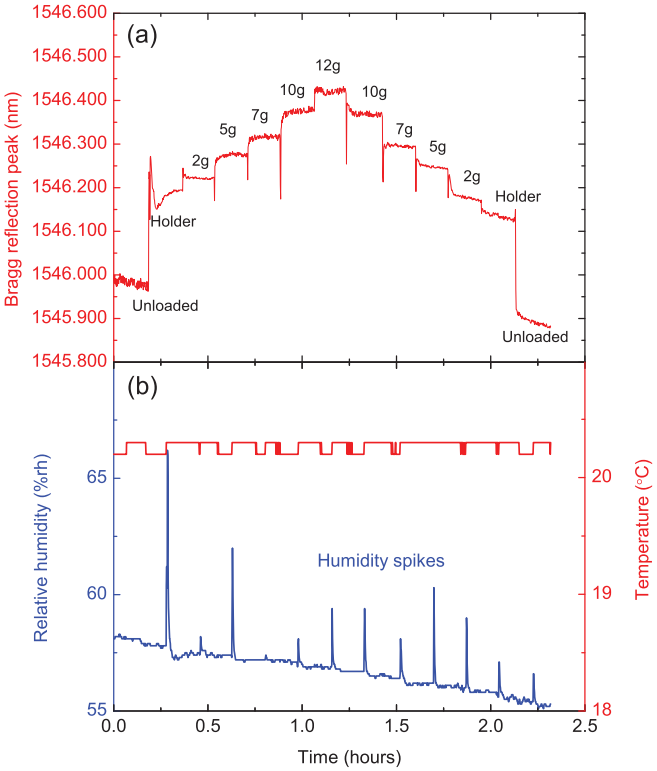


Figure 7.17 – The (a) strain response and (b) humidity and temperature for a 27 μm thick 3wt% PYR-3/PMMA film sensor undergoing a small strain cycle.

Next a large strain was applied to find the breaking strain of the film sensor. Here a larger holder (43 g) was used to provide a sufficient clamp force to prevent it slipping off with much larger weights loaded (Fig 7.20). The film was loaded to 393 g (43 g holder + 350 g mass) resulting in a strain of 7,650 $\mu\varepsilon$ and 12.7 nm

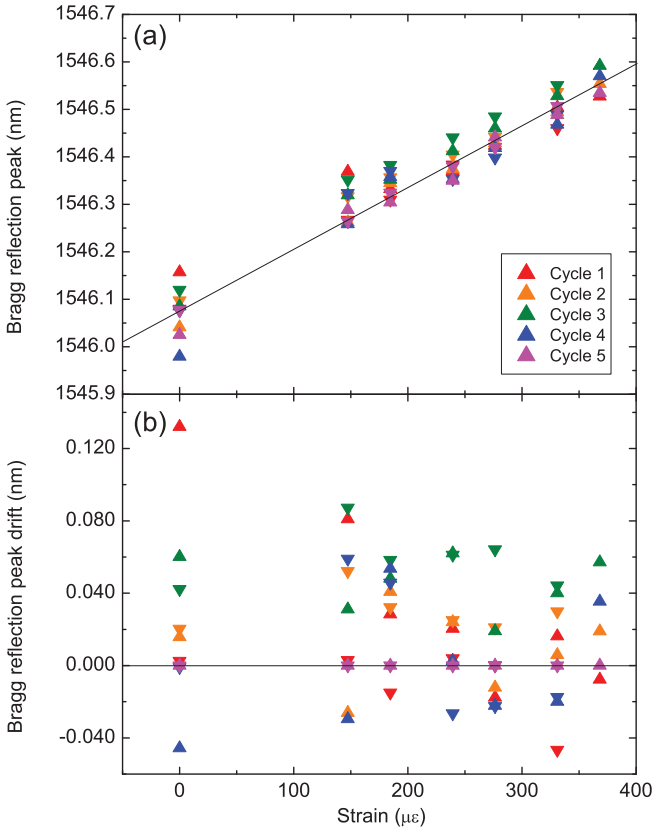


Figure 7.18 – The (a) strain response and (b) deviation from the final strain cycle for a 27 μm thick 3wt% PYR-3/PMMA film sensor undergoing a set of small strain cycle. The lines are guides to the eye.

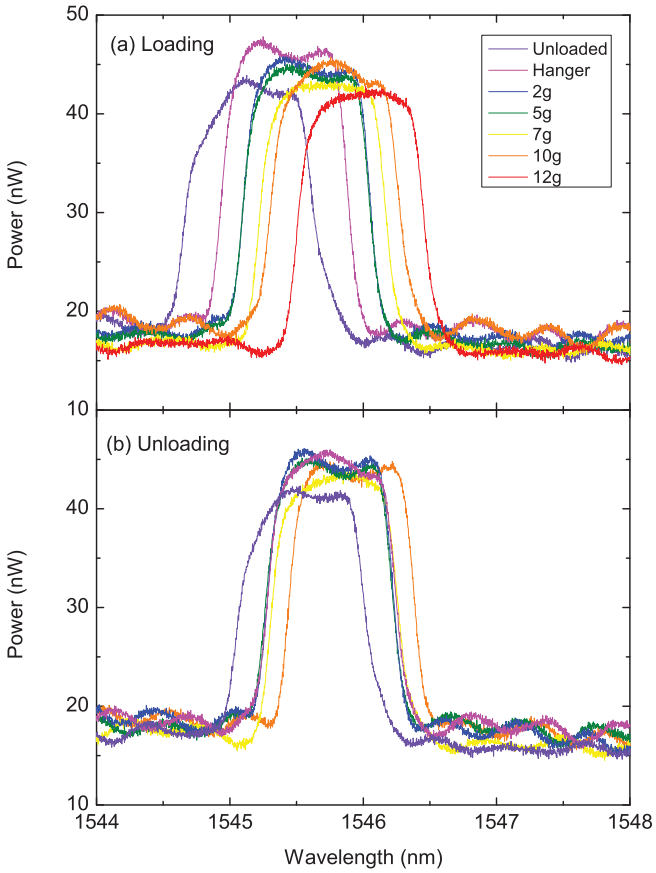


Figure 7.19 – A 27 μm thick 3wt% PYR-3/PMMA film sensor undergoing a (a) loading and (b) unloading strain cycle that is particularly affected by humidity cross sensitivity.

Bragg reflection peak shift, where it held for about 2 minutes before the film broke. The yield strength of PMMA is 65 N/mm^2 [54], while here the maximum tensile stress is only 17 N/mm^2. This means the experiment took place in the elastic region of the stress curve and did not cause any permanent extension. The response was linear with very little deviation from linearity. This can be explained by the large nanometre scale shift due to strain overwhelming any small picometre scale shifts due to humidity fluctuations.

The sensitivity of the sensor was measured as 1.70 pm/$\mu\varepsilon$ (Table 7.4). This sensitivity has contributions from two effects, the change in grating period and change in refractive index with extension. Here the change in grating period with extension $\partial\Lambda/\partial l$ was calculated as 1.04×10^{-4} and the change in refractive index with extension $\partial n_e/\partial l$ as 0.11×10^{-4} μm^{-1}. The change in length ∂l was calculated as 77 μm giving a total change in grating period $\partial\Lambda$ of 4 nm and total change in refractive index ∂n_e of 8.2×10^{-4} when the sensor was loaded to 7,650 $\mu\varepsilon$. Of the observed 12.7 nm shift the change in grating period contributed 11.9 nm to the shift and the refractive index change contributed 0.8 nm.

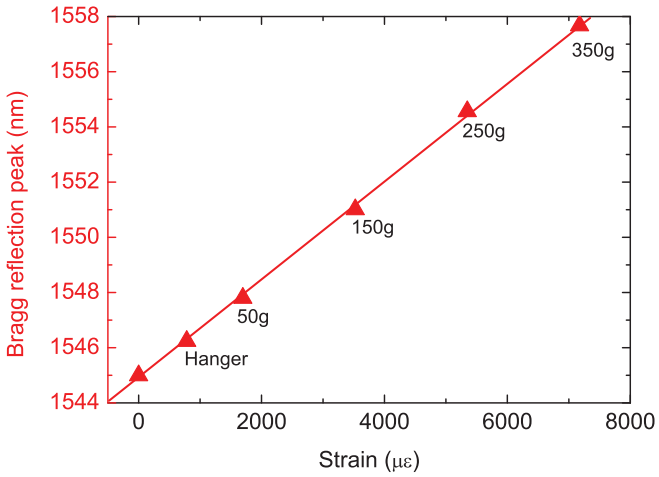


Figure 7.20 – A 27 μm thick 3wt% PYR-3/PMMA film sensor that is loaded to failure. The line is a guide to the eye.

Table 7.4 – Dye-doped film sensor strain experimental results.

Dye/Polymer	PYR-3 / PMMA	BAF-1 / PMMA
Cross sectional area, A (mm^2)	0.22	0.14
Sensitivity (pm/$\mu\varepsilon$)	1.70	1.80
Max tensile stress (N/mm^2)	17.22	10.05
Change in length, ∂l (μm)	76.54	44.67
$\partial\Lambda/\partial l$	1.0×10^{-4}	1.0×10^{-4}
Change in grating period, $\partial\Lambda$ (nm)	4.0	2.3
$\partial n_e/\partial l$ (μm^{-1})	0.11×10^{-4}	0.28×10^{-4}
∂n_e	8.22×10^{-4}	12.6×10^{-4}

Larger strains were able to be achieved on newly prepared uncoupled films with up to 600 g being loaded (11,000 $\mu\varepsilon$) before the glue holding the film failed and the film was was pulled out of the glass housing unit. The film that broke at a loading 393 g (7,650 $\mu\varepsilon$) may have had small tears in it due to previous handling, so the sensor may be able to go to higher strain before failing. Although in reality coupling may be lost due to coupling misalignment as higher strains are applied before the film sensor fails by other means.

BAF-1 doped polymer film sensor strain response

A set of large strain cycles below the films' breaking strain was applied to a BAF-1 doped film. Here the larger holder (43 g) was used and loaded to 143 g (43 g holder + 100 g mass) resulting in a strain of 4,450 $\mu\varepsilon$ generating a Bragg reflection peak shift of 8.3 nm (Figs 7.21&7.22). Again humidity spikes from the operator are observed during weight changes and sudden dips in Bragg reflection are due to the weights being unloaded to allow additional weight to be attached before reloading. A larger spread in peak values, exceeding the contribution due to humidity, was observed. This could be attributed to the sensor being multi-mode, with multiple Bragg reflections, making it more difficult for the peak tracking program to track. There is also the possibility of the strain inducing the dye to undergo cis-trans switching, changing the refractive index. Using a single-mode non-photo switching dye gives a much better strain calibration response (Fig 7.20).

The sensitivity of the BAF-1 doped sensor was measured as 1.80 pm/$\mu\varepsilon$ (Table 7.4). The change in grating period with extension $\partial\Lambda/\partial l$ was calculated as 1.04×10^{-4} and the change in refractive index with extension $\partial n_e/\partial l$ as 0.28×10^{-4} μm^{-1}. The change in length ∂l was calculated as 45 μm giving a total change in grating period $\partial\Lambda$ of 2.3 nm and total change in refractive index ∂n_e of 12.6×10^{-4} when the sensor was loaded to 4,450 $\mu\varepsilon$. Of the observed 8.2 nm shift the change in grating period contributed 6.9 nm to the shift and the refractive index change contributed 1.3 nm.

The PYR-3 and BAF-1 doped sensors have similar sensitivity of 1.70 and 1.80 pm/$\mu\varepsilon$ respectively. The BAF-1 doped sensor has a larger change in refractive index contribution $\partial n_e/\partial l$ with strain of 0.28×10^{-4} μm^{-1} compared to the analogous PYR-3 doped sensor 0.11×10^{-4} μm^{-1}, which could be the effect of using a different dye.

Plain undoped PMMA optical fibre sensors have strain sensitivities reported of 1.1 pm/$\mu\varepsilon$ [150] and 1.4 pm/$\mu\varepsilon$ [151]. This is a lower response than the response observed with the dye-doped PMMA film sensors and the difference in response could be attributed to the effect of using the dye or different molecular weight PMMA. The dye-doped film sensors strain response also exceeds traditional silica fibre based FGB strain sensors that have sensitivities reported of 1.5 pm/$\mu\varepsilon$ [152]

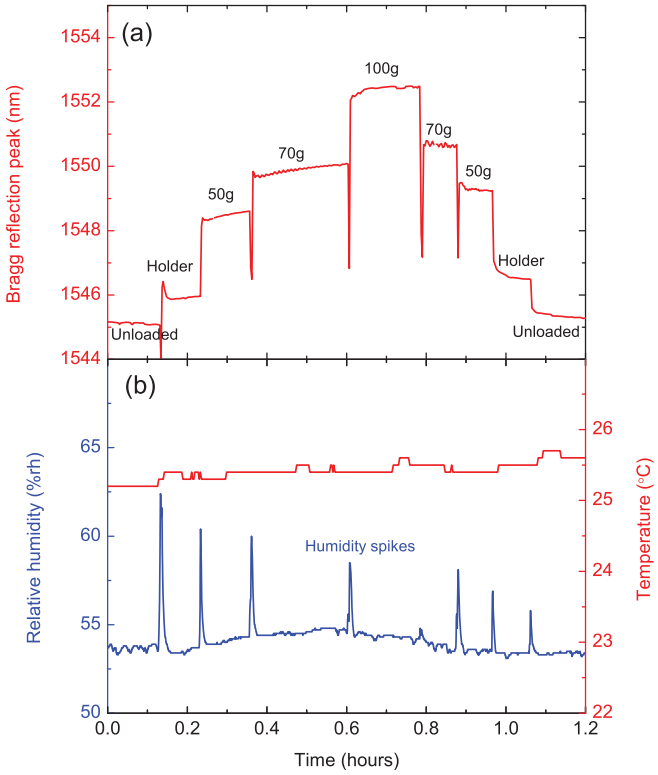


Figure 7.21 – The (a) strain response and (b) humidity and temperature for a 17 μm thick 3wt% BAF-1/PMMA film sensor undergoing a strain cycle.

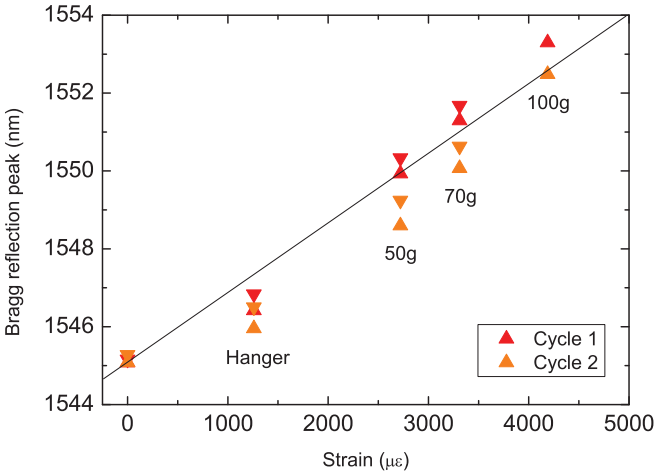


Figure 7.22 – A 17 μm thick 3wt% BAF-1/PMMA film sensor undergoing a set of strain cycles.

and 1.3 pm/$\mu\varepsilon$ [1].

7.6 Summary and future work

In summary, the strain, temperature and chemical response of the dye-doped optical sensors were investigated. The humidity response of the dye-doped film sensors ranged from 44.6 to 62.1 pm/%rh which is larger than similar undoped PMMA fibres. A two-layer model was proposed to model the response of the film sensor to a humidity step change. A small amount of hysteresis was observed, similar what was observed with the fibre polymer coatings, with the hysteresis subsiding as the solvent was removed and the polymer settled in. The optical glue securing the input optical fibre was also humidity responsive, affecting coupling power as humidity changed. The temperature response of the sensor was investigated with a shift to shorter wavelength observed due to a dominate thermo-optic coefficient before the glue failed and the sensor was lost. Additional sensors would need to be fabricated and tested to investigate sensing reproducibility.

The film sensors' chemical response to DNT was investigated. Here an extreme cross sensitivity to humidity was observed with no response to DNT seen. The film sensor may still be responsive to DNT but the DNT concentrations used here may be below the threshold detection limit for this sensor.

The strain response of the film sensor was found to vary from 1.70 to 1.80 pm/$\mu\varepsilon$. This response was in excess of that observed for undoped polymer optical fibres and silica fibres. Humidity cross sensitivity also influenced strain measurements and would need to be accounted for when the film is used as a strain sensor.

The future work has a wealth of exciting opportunities with this novel sensor. The first challenge to enable exploring these opportunities more easily would be to improve the method of coupling the film to the optical fibre. Using an optically curable glue that was rated to a higher temperature with lower shrinkage on curing would be a first step. The cured glue and film could then be coated with a waterproof coating to remove the interference from humidity.

To enhance the humidity sensing performance different polymers can be trialled. From the coated fibres' work P84 HT was an excellent candidate. However, the polymer is turbid and excessive scattering may occur as light is guided in the waveguide. If this is the case it could be used as an additional cladding layer over the existing lower refractive index PMMA cladding. Other work includes trialling different dyes and using different dye loadings to see if performance is improved. The performance as a temperature sensor will be enhanced with an optical glue that is rated to a higher temperature. Additionally using a non-turbid polymer with a higher glass transition temperature such as APC (218 °C) [45] would allow higher temperatures to be measured.

To greatly improve performance as a chemical sensor the cross sensitivity with

humidity should be minimised. This could be done using a polymer that is non-humidity responsive. To achieve sensitivity to DNT and other nitro-aromatic explosives, organometallic complexes or different dyes*, and higher dye loadings could be trialled. Another method would be to have the explosive chemically bond with the dye and would be much more responsive than the other methods based on associations due to van der waals forces. However, this method would not be reversible and the sensor would be a one time use detector.

Further enhancement of the sensors' strain response could be achieved by modifying the chemical structure of the dye and polymer by tethering the dye to polymer or by poling the dye. This will enhance the dyes' polarisation change when strained, shifting the absorption peak of the dye and in turn cause a greater refractive index change. Polymers with different Young's moduli can also be trialled to improve the strain response. The humidity cross sensitivity can be eliminated by attaching the film to the structure requiring strain monitoring with strain cement then encasing the whole assembly with a waterproof layer.

For long term use and repeatability of the sensor in any sensing application, it would be advantageous to encapsulate the sensor to prevent UV light degrading the polymer or visible light and oxygen degrading the dye.

But perhaps the most exciting opportunity is the creation of a dye-doped film optical sensing chip. Here the chip could have a rosette shaped waveguide with multiple Bragg gratings allowing strain tensors to be measured in real time. Different polymers and grating periods could be utilised to allow the chip simultaneously measure humidity and temperature. The large refractive change induced by dye doping would allow much smaller Bragg gratings to be formed, enabling the chip to be very small in size.

*Such as the DNT responsive dyes studied in reference [144].

Chapter 8

Summary

The motivation of this study was to develop optical sensors to measure strain, temperature and chemical concentrations. Fibre optic sensors are ideally suited for compact and harsh conditions, including high electric field or explosive environments where traditional sensors can not be used. Two types of optical sensor were developed and characterised in this thesis. A humidity sensor that consisted of novel polymer coatings on an existing glass fibre Bragg gratings and a novel dye-doped polymer film developed for humidity, temperature, chemical and strain sensing.

The results from the coated glass fibre humidity sensors investigated in chapter 4 show that polyimide coated sensors were the most responsive to humidity, of the polymer coatings investigated. This responsiveness might be due to the polyimide having a higher density of water-associating sites. By modifying the chemical structure of a polyetherimide the humidity sensing performance was enhanced. The modifications reduced the effect of chain whipping and shielding and increased the number of water associating sites. The humidity calibration experiments showed that after the initial coating of a fibre, the Bragg reflection peak drifts to lower wavelength, before settling on a reproducible response. This drift was partially attributed to residual solvent in the coating being removed. The sensor required cycling a number of times before it could be calibrated. The humidity sensitivity of a fibre coating was enhanced, by either increasing the coating thickness or reducing the fibre cladding diameter.

The time response of the coated fibres to large humidity step changes were presented in chapter 5. A two-layer model was proposed, with a fast time constant representing the portion of the coating that can have moisture easily occupy and exit, and a slow time constant for the deeper part of the coating that was slower to respond. This model provided good fits to the experimental data, and allowed the performance of different coatings to be compared. By solving the basic diffusion equation with COMSOL, using a mesh model, an estimation could be made of the coatings' water absorption and desorption diffusion coefficients. This model sometimes struggled with fitting the time response data, and could possibly be improved by utilising a non-Fickian diffusion model. The effect of

coating thickness and fibre cladding diameter was examined. While no significant time response difference was observed for a coating of the same thickness on different fibre cladding diameters, the time response increases rapidly with increasing coating thickness.

Chapter 6 presented the fabrication of the novel dye-doped film sensors. Here the method for the preparation and coupling of the film sensor with a single-mode fibre was developed. The alignment of the phase mask and input fibre were found to be critical. Single Bragg reflections were only observed in a single-mode waveguide, with the correct phase mask alignment, and when a non photo-switchable dye was used. The Bragg reflection peak was observed at a shorter wavelength than expected after writing with a phase mask. This was attributed to the film being strained by shrinkage, occurring during the post spin coating drying procedure. This strain was subsequently released once the film was removed from the substrate.

The strain, temperature and chemical response of the dye-doped optical sensors were reported in chapter 7. The sensors were found to have a large humidity response, greater than similar undoped polymer fibres and polymer-coated glass fibre sensors. This enhanced sensitivity was attributed to the use of a dye-dopant. A small amount of hysteresis was observed, which subsided as the solvent was removed and the polymer relaxed. The temperature response studies revealed a shift to shorter Bragg wavelength with increasing temperature, due to the dominant effect of refractive index changes with temperature.

These experiments showed that the optical glue securing the input optical fibre could be improved, to prevent coupling power fluctuations with humidity changes and power loss at higher temperature. The sensors were tested for their chemical response to DNT, an analogous molecule to nitro aromatic explosives. Here an extreme cross sensitivity to humidity was observed with no sensitivity to DNT observed. The DNT concentrations used here were below the threshold detection limit of the sensor. Strain calibration measurements were conducted, the sensor's response was found to be in excess of that observed for undoped polymer optical fibres, and silica fibres. Humidity cross-sensitivity also influenced strain measurements, and would need to be accounted for when the sensor is used in practice.

Future prospects

There is a wealth of new opportunities and directions to take for the continued development of sensors investigated here. The coated optical fibre sensors could have their humidity response further enhanced by modifying the chemical structure of the polyimide coatings. Achieving solubility of the polyimide to allow the coating to be applied on the fibre will be the greatest challenge. This fibre Bragg grating moisture sensor would have potential applications in fuel cells [80, 81],

high temperature furnaces [82, 83], cold storage [84–86] and power transformers [87].

The sensor could be adapted to sense another vapour or gas, with potential applications including sensing hydrogen in fuel cells [88], dissolved gases in power transformers [153] and ethylene during fruit ripening [89]. Optical sensors are a safe method of measuring these gases at high concentrations where the risk of ignition is significant. The time response of the developed sensors will need to be characterised; here the two layer and mesh model could be directly applied or altered to enable this.

A particularly exciting future awaits the dye-doped film sensors. Now that the basic development and characterisation process has been developed, this sensor can be modified and enhanced. Its temperature response range could be increased using higher temperature rated curable glues and polymers. The humidity response could be greatly enhanced by incorporating polyimide as either the dye-doped polymer or a cladding. Temperature compensation could be provided by an additional Bragg grating in a non-humidity responsive material. Alternatively an additional Bragg reflection peak that is sufficiently far away from the peak used to monitor humidity could be used.

The chemical response could be improved by using a different dye and investigating dye loadings. Another focus could be trialling other polymers to host the dye or developing a chemical selective cladding layer as the sensing element. Cross sensitivity, particularly to humidity, will be a key consideration. Alternatively, the chemical analyte could undergo a chemical reaction with the dye. This method would be significantly more responsive than other methods reliant on detection by association from van der waals forces. However, reversibility of the sensor would be an issue.

There is a number of ways to improve the strain sensor. Firstly, its strain response could be further improved by enhancing the strain optic effect either by poling an electro-optic dye and/or tethering the dye to the polymer. Secondly, by developing dye-doped rosettes, which allow strain tensors to be resolved. The sensor could be further explored by trialling different dyes and studying the effect of different dye loadings. One of the main advantages of using dye-doping is that the induced refractive index change is much larger than in undoped Bragg grating sensors. This would enable smaller gratings to be developed that could ultimately lead to the development of an integrated optical sensing chip.

Bibliography

[1] A. Othonos and K. Kalli. *Fiber Bragg Gratings - Fundamentals and Applications in Telecommunications and Sensing*. Artech House, Inc., 1999.

[2] N. David. *Fiber Optic Sensors for PEM Fuel Cells*. PhD thesis, University of Victoria, 2011.

[3] B. Zhang and M. Kahrizi. High-temperature resistance fiber Bragg grating temperature sensor fabrication. *IEEE Sensors Journal*, 7(4):586–591, April 2007.

[4] D. Krohn, T. MacDougall, and A. Mendez. *Fiber optic sensors fundamental and applications*. SPIE Press, 2014.

[5] B. E. A. Salech and M. C. Teich. *Fundamentals of Photonics (2nd Edition)*. John Wiley & Sons, Ltd, 2007.

[6] M.G. Kuzyk. *Polymer Fiber Optics: Materials, Physics, and Applications*. Optical Science and Engineering Series. Taylor & Francis Group, 2007.

[7] X. Song and R. Leonhardt. Ray-optics analysis of single mode condition for optical waveguides with rectanugular cross-section. *Progress in electromagnetics research*, 135:81–89, 2013.

[8] K. T. V. Grattan and T. Sun. Fibre optic sensor technology: an overview. *Sensors and Actuators*, 82:40–61, November 2000.

[9] B. Culshaw and A. Kersey. Fiber-optic sensing: A historical perspective. *Journal of light wave technology*, 26(9):1064–1078, May 2008.

[10] R. Bogue. Fibre optic sensors: a review of today's applications. *Sensor Review*, 1:304–309, 2011.

[11] G. Berruti, M. Consales, M. Giordano, L. Sansone, P. Petagna, S. Buontempo, G. Breglio, and A. Cusano. Radiation hard humidity sensors based on polyimide-coated fiber Bragg gratings. *Sensors and Actuators B: Chemical*, 177:94–102, 2013.

[12] B. Lee. Review of the present status of optical fibre sensors. *Optical Fibre Technology*, 9:57–79, August 2002.

[13] A. Mendez and T. Graver. Overview of fiber optic sensors for NDT applications. In *4th NDT Panamerican conference, Buenos Aires*, 2007.

[14] A. Cusano, A. Cutolo, and J. Albert. *Fiber Bragg grating sensors, Research advancements, industrial applications and market exploitation.* Bentham books, 2014.

[15] S. Lecler and P. Meyrueis. *Fiber optic sensors.* InTech, 2012.

[16] W. B. Spillman and E. Udd. *Field guide to fibre optic sensors.* SPIE Press, 2014.

[17] E. Udd. *Fiber optic sensors: An introduction for engineers and scientists.* Wiley InterScience, New York, 1991.

[18] Y. J. Rao. In-fibre Bragg grating sensors. *Meas. Sci. Technol.*, 8:355–375, November 1997.

[19] S. Benton et al. *Holographic Imaging.* John Wiley and Sons Ltd, 2008.

[20] A. Ikhlef, R. Hedara, and M. Chikh-Bled. Uniform fibre Bragg grating modeling and simulation used matrix transfer method. *International journal of computer science issues*, 9(2):368–374, 2012.

[21] P. Wagner. Development and characterization of optical strain sensors. Master's thesis, University of Applied Science Darmstadt, 2012.

[22] M. Panczyk. Development and characterisation of fibre Bragg grating based strain temperature sensing systems. Technical report, Industrial Research Limited, 2012.

[23] M. Silva-Lopez et al. Strain and temperature sensitivity of a single-mode polymer optical fiber. *Opt. Lett.*, 30(23):3129–3131, Dec 2005.

[24] R. Oliveira, L. Bilro, and R. Nogueira. Bragg gratings in a few mode microstructured polymer optical fiber in less than 30 seconds. *Optics Express*, 23(8):10181–10187, April 2015.

[25] P. Lu, L. Men, and Q. Chen. Resolving cross sensitivity of fiber Bragg gratings with different polymeric coatings. *Applied Physics Letters*, 92(17):171112–171112–3, Apr 2008.

[26] Z. Zhou and J. Ou. Techniques of temperature compensation for FBG strain sensors used in long-term structural monitoring. In *Proceeding of Asian Pascifc Fundamental Problems of Opto- and Microelectronics (APCOM 2004)*, volume 5851, pages 167–172. SPIE, 2005.

[27] S. J. Mihailov et al. Apodization technique for fiber grating fabrication with a halftone transmission amplitude mask. *Applied Optics*, 39(21):3670–3677, July 2000.

[28] H. Singh and M. Zippin. Apodized fiber Bragg gratings for DWDM applications using uniform phase mask. In *ECOC'98 Madrid Spain*, 1998.

[29] I. Riant et al. Chirped fiber Bragg gratings for WDM chromatic dispersion compensation in multispan 10-Gb/s transmission. *IEEE Journal Of Selected Topics In Quantum Electronics*, 5(5):1312–1324, September 1999.

[30] Z. Zhao et al. Fabrication of a tilted fiber Bragg grating with a designed reflection spectrum profile. *Optics Letters*, 29(3):244–246, February 2004.

[31] X. Dong et al. Tilted fiber Bragg gratings: Principle and sensing applications. *Photonic Sensors*, 1(1):6–30, October 2011.

[32] Y. Huang et al. Tunable superstructure fiber Bragg grating with chirp-distribution modulation based on the effect of external stress. *Optics Letters*, 37(18):3918–3920, September 2012.

[33] B. O. Guan and H. Y. Tam. Simultaneous strain and temperature measurement using a superstructure fiber Bragg grating. *IEEE Photonics Technology Letters*, 12(6):675–677, June 2000.

[34] S. Blais. *Superstructured fibre Bragg gratings and applications in microwave signal processing.* PhD thesis, University of Ottawa, 2014.

[35] Y. Jeong, J. K. Sahu, D. N. Payne, and J. Nilsson. Ytterbium-doped large-core fiber laser with 1kW continuous-wave output power. *Electronics Letters*, 40:470–472, 2004.

[36] Y. Xiao, F. Brunet, M. Kanskar, M. Faucher, A. Wetter, and N. Holehouse. 1-kilowatt CW all-fiber laser oscillator pumped with wavelength-beam-combined diode stacks. *Optics Express*, 20:3296–3301, 2012.

[37] J. W. Dawson et al. Analysis of the scalability of diffraction-limited fiber lasers and amplifiers to high average power. *Optics Express*, 16:1324013260, 2008.

[38] G. Oulundsen, K. Farley, J. Abramczyk, and K. Wei. Fiber for fiber lasers: Matching active and passive fibers improves fiber laser performance. *Laser Focus World*, 48:391, January 2012.

[39] B. Samson, A. Carter, and K. Tankala. Rare-earth fibres power up. *Nature Photonics*, 5(8):466, 2011.

[40] S. Magne, S. Rougeault, M. Vilela, and P. Ferdinand. State-of-strain evaluation with fiber Bragg grating rosettes: application to discrimination between strain and temperature effects in fiber sensors. *Appl. Opt.*, 36(36):9437–9447, December 1997.

[41] Y. Lin and W. Wang. A novel fiber Bragg grating sensor with temperature compensation. In *Photonics and Optoelectronics, 2009. SOPO 2009. Symposium on*, pages 1 –3, August 2009.

[42] L. Alwis, T. Sun, and K. T. V. Grattan. Optical fibre-based sensor technology for humidity and moisture measurement: Review of recent progress. *Measurement*, 46:4052–4074, 2013.

[43] J. Lovell-Smith and R. Mason. Humidity workshop. Booklet, 2013.

[44] C. I. Merzbacher, A. D. Kersey, and E. J. Friebele. Fiber optic sensors in concrete structures: a review. *Smart Mater. Struct.*, 5:196–208, 1995.

[45] Y. Kutuvantavida. *Opitcal properties of oganic NLO chromophores for terahertz applications*. PhD thesis, Massey University, 2012.

[46] Laurell Technologies Corporation. *WS-400/500B Lite series Spin Processor Operation Manual*, April 2005.

[47] Micromeritics. *ASAP 2020 Accelerated Surface Area and Porosimetry System Operators Manual*, v4.01 edition, October 2011.

[48] Metricon Corporation. *Metricon Models 2010 and 2010/M Prism coupler thin film thickness/refractive index measurement system operation and maintenace guide - windows progam*, January 2003.

[49] PerkinElmer. *High performance Lambda Spectrometers Getting Started Guide*, December 2007.

[50] Southern Photonics. *OSA 150i User Manual*, 1st edition, 2012.

[51] Anritsu Corporation. *MS9740A Optical Spectrum Analyzer Operation Manual*, 13 edition, June 2013.

[52] Superlum. Tips for selecting the appropriate broadband light source. Technical report, Superlum, December 2014.

[53] Thunder Scientific Corporation. *Series 2500 Benchtop two-pressure humidity generator operation and maintenance manual*. Thunder Scientific Corporation, 15 edition, 2014.

[54] M. Rosenberger, G. Koller, S. Belle, B. Schmauss, and R. Hellmann. Polymer planar Bragg grating sensor for static strain measurements. *Optics letters*, 38(5):772–774, March 2013.

[55] T. L. Yeo, T. Sun, K. T. V. Grattan, D. Parry, R. Lade, and B. D. Powell. Characterisation of a polymer-coated fibre Bragg grating sensor for relative humidity sensing. *Sensors and Actuators B: Chemical*, 110(1):148 – 156, 2005.

[56] *Determination of the coefficient of moisture expansion (CME)*, volume Proceedings of the 9th International Symposium on Materials in a Space Environment of *Noordwijk, The Netherlands, 16-20 June 2003 (ESA SP-540, September 2003)*, 2003.

[57] N. A. David, P. M. Wild, and N. Djilali. Parametric study of a polymer-coated fibre-optic humidity sensor. *Measurement Science and Technology*, 23(3):035103, 2012.

[58] P. Kronenberg, P. K. Rastogi, P. Giaccari, and H. G. Limberger. Relative humidity sensor with optical fiber Bragg gratings. *Opt. Lett.*, 27(16):1385–1387, Aug 2002.

[59] P. Yimsiri and M. R. Mackley. Spin and dip coating of light-emitting polymer solutions: Matching experiment with modelling. *Chemical Engineering Science*, 61(11):3496 – 3505, 2006.

[60] D. Grosso. How to exploit the full potential of the dip-coating process to better control film formation. *J. Mater. Chem.*, 21:17033–17038, 2011.

[61] R. Krechetnikov and G. M. Homsy. Experimental study of substrate roughness and surfactant effects on the Landau-levich law. *Physics of Fluids*, 17(10):1385–1387, Oct 2005.

[62] S. F. Cheng and L. K. Chau. Colloidal gold-modified optical fiber for chemical and biochemical sensing. *Analytical Chemistry*, 75(1):16–21, 2003.

[63] J. A. Howarter and J. P. Youngblood. Optimization of silica silanization by 3-aminopropyltriethoxysilane. *Langmuir*, 22(26):11142–11147, 2006.

[64] HD MicroSystems. VM-651 and VM-652 adhesion promoters. Technical report, HD MicroSystems, 2008.

[65] E. M. Davis and Y. A. Elabd. Water clustering in glassy polymers. *The Journal of Physical Chemistry B*, 117(36):10629–10640, 2013.

[66] Z. Chen and C. Lu. Humidity sensors: A review of materials and mechanisms. *Sensor Letters*, 3(4):274–295, 2005.

[67] C. Roman et al. A capacitive-type humidity sensor using crosslinked poly(methyl methacrylate-co-(2 hydroxypropyl)-methacrylate). *Sensors and Actuators B: Chemical*, 25(13):710 – 713, 1995. Proceedings of the Fifth International Meeting on Chemical Sensors.

[68] S. C. Her and C. Y. Huang. Effect of coating on the strain transfer of optical fiber sensors. *Sensors (Basel, Switzerland)*, 11(7):6926–6941, 2011.

[69] T. L. Yeo, T. Sun, K. T. V. Grattan, D. Parry, R. Lade, and B. D. Powell. Polymer-coated fiber Bragg grating for relative humidity sensing. *Sensors Journal, IEEE*, 5(5):1082–1089, 2005.

[70] F. Ding, L. Wang, N. Fang, and Z. Huang. Experimental study on humidity sensing using a FBG sensor with polyimide coating. *Proc. SPIE*, 7990:1–7, 2010.

[71] L. Wang, N. Fang, and Z. Huang. *High Performance Polymers - Polyimides Based - From Chemistry to Applications*. InTech, 2012.

[72] L. E. Stephans, A. Myles, and R. R. Thomas. Kinetics of alkaline hydrolysis of a polyimide surface. *Langmuir*, 16(10):4706–4710, 2000.

[73] Draw Tower Gratings. Does humidity affect the wavelength of a FBG. Technical report, Draw Tower Gratings, 2013.

[74] T. Habisreuther, E. Hailemichael, W. Ecke, I. Latka, K. Schroder, C. Chojetzki, K. Schuster, M. Rothhardt, and R. Willsch. ORMOCER coated fiber-optic Bragg grating sensors at cryogenic temperatures. *Sensors Journal, IEEE*, 12(1):13–16, Jan 2012.

[75] L. Lien, C. M. Fellows, L. Copeland, B. S. Hawkett, and R. G. Gilbert. Water-binding and oxygen permeability in poly(vinyl alcohol) films. *Australian Journal of Chemistry*, 55:507–512, 2006.

[76] T. Venugopalan, T. L. Yeo, T. Sun, and K. T. V. Grattan. LPG-based PVA coated sensor for relative humidity measurement. In *Proc. SPIE 6619, Third European Workshop on Optical Fibre Sensors*, 2007.

[77] K. K. Mokwena, J. Tang, and M. P. Laborie. Water absorption and oxygen barrier characteristics of ethylene vinyl alcohol films. *Journal of Food Engineering*, 105(3):436 – 443, 2011.

[78] T. Matsumoto, K. Nakamae, T. Ocjiumi, T. Tamura, and T. Shioyama. The solubility and the wet spinning of ethylene-vinyl alcohol copolymers. *Bull Inst Chem Res, Kyoto Univ*, 52:403–415, 1974.

[79] Q. Chen and P. Lu. *Atomic, Molecular and Optical Physics: New Research*. Nova Science Publishers, 2008.

[80] N. A. David, P. M. Wild, J. Jensen, T. Navessin, and N. Djilali. Simultaneous in situ measurement of temperature and relative humidity in a PEMFC using optical fiber sensors. *J. Electrochem. Soc.*, 157(8):1173–1179, June 2010.

[81] F. K. Coradin et al. Etched fiber Bragg gratings sensors for water-ethanol mixtures: a comparative study. *J. Microw. Optoelectron. Electromagn. Appl.*, 9(2):131–143, Novemeber 2010.

[82] S. J. Mihailov. Fiber Bragg grating sensors for harsh environments. *Sensors*, 12:1898–1918, February 2012.

[83] S. Trpkovski, D. J. Kitcher, G. W. Baxter, S. F. Collins, and S. A. Wade. High-temperature-resistant chemical composition Bragg gratings in Er3+-doped optical fiber. *Optics Letters*, 30(6):607–609, March 2005.

[84] Z. S. Guo, J. Feng, and H. Wang. Cryogenic temperature characteristics of the fiber Bragg grating sensors. *Cryogenics*, 52(10):457–460, 2012.

[85] S. Gupta, T. Mizunami, T. Yamao, and T. Shimomura. Fiber Bragg grating cryogenic temperature sensors. *Applied Optics*, 35(25):5202–5205, 1996.

[86] T. Mizunami, H. Tatehata, and H. Kawashima. High-sensitivity cryogenic fibre-Bragg-grating temperature sensors using teflon substrates. *Meas. Sci. Technol.*, 12:914–917, 2001.

[87] R. Allil. *Current Trends in Short- and Long-period Fiber Gratings*. Intech, 2013.

[88] G. Gupta and W. H. Steier. Modeling photobleaching of optical chromophores: Light-intensity effects in precise trimming of integrated polymer devices. *J. phys. chem. C*, 112(21):80518060, 2008.

[89] S. M. Cristescu et al. Current methods for detecting ethylene in plants. *Annals of botany*, 1(1):1–14, 2012.

[90] A. Hacinliyan, Y. Skarlatos, G. Sahin, K. Atak, and O. O. Aybar. Possible stretched exponential parametrization for humidity absorption in polymers. *The European Physical Journal E*, 28(4):369–376, 2009.

[91] J. L. Mrotek, M. J. Matthewson, and C. R. Kurkjian. Diffusion of moisture through optical fiber coatings. *Journal of Lightwave Technology*, 19(7):988–993, July 2001.

[92] N. G. Harbach. *Fibre Bragg gratings in polymer optical fibres*. PhD thesis, cole Polytechnique Fdrale De Lausanne, 2008.

[93] W. Zhang, D. J. Webb, and G. Peng. Investigation into time response of polymer fiber Bragg grating based humidity sensors. *Journal of Lightwave Technology*, 30(8):1090–1096, 2012.

[94] J. W. Lovell-Smith and R. Mason. Calibration of relative humidity sensors using the transient response. Technical report, Callaghan Innovation, 2014.

[95] P. Zhang. Comsol simulation of water diffusion in polymers and the determination of diffusion coefficients. Technical report, Callaghan Innovation, 2014.

[96] J. Crank. *The mathematics of diffusion*. UK: Clarenan Press, 1975.

[97] M. Kleemann, A. Suisalu, and J. Kikas. Polymer film doped with a solvatochromic dye for humidity measurement. *Proceedings of SPIE Optical Materials and Applications*, 5946:1–7, 2005.

[98] D. S. Cohen and E. A. Stanley. Gaseous diffusion in glassy polymers. *Journal of applied mathematics*, 43(4):949–970, 1983.

[99] L. Masaro and X. X. Zhu. Physical models of diffusion for polymer solutions, gels and solids. *Progress in polymer science*, 24:731–775, 1999.

[100] D. A. Edwards. Non-Fickian diffusion in thin polymer films. *Journal of Polymer Science: Part B: Polymer Physics*, 34:981–997, 1996.

[101] I. A. Kathawalla and J. L. Anderson. Pore size effects on diffusion of polystyrene in dilute solution. *Industrial & Engineering Chemistry Research*, 27:866–871, 1988.

[102] M. Karimi. *Diffusion in Polymer Solids and Solutions Mass transfer in chemical engineering processes*. InTech Open, 2011.

[103] W. Chen, S. Lee, and B. Ho. Diffusion coefficients of acrylic monomers in poly(methyl methacrylate). *Journal of Polymer Research*, 5(3):187–191, July 1998.

[104] T. Liu, R. Ozisik, and R. W. Siegel. Nanoporous polymer films from immiscible polymer blends: Pore size and composition dependence. *Mater. Res. Soc. Symp. Proc.*, 856:1–6, 2005.

[105] Z. Xiong, B. Peng, B. Wu, and P. L. Chu. Highly tunable Bragg grating in single-mode polymer optical fibres. *IEEE Photonics Technology Letters*, 11(3), March 1999.

[106] A. Zhang, S. Gao, G. Yan, and Y. Bai. Advances in optical fiber Bragg grating sensor technologies. *Photonic Sensors*, 2:1–13, 2012.

[107] A. Argyros. Review article microstructures in polymer fibres for optical fibres, THz waveguides, and fibre-based metamaterials. *ISRN Optics*, 2013(785162):22, 2013.

[108] K. E. Carroll, C. Zhang, D. J. Webb, K. Kalli, A. Argyros, and M. C. J. Large. Thermal response of Bragg gratings in PMMA microstructured optical fibres. *Optics express*, 15(14):8844–8850, 2007.

[109] M. Rosenberger, G. Koller, S. Belle, B. Schmauss, and R. Hellmann. Planar Bragg grating in bulk polymethylmethacrylate. *Optics express*, 20(25):27288–27296, December 2012.

[110] I. J. G. Sparrow, P. G. R. Smith, G. D. Emmerson, S. P. Watts, and C. Riziotis. Planar Bragg grating sensors - fabrication and applications: A review. *Journal of Sensors*, 2009:1–12, 2009.

[111] E. McKenna and A. R. Mickelson. Slow light structures in dye-doped polymer waveguides. *Applied optics*, 46(20):4407–4412, 2007.

[112] E. McKenna. *Submicron structures in dye-doped polymer waveguide materials*. PhD thesis, University of Colorado, 2006.

[113] E. McKenna, J. Xue, R. Fan, L. Bintz, R. Dinu, and A. R. Mickelson. Wavelength dependence of irreversible photobleaching of dye-doped polymer waveguide materials. *Applied Optics*, 44(15):3063–3068, 2005.

[114] S. Lin, W. Feng, B. Hooker, and A. R. Mickelson. UV bleaching of polymer and polymeric directional couplers for optical interconnects. *Proceedings of SPIE - The International Society for Optical Engineering*, 2285:415–423, 1994.

[115] E. M. McKenna, A. Lin, A. Waskiewicz, and A. R. Mickelson. In-situ monitoring of slow light structures in dye-doped polymer waveguide materials. *Proc. of SPIE 6713, Nanophotonics and Macrophotonics for Space Environments*, 6713:1–8, September 2007.

[116] J. Ma, S. Lin, W. Feng, R. J. Feuerstein, B. Hooker, and A. R. Mickelson. Modeling photobleacher optical polymer waveguides. *Applied Optics*, 34(24):5352–5360, August 1995.

[117] D. J. Goodwill, R. S. Fan, D. Tomic, N. D. Morozova, R. B. Hooker, A. R. Mickelson, and Y. C. Lee. Lasar-array to single-mode-fiber coupling module with increased tolerance budget using polymer waveguide tapers. *Proc. SPIE 2844, Photonics and Radio Frequency*, 60:1–11, December 1996.

[118] S. Janssens. *New materials for ultrafast switching and optical regeneration.* PhD thesis, Victoria University, 2012.

[119] S. G. Raymond et al. Photostability enhancement studies on zwitterionic chromophores for nonlinear optics. In Robert L. Nelson, François Kajzar, and Toshikuni Kaino, editors, *Proceedings of SPIE - The International Society for Optical Engineering*, volume 7599, page 759914. SPIE, 2010.

[120] G. V. M. Williams et al. The effects of excited state lifetime, optical intensity, and excited state quenchers on the photostability of zwitterionic chromophores. *Journal of Applied Physics*, 110(8):083524, 2011.

[121] A. K. Kay et al. Simple zwitterionic merocyanines as potential NLO chromophores. *Journal of materials chemistry*, 11:2271–2281, 2001.

[122] S. G. Raymond et. al. The effects of oxygen concentration and light intensity on the photostability of zwitterionic chromophores. *Journal of Applied Physics*, 105(11):113123, 2009.

[123] S. G. Raymond, G. V. M. Williams, M. T. T. Do, S. Janssens, B. Lochocki, M. D. H. Bhuiyan, and A. J. Kay. Photoluminescence and optical studies of photodegradation in nonlinear optical organic chromophores. In Mario Bertolotti, editor, *Nonlinear Optics and Applications III*, volume 7354, page 735408. SPIE, 2009.

[124] A. Dubois et al. Photostability of dye molecules trapped in solid matrices. *Applied optics*, 35(18):3193–3199, 1996.

[125] P. Soundarrajan and F. Schweighardt. *Hydrogen Fuel: Production, Transport, and Storage.* CRC Press, 2008.

[126] S. Ito, H. Katayama, and M. Yamamoto. Excited triplet state of carbazole chromophore and the triplet energy migration in poly[(carbazolylethylmethacrylate)-(co-(methyl methylacrylate)] film. *Macromolecules*, 21(8):2456–2462, August 1988.

[127] R. A. Keller and L. J. Dolby. Intramolecular energy transfer between triplet states of weakly interacting chromophores. III. compounds in which the chromophores are separated by a rigid steroid bridge. *J. Am. Chem. Soc.*, 91(6):1293–1299, March 1969.

[128] J. Qu, B. Lui, and J. He. Photofading mechanisms of azo dye in its azo and hydrazone forms under UV irradiation. *Journal of Chemical and Pharmaceutical Research*, 6(3):1149–1154, 2014.

[129] T. Mizunami, T. V. Djambova, T. Niiho, and S. Gupta. Bragg gratings in mulitmode and few mode optical fibres. *Journal of lightwave technology*, 18(2):230–235, 2000.

[130] W. Feng, S. Lin, B. Hooker, and A. R. Mickelson. Study of UV-bleached channel-waveguide performance in nonlinear optical polymer films. *Applied optics*, 34(30):6885–6891, 1995.

[131] R. C. Bailey and J. T. Hupp. Large-scale resonance amplification of optical sensing of volatile compounds with chemoresponsive visible-region diffraction gratings. *American Chemical Society*, 124(23):6767–6774, December 2002.

[132] M. Szczurowski. Refractive index database. Technical report, www.refractiveindex.info, February 2015.

[133] Coherent Inc. An introduction to phase masks for FBG writing. Technical report, Coherent Inc., 2013.

[134] Y. Qiu, Y. Sheng, and C. Beaulieu. Optimal phase mask for fiber Bragg grating fabrication. *Journal of lightwave technology*, 17(11):2366–2370, November 1999.

[135] S. A. Wade, W. G. A. Brown, K. B. Harpreet, F. Sidirolou, G. W. Baxter, and S. F. Collins. Effect of phase mask alignment on fibre Bragg grating spectra at harmonics of the Bragg wavelength. *Journal of the optical society of America*, 29(8):1597–1605, August 2012.

[136] K. J. Stevens et al. Characterisation of a fibre Bragg grating system for strain and temperature sensing. *2011 Fifth International Conference on Sensing Technology*, 1(1):234–237, 2011.

[137] R. Magnusson and T. K. Gaylord. Diffraction regimes of transmission gratings. *Journal of optical society of America*, 68(6):809–814, 1978.

[138] D. Bogunovic et al. Limitations of inscribing volume holographic gratings in nonlinear polymer thin films (submitted for publication). *Journal of Applied Physics*, 2015.

[139] Norland Products Inc. Norland optical adhesive 68. Technical report, Norland Products Inc, 2015.

[140] A. Goulet-Hanssens, T. C. Corkery, A. Priimagi, and C. J. Barrett. Effect of head group size on the photoswitching applications of azobenzene Disperse Red 1 analogues. *J. Mater. Chem. C*, 2:7505–7512, 2014.

[141] G. T. Dempsey, M. Bates, W. E. Kowtoniuk, D. R. Liu, R. Y. Tsien, and X. Zhuang. Photoswitching mechanism of cyanine dyes. *JACS communications*, 131(51):18192–18193, December 2009.

[142] Y. Kutuvantavida et al. High electro-optic coefficent in organic NLO polymers: poling and study of the relaxation process. *Materials science forum*, 700:154–157, 2012.

[143] D. Richter, C. Voigtlnder, R. G. Krmer, J. U. Thomas, A. Tnnermann, and S. Nolte. Discrete nonplanar reflections from an ultrashort pulse written volume Bragg grating. *Optics Letters*, 40(12):2766–9, 2015.

[144] A. Chen et al. Chromophore-containing polymers for trace explosive sensors. *Journal of Physical Chemistry C*, 112:8072–8078, 2008.

[145] C. Zhang, W. Zhang, D. J. Webb, and G. D. Peng. Optical fibre temperature and humidity sensor. *Electronics Letters*, 46(9):1–2, April 2010.

[146] A. Chen. *Advanced Photonic Structures for biological and chemical detection*. Springer, 1 edition, 2009.

[147] L. Mosca et al. Sensing of 2,4,6-trinitrotoluene (TNT) and 2,4-dinitrotoluene (2,4-DNT) in the solid state with photoluminescent Ru2 and Ir3 complexes. *Chemistry - A European Journal*, 21(10):4056–4064, 2015.

[148] J. Jae, G. A. Tompsett, A. J. Foster, K. D. Hammond, S. M. Auerbach, R. F Lobo, and G. W. Huber. Investigation into the shape selectivity of zeolite catalysts for biomass conversion. *Journal of Catalysis*, 279:257–268, 2011.

[149] C. L. Yaws. *Thermophysical properties of chemicals and hydrocarbons*. Gulf Professional Publishing, 2008.

[150] X. Chen, C. Zhang, D. J. Webb, G. D. Peng, and K. Kalli. Bragg grating in a polymer optical fibre for strain, bend and temperature sensing. *Meas. Sci. Technol.*, 21:1–5, 2010.

[151] W. Yuan et al. Improved thermal and strain performance of annealed polymer optical fiber Bragg gratings. *Optics Communications*, 284(1):176 – 182, 2011.

[152] S. G. Raymond et al. Development of fibre Bragg grating based strain/temperature sensing system. *Proc. of SPIE: Organic Photonic Materials and Devices XIV*, 8258(1):1–8, 2012.

[153] J. Jiang, G. M. Ma, H. T. Li, C. R. Song, Y. T. Luo, and H. B. Wang. Highly sensitive dissolved hydrogen sensor based on side-polished fiber Bragg grating. *IEEE Photonics Technology Letters*, 27(13):1453–1556, July 2015.

List of Publications

Journal Papers

1. A. J. Swanson, S. G. Raymond, S. Janssens, J. W. Lovell-Smith and M. R. Waterland, "Development of planar dye doped Bragg grating strain sensor", *Applied optics* (2016). (In preparation).

2. A. J. Swanson, S. G. Raymond, S. Janssens, J. W. Lovell-Smith and M. R. Waterland, "Development of planar dye doped Bragg grating humidity sensor", *Photonic Sensors* (2016). (In preparation).

3. A. J. Swanson, S. G. Raymond, S. Janssens, R. D. Breukers, M. D. H. Bhuiyan, J. W. Lovell-Smith and M. R. Waterland, "Investigation of polyimide coated fibre Bragg gratings for relative humidity sensing", *Meas. Sci. Technol. 26(12),* (2015).

4. A. J. Swanson, S. G. Raymond, S. Janssens, R. D. Breukers, M. D. H. Bhuiyan, J. W. Lovell-Smith and M. R. Waterland, "Development of polymer coated fibre Bragg gratings for relative humidity sensing", *Sensors and Actuators A: Physical* (2016). (Submitted for publication).

5. S. Janssens, R. D. Breukers, A.J. Swanson, S. G. Raymond, "Birefringence and photochromic effects of planer dye-doped polymer Bragg grating", *Journal of applied physics* (2016). (In preparation).

Conference Papers

1. A. J. Swanson, S. G. Raymond, S. Janssens, R. D. Breukers, M. D. H. Bhuiyan, J. W. Lovell-Smith and M. R. Waterland, "Polyimide coated fibre Bragg grating based moisture sensor development"', *The Eleventh Conference on Lasers and Electro-Optics Pacific Rim*, Busan, South Korea, (2015).

2. A. J. Swanson, S. G. Raymond, S. Janssens, M. D. H. Bhuiyan and M. R. Waterland, "Development of polymer coated fibre Bragg gratings for relative humidity sensing, *2013 Seventh International Conference on Sensing Technology*, Wellington, New Zealand, 230-234 (2013).